

KIT SCIENTIFIC REPORTS 7682

Safety Analysis for a Fuel Qualification Test with Supercritical Water

Manuel Raqué

Manuel Raqué

**Safety Analysis for a Fuel Qualification
Test with Supercritical Water**

Karlsruhe Institute of Technology
KIT SCIENTIFIC REPORTS 7682

Safety Analysis for a Fuel Qualification Test with Supercritical Water

by
Manuel Raqué

Report-Nr. KIT-SR 7682

Dissertation, Karlsruher Institut für Technologie
Fakultät für Maschinenbau, 2014
Tag der mündlichen Prüfung: 23. Juli 2014

Impressum



Karlsruher Institut für Technologie (KIT)
KIT Scientific Publishing
Straße am Forum 2
D-76131 Karlsruhe

KIT Scientific Publishing is a registered trademark of Karlsruhe
Institute of Technology. Reprint using the book cover is not allowed.

www.ksp.kit.edu



*This document – excluding the cover – is licensed under the
Creative Commons Attribution-Share Alike 3.0 DE License*

(CC BY-SA 3.0 DE): <http://creativecommons.org/licenses/by-sa/3.0/de/>



*The cover page is licensed under the Creative Commons
Attribution-No Derivatives 3.0 DE License (CC BY-ND 3.0 DE):*

<http://creativecommons.org/licenses/by-nd/3.0/de/>

Print on Demand 2015

ISSN 1869-9669

ISBN 978-3-7315-0277-7

DOI: 10.5445/KSP/1000043458

Safety Analysis for a Fuel Qualification Test with Supercritical Water

Zur Erlangung des akademischen Grades

Doktor der Ingenieurwissenschaften

der Fakultät für Maschinenbau

Karlsruher Institut für Technologie (KIT)

genehmigte

Dissertation

von

Dipl.-Ing. Manuel Raqué

Tag der mündlichen Prüfung: 23. Juli 2014

Hauptreferent: Prof. Dr.-Ing. Thomas Schulenberg
Karlsruher Institut für Technologie (KIT)

Korreferent: Prof. Dr.-Ing. Xu Cheng
Karlsruher Institut für Technologie (KIT)

Danksagung

Die vorliegende Arbeit entstand im Rahmen meiner Tätigkeit als wissenschaftlicher Mitarbeiter am Institut für Kern- und Energietechnik (IKET) des Karlsruher Instituts für Technologie (KIT).

Ich möchte diese Gelegenheit nutzen, um mich ganz herzlich bei Herrn Prof. Dr.-Ing. T. Schulenberg, Leiter des IKET, für die Betreuung der Promotion zu bedanken. Zudem stand er mir mit seiner fachlichen Kompetenz immer mit Rat und Tat zur Seite.

Ebenfalls bedanken möchte ich mich bei der EnBW Kernkraft GmbH für das dreijährige Stipendium. Hier gilt mein Dank besonders Frau R. Lübben, Herrn Dr. T. Ortega Gómez und Herrn Dr. T. Vogel für die organisatorische und fachliche Unterstützung im Rahmen des EnBW-Doktoranden-Programms.

Frau M. Ruzickova danke ich, da sie durch die souveräne Leitung maßgeblich zum Gelingen des Projekts SCWR-FQT beitrug. Weiter möchte ich Frau Dr. C. Zhou und Herrn A. Vojáček meinen Dank für die gute und unkomplizierte Zusammenarbeit aussprechen.

Für die Übernahme des Korreferats bzw. des Prüfungsvorsitzes danke ich Herrn Prof. Dr.-Ing. X. Cheng, dem Leiter des Instituts für Fusionstechnologie und Reaktortechnik (IFRT), sowie Herrn Prof. Dr.-Ing. H.-J. Bauer, dem Leiter des Instituts für thermische Strömungsmaschinen (ITS).

In besonderem Maße danke ich meinem langjährigen Bürokollegen Markus Stokmaier, welcher durch Hilfestellungen jedweder Art (u.a. die unermüdliche Überzeugungsarbeit für die Mächtigkeit von Python) zum Gelingen dieser Arbeit beigetragen hat und für die super Zeit! Auch die Kaffeekunde sorgte immer im richtigen Moment für Ablenkung und Erheiterung, danke!

Herzlich danken möchte ich meiner Familie, die mich immer uneingeschränkt unterstützte!

Mein größter Dank gebührt meiner Ehefrau Alexandra für die Unterstützung und Liebe (nicht nur) während der gesamten Arbeit!

Waldshut-Tiengen, im September 2014

Manuel Raqué

Kurzfassung

Sicherheitsanalysen für einen Brennstofftest mit überkritischem Wasser

Ein mit überkritischem Wasser gekühlter Reaktor (SCWR) ist ein vielversprechendes Systemkonzept, welches vom Generation IV International Forum ausgewählt wurde um den Anforderungen einer zukünftigen Energieerzeugung, speziell unter den Gesichtspunkten Sicherheit, Nachhaltigkeit, Wirtschaftlichkeit, Zuverlässigkeit und Proliferationssicherheit gerecht zu werden. Diese Wahl bildet die Grundlage für eine weitere Erforschung und Entwicklung dieses fortschrittlichen Leichtwasserreaktors, welcher auf Grund der Kühlung und Moderation mit überkritischem Wasser einige Vorteile gegenüber der aktuellen Reaktortechnologie aufweist. Da in den vergangenen Jahren im Rahmen eines europäischen Forschungsprojekts bereits eine umfangreiche Konzeptstudie eines 1000 MW_e Reaktors dieses Typs namens High Performance Light Water Reactor (HPLWR) erarbeitet wurde, besteht der nächste logische Schritt nun in einem in-pile Test eines SCWR-Brennelements. Ziel ist es, sowohl erste Betriebserfahrung zu sammeln, als auch eine Datenbasis zu schaffen, die dazu dienen kann, offene Fragen aus den Bereichen Werkstoffe, Thermohydraulik, Wärmeübertragung und Strömungsstabilität zu beantworten. Die Entwicklung und Lizenzierung eines derartigen Brennelements mit angeschlossenem Hochdruckkreislauf inklusive der zusätzlichen Notkühl- und Hilfssysteme bilden den Rahmen des Projekts SCWR-FQT. Bau und Betrieb dieser nuklearen Anlage mit überkritischem Wasser sind innerhalb der nächsten zehn Jahre geplant. Die realistischen Reaktorbedingungen speziell mit Hinsicht auf die Neutronik werden dabei durch den Forschungsreaktor LVR-15 erzeugt, welcher vom Forschungszentrum CVR in Řež in der Tschechischen Republik betrieben wird und in welchen das Brennelement eingesetzt werden soll. Da dies die erste nukleare Testanlage mit überkritischem Wasser darstellt, befasst sich diese Arbeit mit der Gestaltung und der Sicherheitsbeurteilung der für einen gefahrlosen Betrieb unerlässlichen Sicherheitssysteme. Das zu Grunde liegende Sicherheitskonzept der hier ausgearbeiteten Systeme folgt der Strategie der gestaffelten Schutzebenen (Defense In Depth), die in der Kerntechnik weit verbreitet ist. Im Zuge dieser Arbeit wurde mit dem Systemcode APROS ein numerisches Modell der SCWR-FQT Versuchsanlage mit allen sicherheitsrelevanten Komponenten erstellt. Dieses Modell erwies sich als wertvolles Werkzeug zur optimierten Auslegung der aktiven und passiven Sicherheitsvorrichtungen, welche für eine sichere Durchführung des Versuchsprogramms vorgesehen sind. Deren Effektivität und transientes Verhalten wurden mittels zahlreicher dynamischer Sicherheitsanalysen ausgewählter Auslegungsstörfälle bewertet.

Zunächst wurde das numerische Modell durch ein Vernetzen standardisierter Komponenten erzeugt. Bestimmte Teile des Kreislaufs mussten jedoch auf alternative Weise mit Hilfe von Grundmodulen des Codes aufgebaut werden, um den Realitätsgrad des Modells zu erhöhen. Die korrekte Abbildung des Systems wurde anschließend durch Vergleichsrechnungen mit dem Thermohydraulikcode ATHLET sichergestellt. Darüber hinaus wurden geeignete Experimente zu transienten Strömungsphänomenen aus der Literatur zur Codevalidierung verwendet.

Im zweiten Teil werden die Sicherheitsanalysen von Auslegungsstörfällen, welche Kühlmittelverlust, Strömungsabbruch, Verlust der Wärmesenke und unterschiedliche Verkürzungen des Strömungspfadens umfassen, vorgestellt. Diese Simulationen bestätigen, dass alle angenommenen Störfällebe-

dingungen verlässlich, durch das aus einer komplexen Logik von Signalen und anschließenden Aktionen bestehende Kontrollsystem, erfasst werden. Auf diese Weise wird jeder Zwischenfall vom jeweils vorgesehenen Sicherheitssystem beherrscht, sodass keinerlei Freisetzung von Radioaktivität befürchtet werden muss. Darüber hinaus wurde eine Strategie zur Langzeit-Nachzerfallswärmeabfuhr entwickelt. Diese ermöglicht es, die Brennstäbe im Anschluss an das unmittelbare Unfallszenario ausreichend zu kühlen. Ein zusätzliches passives System ist hilfreich, um die Teststrecke daraufhin unter kalten Bedingungen zu stabilisieren.

Zuletzt wurde ein auslegungsüberschreitendes Störfallszenario für das gleichzeitige Versagen mehrerer Komponenten untersucht. Der zeitliche Verlauf der maximalen Brennstofftemperaturen, berechnet mit APROS, diente dabei als Grundlage für eine Quelltermabschätzung zur Quantifizierung der radiologischen Konsequenzen. Hierfür wurde das Freisetzungsmodell CORSOR-O angewandt, welches am Oak Ridge National Laboratory entwickelt wurde. Auch wenn die Eintrittswahrscheinlichkeit eines solchen Vorkommnisses als sehr geringe einzuschätzen ist, konnte aufgrund der beträchtlichen Menge potentiell freigesetzter Aktivität die Notwendigkeit für weitere Redundanzen in den Sicherheitssystemen mit dem Ziel des strikten Ausschlusses solcher Szenarien aufgezeigt werden.

Abstract

Safety Analysis for a Fuel Qualification Test with Supercritical Water

A supercritical water cooled reactor (SCWR) is one promising reactor concept selected by the Generation IV International Forum to meet future energy demands with particular respect to safety, sustainability, economics, reliability, and proliferation resistance. The choice sets the base for further research and development support for this advanced light water reactor, which possesses several benefits compared to present reactor technology due to cooling and moderation with supercritical water. During recent years, a comprehensive design study for a 1000 MW_e reactor called High Performance Light Water Reactor (HPLWR) has been carried out in the framework of a European project. The next logical step is to run an in-pile fuel assembly test. The aim of such a test is to gain first operational experiences and to generate a data basis, which will be very helpful for answering open questions in the fields of materials, thermal hydraulics, heat transfer, and flow stability. The design and licensing of such a small-scale fuel assembly with a high pressure coolant loop, involving emergency and auxiliary systems, is the scope of the project Supercritical Water Cooled Reactor - Fuel Qualification Test (SCWR-FQT). The construction and operation of this first nuclear test facility with supercritical water is envisaged within the next ten years. Realistic reactor conditions for the intended test fuel element will be provided by the hosting research reactor LVR-15, which is operated by the Nuclear Research Centre CVR in Řež, Czech Republic. As such a device has never been built before, this thesis deals with the design and the safety assessment of the emergency cooling systems, which are indispensable for a safe operation. The underlying safety concept of the worked out setup is thereby following the strategy of Defense In Depth, which is widely employed in nuclear engineering. In the course of this work, a numerical model of the SCWR-FQT facility with all safety-relevant components has been elaborated with the one-dimensional system code APROS. This model gave valuable support for the design of the active and passive safety features intended for a safe execution of the testing program. Their performance and transient response have been evaluated by numerous dynamic safety analyses for designated design basis accidents.

As a first step, the numerical model has been developed by the use of interconnected, standardized components. Specific parts of the loop, however, had to be made more realistic through alternative formulations, composing them by basic modules available in the code library. In order to verify the correct implementation of the loop design, a code to code comparison with the thermal-hydraulic code ATHLET has been performed. Furthermore, several experimental data sets from literature describing pertinent transient flow phenomena have been used to validate the numerical code.

In the second part, safety analyses for design basis accidents are presented, comprising loss of coolant, loss of flow, loss of heat sink and different coolant shortcuts. Those simulations confirm that all postulated accidental conditions are reliably detected by a control system based on a sophisticated logic of signals and actions. Thus, each incident will be mastered by the designated emergency system and no release of radioactivity is to be expected. Moreover, a strategy for long-term residual heat removal has been developed ensuring sufficient heat transfer capability to cool the fuel rods subsequent to an accident. For the longer time scale after days, an additional application of a passive system can help to stabilize the test section at cold conditions.

Finally, a beyond-design-basis accident scenario for a multi-component failure has been analyzed. The maximum fuel temperatures obtained from one-dimensional simulations were used as basis for the evaluation of the source term resulting inside the experimental hall, which contains the test facility. For this purpose, the fractional release rate model CORSOR-O has been applied, which has been developed at the Oak Ridge National Laboratory. Although such an event is of very low probability, the considerable amount of potentially released activity revealed the necessity of further redundancies in the safety systems in order to strictly avoid common-mode failures.

Table of Contents

Kurzfassung	i
Abstract	iii
1 Introduction.....	1
1.1 HPLWR – European Generation IV Reactor Concept	2
1.2 SCWR Fuel Qualification Test	3
2 In-pile Test Loop.....	5
2.1 Research Reactor LVR-15.....	5
2.2 Test Section Design.....	6
2.2.1 Heated Section	8
2.2.2 Recuperator	8
2.2.3 Cooler	8
2.3 Safety Concept and Loop Design with Emergency Systems.....	9
2.3.1 Safety Requirements and Defense in Depth Approach	9
2.3.2 Safety Criteria	10
2.3.3 Emergency System Design	12
2.3.4 Trigger Signals of the Safety Systems.....	17
3 Thermal-hydraulic Code APROS	19
3.1 Six-equation Model	19
3.2 Pressure Loss.....	20
3.3 Wall Heat Transfer.....	21
3.4 Critical Mass Flow.....	25
3.5 Non-condensable Gas	25
3.6 Validation of the Commercial System Code APROS.....	26
3.6.1 Water Hammer Experiments	26
3.6.2 Natural Circulation in a Closed Loop	30
3.6.3 Depressurization Transients.....	34
3.7 Code-to-code Comparison of APROS and ATHLET	38
4 Numerical Model of the Loop	41
4.1 Multichannel Configuration of the Test Fuel Element	41
4.1.1 Coolant Density Feedback	44
4.1.2 Decay Heat Curve.....	46
4.2 Depressurization System	47
4.3 Accumulator and Pressurizers	48
4.4 Double-pipe Heat Exchanger CH1	49
5 Design Operation.....	51
6 Design Optimization for Fast Depressurization Transients.....	55

Table of Contents

6.1	Buckling of the Guide Tubes.....	55
6.2	Pressure Histories during a Loss-of-coolant Accident.....	56
6.3	Optimization of the Outlet Cross Sections in the Head Piece of the Fuel Element.....	58
7	Safety Analyses of Design Basis Accidents.....	63
7.1	Trip of the Recirculation Pump	63
7.2	Loss of Heat Sink	66
7.3	Loss of Electric Power Supply with Passive Residual Heat Removal.....	67
7.3.1	Passive Midterm Residual Heat Removal	68
7.4	Blockage of the Coolant Flow Path.....	69
7.4.1	Blockage of the Return Line L2.....	69
7.4.2	Blockage of the Feed Line L1	71
7.5	Coolant Shortcut inside the Test Fuel Element.....	72
7.5.1	Coolant Shortcut between the Emergency Line and Channel 4	72
7.5.2	Coolant Shortcut between Channel 1 and Channel 4.....	74
7.6	Loss-of-coolant Accidents	77
7.6.1	Large Break of the Emergency Cooling Line L3.....	78
7.6.2	Large Break of the Return Line L2	81
7.6.3	Large Break of the Feed Line L1.....	84
8	Beyond-design-basis Accident with In-containment Source Term Analysis	91
8.1	Accident Scenario	91
8.2	Release Rate Model CORSOR-O.....	94
8.3	Source Term	96
9	Summary and Conclusions.....	103
	Nomenclature.....	107
	References.....	111
	Annex A	117
	Annex B	123

1 Introduction

The Generation IV International Forum (GIF), a co-operation of thirteen international members¹, ‘is a co-operative international endeavor organized to carry out the research and development (R&D) needed to establish the feasibility and performance capabilities of the next generation nuclear energy systems’ [1]. In 2002, this organization published a Technology Roadmap [2], pointing out that a growing world population of expected ten billion people in the year 2050 will be facing the challenge of a severely growing energy demand. The text claims further, that in order to avoid negative environmental impacts and long-term consequences from global climate change, the use of climate-neutral and cost-effective energy supplies must be intensified. In this respect, nuclear energy is seen as the only technology with the proven ability of delivering CO₂-free on-demand electricity on a large scale in cost-efficient manner. However, some important challenges need to be addressed in order for nuclear fission power to play a world-wide key role in future. These challenges involve safety, sustainability, economics, reliability, and proliferation resistance and they translate into a number of technology goals that have been formulated by GIF and which are defining for the upcoming fourth generation (Gen IV) of nuclear energy systems, envisaged to be built beyond 2030. The six most promising Gen IV systems, listed alphabetically in Tab. 1-1 were identified and selected for further development support:

Tab. 1-1 Generation IV nuclear energy systems [1].

Gas-Cooled Fast Reactor (GFR)
Lead-Cooled Fast Reactor (LFR)
Molten Salt Reactor (MSR)
Sodium-Cooled Fast Reactor (SFR)
Supercritical-Water-Cooled Reactor (SCWR)
Very-High-Temperature Reactor (VHTR)

Among these systems, there is the supercritical water cooled reactor, which has several advantages compared to present light water reactors, particularly with respect to economy and safety. The development of an SCWR reactor design called High Performance Light Water Reactor (HPLWR) was the scope of the European project High Performance Light Water Reactor – Phase 2 [3], which has been carried out during 42 months between September 2006 and February 2010. Now, considered as a first step towards a small-scale demonstration reactor, an SCWR in-pile fuel element test shall be designed and licensed in the collaborative Chinese-European project SCWR-FQT (fuel qualification

¹ Argentina, Brazil, Canada, China, Euratom, France, Japan, the Republic of Korea, the Russian Federation, South Africa, Switzerland, the United Kingdom and the United States.

test). This test is intended to be performed inside the LVR-15 research reactor hosted by the Nuclear Research Centre CVR near Prague, Czech Republic. As such a device has never been built before, this thesis deals with the design and the safety assessment of the emergency systems, which are essential for a safe operation. The commercial thermal-hydraulic system simulation code APROS (Advanced Process Simulation) has been applied to perform safety analyses for a number of anticipated design basis accidents. A numerical model has been set up covering the fuel assembly and the coolant loop with all safety-relevant components. It allowed the optimization of crucial system components, so that the final setup performed well during all design basis accidents. This means that the obtained simulation results for various accidental scenarios indicate that no radioactive release has to be expected, because the integrity of either the fuel claddings or the loop can be retained. Furthermore, a beyond-design-basis accident sequence of very low probability, a multi-component failure, has been examined employing the fractional release rate model CORSOR-O with the goal of quantitatively estimating the amount of radioactivity released into the containment.

1.1 HPLWR – European Generation IV Reactor Concept

The High Performance Light Water Reactor is a proposed reactor design falling into the SCWR category, which was recently developed as the Euratom contribution to GIF [3]. The scope of the HPLWR – Phase 2 project [4] was ‘to assess the critical scientific issues and the technical feasibility of’ such a system. For this purpose, a comprehensive design study of a 1000 MW_e reactor with a thermal core has been worked out by 13 Euratom partners. This concept combines important economic advantages of boiling water reactors (BWR), with inherent safety benefits of pressurized water reactors (PWR): a direct-cycle, not requiring steam generators and a secondary circuit with an extra set of recirculation pumps (BWR aspects) with a single-phase working fluid avoiding problematic two-phase flow phenomena such as boiling crisis or dryout. Furthermore, the aim is to achieve elevated live steam parameters and thus a higher thermal efficiency by using supercritical water as coolant and moderator, analogue to the evolution which has already taken place in the area of fossil fired power plants. Consequently, the SCWR concept operates above the thermodynamic critical point of water (22.1 MPa, 374 °C). These improvements are primarily aimed at a thermal efficiency of 44 %, which is about 8 % higher than the efficiency of current nuclear power plants. Thus, the essential requirement of cost reduction for the future application of nuclear power plants is, according to Bittermann et al. [5], clearly fulfilled. At the same time, the safety concept with active and passive safety systems, described by Bittermann et al. [6] and de Marsac et al. [7], creates a safety level, which is as high as or even higher than known from advanced light water reactors (LWR).

From the thermal-hydraulic point of view, the HPLWR is characterized by an innovative three-pass core concept, which has been presented by Schulenberg et al. [8]. The coolant gets heated up in four steps from initially 280 °C to 500 °C, when leaving the core. A first heat-up of the water takes place in the moderator gaps and boxes, being followed by pseudo-evaporation in the central evaporator channels of the core. Here, the coolant temperature gets increased from 310 to 390 °C while passing the critical point. Subsequently, the coolant gets supplied to the first superheater, before it finally reaches an average temperature of 500 °C in a second superheater, which is located on the outer edge of the core, surrounding the first superheater. Mixing chambers below and above the core are installed for homogenization of the coolant temperatures.

Other current SCWR concepts are the Japanese Super LWR and the Chinese SCWR-M with a mixed spectrum core [9], [10]. Within the framework of these developments, substantial progress has been made in the investigation of suitable materials, as well as in the prediction of thermal-hydraulics such as heat transfer and flow stability for SCWR applications. However, as there is still only very few data available for model validations, Behnke et al. [11] came up with the idea to run experiments with a small-scale four-pin fuel bundle operated with supercritical water.

1.2 SCWR Fuel Qualification Test

The next logical step, proposed in the Technology Roadmap Update released in 2014 [12], should be the construction and operation of the first nuclear test facility with supercritical water within the next ten years. The design and licensing of a small-scale fuel assembly and the high pressure coolant loop with emergency and auxiliary systems is the scope of the project Supercritical Water Cooled Reactor – Fuel Qualification Test (SCWR-FQT). This project is carried out as part of collaboration between Euratom and China. The second partial project, called Supercritical Water Cooled In-Pile Test (SCRIPT), comprises an electrically heated four-rod bundle, which is also cooled with supercritical water. This preliminary out-of-pile test to be performed at the Jiao Tong University of Shanghai is the Chinese contribution and meant for pre-qualification of the in-pile test. The aim of the SCWR-FQT project is the qualification of a fuel assembly for typical HPLWR operation conditions, whereby, reaching temperature regimes where the claddings would fail shall be avoided. Furthermore, the focus lies on the examination of material and thermal-hydraulic behavior under supercritical water conditions. Although heat transfer in supercritical water can be predicted with reasonable accuracy, there are still high uncertainties prevailing in the transition region close to the critical point. For this reason, the chosen test conditions shall represent the most challenging part of an evaporator channel in which the bulk temperature of the coolant is slightly below the pseudo-critical temperature of 384 °C at 25 MPa, but the cladding temperature is slightly higher, such that a deterioration of heat transfer is provoked. Further ambitious boundary conditions are a peak heat flux of 1500 kW/m² and a coolant mass flux of 1380 kg/m²s. The experimental results are expected to be highly valuable for the validation of thermal-hydraulic models and the qualification of numerical codes. Moreover, this test facility promises advances for the qualification of cladding and structural materials for supercritical water conditions, as demanded by Schulenberg in order to meet ambitious design targets [13].

In addition, this project provides the opportunity to elaborate an approach for the licensing of SCWR facilities, in general. The loop is scheduled to be constructed from 2015 on. The envisaged time frame for operation is 2017 to 2022. A general overview about the progress, made in the SCWR-FQT project since 2011 is given by Ruzickova et al. [14].

2 In-pile Test Loop

In the first part of this chapter an overview of the SCWR-FQT facility is given. After a brief presentation of the research reactor LVR-15, which will host the experiment, the design of the loop and the test fuel element is described in detail. In the second part the required safety systems, which are required for a safe execution of the experiment, and their release signals are discussed. Additionally, the safety criteria and the strategy of Defense in Depth, which were applied during the design phase, are pointed out. The aim is to ensure the integrity of the claddings and the pressure tube during design basis accidents in order to prevent any radioactive release.

2.1 Research Reactor LVR-15

The LVR-15 is a light water moderated pool-type reactor, which is operated at ambient pressure. A schematic cross section of the reactor, which is located at the Czech research institute CVR in Řež, is depicted in Fig. 2-1 [15].

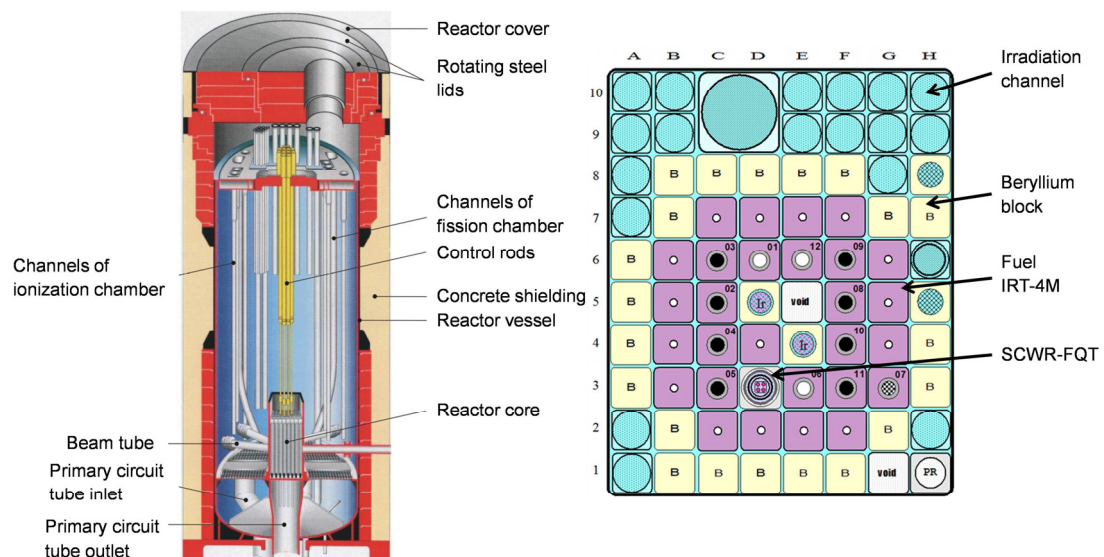


Fig. 2-1 Schematic cross section of the LVR-15 reactor² [15] with designated core composition for the SCWR-fuel qualification test [16].

The research reactor serves as an irradiation source for material testing, radio-pharmaceutical production, nuclear and medical experiments. The reactor vessel has an outer diameter of 2300 mm and a total height of 6235 mm. IRT-4M type fuel assemblies with an enrichment of 20% ^{235}U are composing the core. Thus, the maximum power of the reactor is 10 MW_{th} with a maximum thermal neutron flux of $1.5 \cdot 10^{18}$ n/m²s. The core has an active height of 740 mm and consists of 80 cells with a pitch of 71.5 mm. A nominal downward coolant mass flow of 2100 m³/h passes the core. The coolant outlet temperature is about 50 °C. A forced coolant circulation transfers the generated heat via

² Reprinted from [15], with permission from CVR.

three cooling circuits to the nearby Vltava River. In case of a station black-out, there are two emergency pumps, which are connected to an emergency battery and a diesel generator. Moreover, there are eight B₄C rods installed to regulate the core power [16].

The LVR-15 reactor shall serve as a radiation source for the planned SCWR fuel qualification test. By replacing one of the standard fuel elements of the core with the test fuel element, its performance can be investigated in a critical arrangement. Furthermore, the size of the ordinary assembly will be limiting the size of the pressure tube, which separates the test section from the reactor environment.

2.2 Test Section Design

The test section, which gets inserted into a single cell of the research reactor core, is enclosed by a thick-walled pressure tube made out of austenitic stainless steel 08Ch18N10T (wall thickness = 9 mm), as shown in Fig. 2-2.

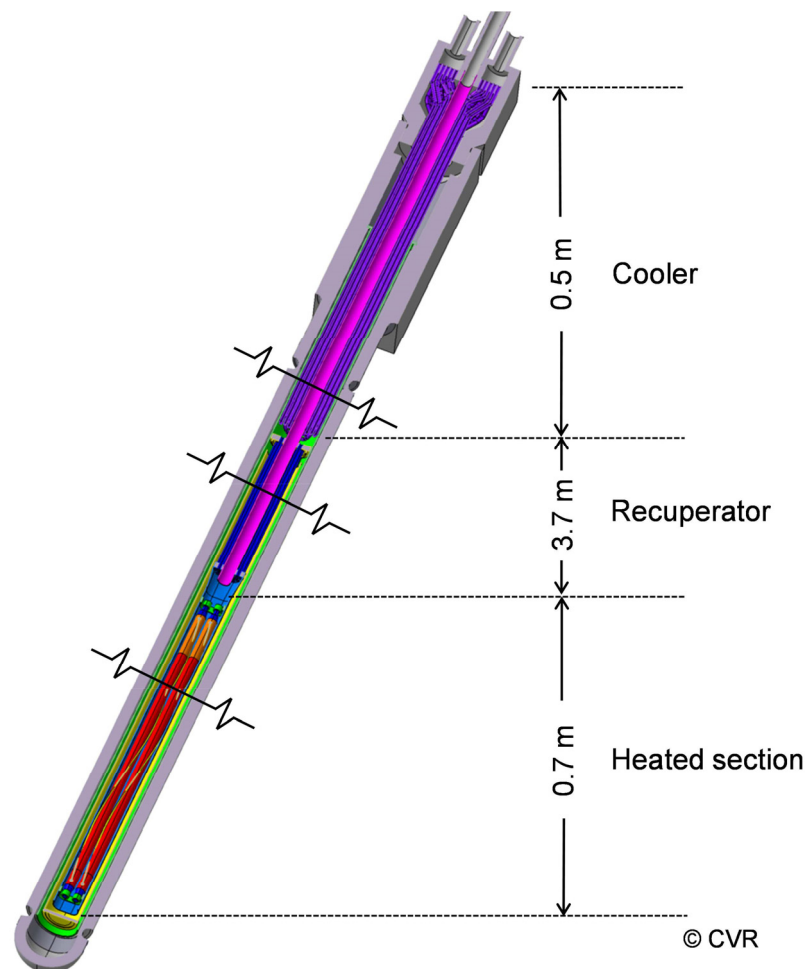


Fig. 2-2 Cross section of the SCWR test fuel element³.

³ Design by CVR, with permission from CVR from 2014.

The pressure tube's outer diameter is limited to 57 mm to fit into the aluminum displacer, which will be fixed in the reactor core grid. By this, an air gap of 3 mm width and 4.3 m height is created. This cushion is open-ended on top and thermally insulates the test fuel element from the reactor pool, which is operated at 50 °C. The pressure tube bears the system pressure of 25 MPa and, furthermore, has to withstand all operational and accidental conditions. The internals of the pressure tube are divided into three sections. From bottom to top, these are the heated section, the recuperator and the u-tube cooler. These sections are described in detail in the next three subsections.

Besides the assembly box (blue), which contains the fuel rods (red), there are two more coaxial tubes mounted inside the pressure tube named guide tubes 1 (green) and 2 (yellow). This pipe-in-pipe arrangement creates the intended flow path through the test fuel element composed by four flow channels. Applying this multichannel configuration extends the residence time of the coolant inside the test fuel element. Thus, high coolant temperatures are achieved at the inlet of the assembly box. The so created geometry of the heated section and the recuperator is illustrated by cross sections depicted in Fig. 2-3. As intended, this configuration allows to simulate thermal-hydraulic conditions comparable to those of the evaporator channels of the HPLWR [3].

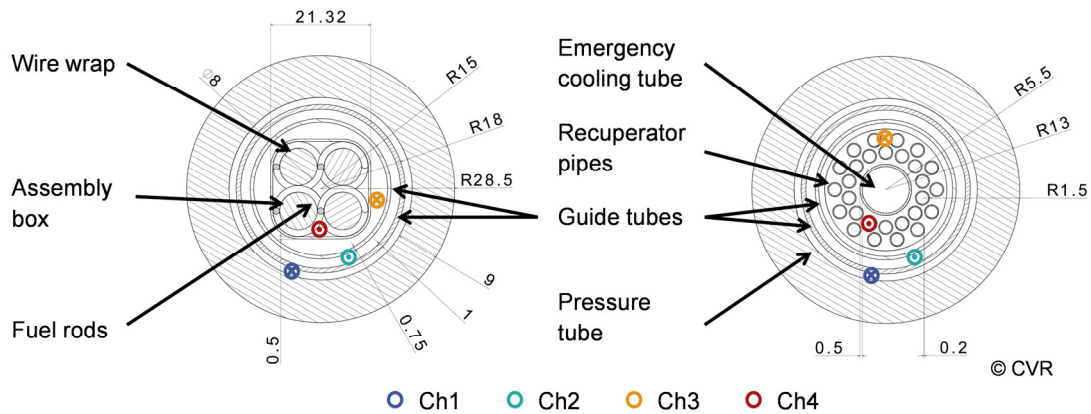


Fig. 2-3 Cross sections of the heated section (left) and the recuperator (right)⁴. Flow directions are indicated by colored circles: cross – downward flow, dot – upward flow.

Another advantage of the guide tubes is the protection of the pressure tube from hot coolant temperatures and thus keeping it below the material limit of 400 °C.

The resulting flow pattern in the fuel element is as follows: The coolant enters the outmost channel (channel 1 (Ch1)) through the fuel element head piece on top of the cooler section. Then it is guided between the pressure tube and the first guide tube to the bottom of the fuel element, where it turns upwards and runs between the two guide tubes to the top of the recuperator (channel 2 (Ch2)). There, it turns downwards again to cool the small recuperator tubes from the outside, forming channel 3 (Ch3) of the flow path. Reaching the lower end of the recuperator, the coolant inside is released to the annulus between the second guide tube and the assembly box. It travels upward through the active test section after being redirected once more at the closed bottom of guide tube 2. Being heated up by the fuel rods, the coolant is entering the small recuperator tubes located above to be cooled down again, before it passes the cooler and leaves the fuel element again. This innermost

⁴ Design by CVR, with permission from CVR from 2014.

flow channel is denoted as channel 4 (Ch4). In Fig. 2-3 the described flow directions inside the channels are indicated by circles with either crosses at their centers for downward flows or with dots for upward flows.

2.2.1 Heated Section

The heated section, which is located in the lowest part of the assembly consists of the before mentioned four coaxial tubes, which are made out of stainless steel, as illustrated on the left side of Fig. 2-3. The central square tube, called assembly box, contains four uranium dioxide fuel rods with an ^{235}U -enrichment of 19.7%. The fuel rods have an active length of 600 mm, according to the core height of the reactor, with additional 40 mm fission gas plenum on top. They are axially constrained by spacers; wire wraps are used as grid spacers to avoid bending as well as to enhance heat transfer, as proposed by Himmel et al. [17]. Different inlet and outlet geometries of the test section were proposed and analyzed with the help of computational fluid dynamics (CFD) by Vágó et al. [18]. The claddings are made out of the austenitic stainless steel 316L, which is qualified for reactor applications. The outer diameter of the rods is 8 mm, which results in a pitch to diameter ratio of 1.18. In order to lower the pressure drop, this value was slightly increased compared to the concept worked out in the design phase of the European project HPLWR [19]. The rod power of the four fuel rods is 63.6 kW in total, consisting of 61.2 kW fissile power and 2.4 kW gamma power, which is released inside the fuel. Thus, the maximum linear heat rate accounts for 37.6 kW/m ($\sim 1500 \text{ kW/m}^2$) at design operation. Additional 9.8 kW of heat are produced by absorbed gamma radiation in the metal structures of the fuel element, primarily in the pressure tube.

The fuel rod bundle is mounted inside the assembly box. At a design mass flow rate of 0.25 kg/s, the coolant mass flux through the assembly box is $1380 \text{ kg/m}^2\text{s}$. With these settings, a maximum average coolant temperature of around 483 °C can be reached at the upper end of the fuel rods.

2.2.2 Recuperator

The recuperator section, which has a length of 3.7 m, is located on top of the heated section. It shall preheat the coolant to achieve higher temperatures in the assembly box. The recuperator consists of 28 tubes, each with an inner diameter of 2.6 mm, arranged in two concentric circles, as indicated on the right hand side of Fig. 2-3. The hot coolant, which left the heated section, is carried inside the tubes in upward direction, while the colder water is passing the shell side of the recuperator in channel 3. In the center of the assembly, an emergency cooling tube is located, which ends directly above the four fuel rods. In case of an accident this tube can be used to inject cold water to quench the rods. During normal operation, the emergency cooling tube is closed at its upper end and contains stagnant coolant.

2.2.3 Cooler

The cooler, mounted in the top most part of the test fuel element, consists of 17 u-tubes, each with an inner diameter of 2 mm and 0.5 mm wall thickness, as shown in the cross section on the left hand side of Fig. 2-4. As the sole heat sink in the primary circuit, the cooler is designed to remove the total inserted heat of 73.4 kW before the coolant leaves the fuel element again. On the tube side, the cooler is part of an additional high pressure circuit ($p = 25 \text{ MPa}$), called secondary circuit, which is

equipped with a pressurizer (KO₂). At design operation, the secondary circuit mass flow is 0.7 kg/s. The secondary side coolant enters the cooler tubes with a temperature of 190 °C and gets heated up to 215 °C while the primary coolant gets cooled down from 352 to 300 °C, as shown in the graph on the right hand side of Fig. 2-4. In the cross section the flow directions are indicated either by a cross for downward flow or by a dot for upward flow.

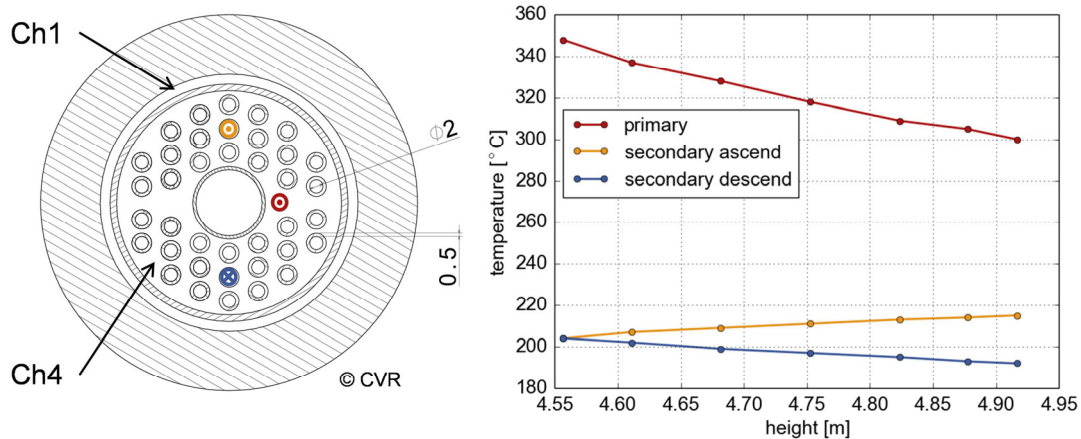


Fig. 2-4 Cross section of the u-tube cooler⁵ with according temperature distribution.⁶

2.3 Safety Concept and Loop Design with Emergency Systems

The SCWR-FQT shall be licensed by the Czech regulator, the State Office for Nuclear Safety (SÚJB). Although the radioactive inventory of this experimental facility is small compared to commercial nuclear reactors, it is still considered as a regular nuclear facility and must conform to the safety guide for research reactors [20]. For this reason, reliable safety systems are required in order to gain approval for in-pile operation. These systems must be capable to handle specified design basis accident without any radioactive release and serve for effective residual heat removal for the event that an accident occurs.

2.3.1 Safety Requirements and Defense in Depth Approach

According to the Requirements on Nuclear Installations for Assurance of Nuclear Safety, Radiation Protection and Emergency Preparedness [21] formulated by the Czech State Office for Nuclear Safety, the safety of nuclear installations shall be assured by a strategy of Defense in Depth (DiD). For this reason, DiD adopts the three generic goals: prevention, control and mitigation. A key aspect of this approach is the use of multiple physical barriers in order to prevent the propagation of ionizing radiation and of radionuclides into the environment. Technical and organizational measures shall be taken to secure and preserve the effectiveness of these barriers on the one hand, and to protect the personnel and other persons, inhabitants and the environment on the other hand.

⁵ Design by CVR, with permission from CVR from 2014.

⁶ The cross section shows the old cooler design with 19 pipes; in the final design only 17 pipes are installed.

Moreover, a methodical approach called Integrated Safety Assessment Methodology (ISAM) for Gen IV nuclear systems [22], which is provided by the Risk and Safety Working Group (RSWG), was taken as a guide line throughout the conception and design development of the loop and its safety systems. Accordingly, a simple but robust loop design in combination with a thoroughly considered test program has been worked out in order to prevent serious conditions right from the start. Further on, efforts have been made for the identification of potential abnormal situations and their initiating events. Thereinafter, protective safety measures could be made up which are able to manage accidental situations and mitigate their consequences. Last but not least, deterministic analyses accompanied the whole process in order to evaluate the adequacy of the applied measures.

As part of the application of the multiple-barrier concept to the SCWR-FQT experimental facility, the definition of these barriers is carried out in conformity with the definition used for nuclear reactors. Thus, the UO_2 matrix is considered to be the first barrier against radioactive release. The second barrier is formed by the gas-tight fuel claddings. The closed primary loop, consisting of the test fuel element, the connecting piping, the recirculation pump and the safety systems, composes a third barrier. For the unlikely case of a failure of all three barriers, a kind of containment serves as a fourth barrier. This is provided by the reactor, an attached duct, which encloses the piping between reactor and the adjoining laboratory, and the experimental hall which is operated at sub-atmospheric pressure. The layout of the described SCWR-FQT facility is depicted in Fig. 2-5.

In advance of the in-pile operation, the entire test facility will be comprehensively tested out-of-pile. Furthermore, the cladding material 316L as well as the pressure tube and piping material 08Cr18Ni10Ti are qualified for reactor applications. Both materials were particularly tested under supercritical water conditions with regard on water chemistry and surface finish [23], [24]. The austenitic stainless steel 316L was found to be the best performer with respect to stress corrosion cracking. Although, this test is planned with the aim to qualify the fuel element for typical SCWR conditions, it is not foreseen to run the test until the claddings will fail. Moreover, a control system is permanently monitoring any deviation from the design working point. According to [20], the associated safety instrumentation is operating with lower warning levels and higher safety levels, indicating minor irregularities to the operating staff in advance of the automatic intervention of the emergency system. The warning levels are chosen, such that the operating personnel are able to influence the state of the system before the value of the relevant quantity reaches the safety level limit.

All codes used to design the test facility and to perform safety analyses have been qualified for nuclear reactor applications. The thermal-hydraulic code APROS version 5.09 used in this work is described in Chapter 3. The developer specifically extended and tested the code for the supercritical pressure region [25], [26].

2.3.2 Safety Criteria

A number of design basis accidents have been analyzed with numerical tools to evaluate the performance of the foreseen safety systems. These accidental scenarios, considered in work package 3 of the SCWR-FQT project, which deals with safety analyses, are listed in Tab. 2-1 [14].

Tab. 2-1 Design basis accidents considered in the SCWR-FQT project.

1. Loss of coolant due to break of any coolant supply line.
2. Trip of the primary pump.
3. Loss of electricity supply for the loop.
4. Blockage of the coolant flow path.
5. Detachment of the wire wrap or other spacer concept designed for the fuel assembly, causing local blockage inside the test section.
6. Fatigue of the internal structures of the pressure tube by coolant temperature differences and associated thermal stresses.
7. Coolant bypassing the test sections due to cracks in the internal structures of the pressure tube.
8. Accumulation of radiolysis gas in stagnant coolant lines, e.g. the central emergency coolant injection line, causing the risk of a hydrogen explosion.
9. Reactivity insertion by change of coolant temperature or by fuel rod deformations.

Scenarios 1 to 4 and 7 are investigated and discussed in detail in this work (Chapter 7), by addressing them with numerical simulations. A local blockage of the test section, e.g. caused by a detached wire wrap, is simulated by Liu [27] with the sub channel code MATRA-SC. His results indicate that a local failure of the cladding must be expected in such case. However, this would be detected by an increased coolant activity and no secondary failures or activity release to the environment should be caused. Item 8 is examined closely by Zeiger et al. [28]. It was found that a permanent hydrogen removal in the coolant make-up system is required in order to mitigate increased hydrogen concentrations, particularly in the closed emergency cooling tube. Furthermore, a reactivity response to off-design conditions (item 9) is analyzed with a Monte Carlo N-Particle Transport Code [29]. From these simulations it can be concluded that such a response is negligible and fully coped by the reactor control system. Finally, Chapter 8 sets the focus on a beyond-design-basis accident with radioactive release into the containment.

In order to evaluate the numerical thermal-hydraulic predictions and thus the capacity of the safety systems to mitigate the consequences of postulated accidents, design criteria are applied. These systems shall be designed such that none of these criteria gets violated during the dedicated state of operation. According to the results of Novotny et al. [30], the maximum cladding surface temperature for the design operation of the test was defined to be 550 °C, in order to avoid the risk of stress corrosion cracking. For transient safety analyses, this value may be exceeded temporarily as corro-

sion and creep play a minor role as failure mechanism during potential short-term temperature peaks. Under such conditions, the integrity of the second barrier will not be endangered as long as a plastic deformation of the material is prevented. For this reason, the yield strength of the material was chosen as the acceptance criterion. According to the ASME (American Society of Mechanical Engineers) Boiler and Pressure Vessel Code [31], short-term failure of the stainless steel claddings must be expected at a temperature of more than 816 °C (= 1500 °F).

2.3.3 Emergency System Design

Two high pressure loops are composing the SCWR-FQT facility. The first one, the 300 °C closed primary circuit is connected to the test fuel element. A second circuit is connected to the cooler in the top part of the fuel element. Both loops with auxiliary systems are situated in the experimental hall, which is located next to the reactor building. The connection to the fuel element is realized via a 30 m long traverse. A 3D drawing of the experimental setup, with the exception of auxiliary systems, is shown in Fig. 2-5.

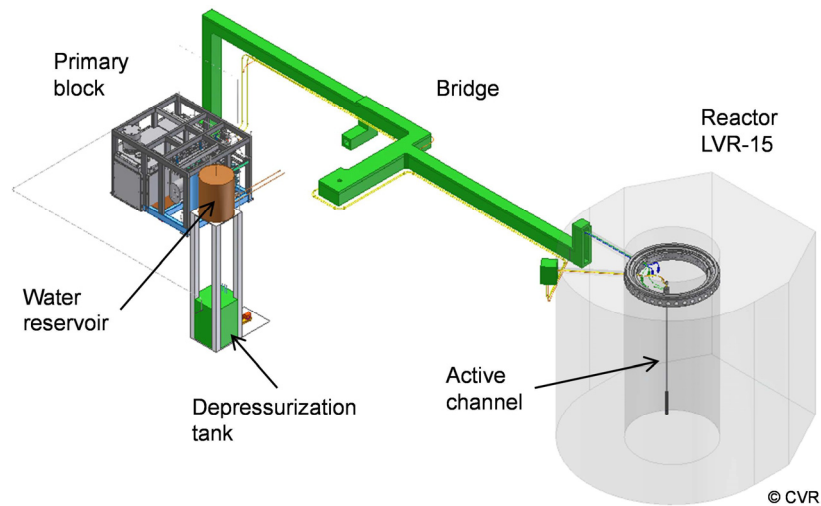


Fig. 2-5 SCWR-FQT facility and research reactor LVR-15 with installed test fuel element⁷. All primary circuit equipment is shielded by lead forming a closed containment.

All mechanical parts are assembled in the so-called primary block containing the recirculation pumps and the emergency systems, as well as the purification, measurement, and H₂ treatment systems. In order to make the building accessible during the operation of the loop, the primary circuit has to be shielded with lead plates, as the coolant gets N-16 activated. A stable system pressure of 25 MPa in both circuits is provided by bladder accumulators. All tubes of the primary and secondary circuit are made out of austenitic steel (08Ch18N10T), which has a high corrosion resistance to supercritical water [23]. The tubes have an inner diameter of 14 mm and a wall thickness of 4 mm; the wall roughness is assumed to be 6.3 μm. The safety systems, which are required to assure a safe performance of the experiments, shall be presented in the following. The system schematic is depicted in Fig. 2-6, leaving out only non-safety-relevant devices like water treatment systems etc. This

⁷ Design by CVR, with permission from CVR from 2014.

scheme also pictures the network of components which is the basis of the APROS model used for safety analyses in this work.

a) Primary Circuit with Safety Systems

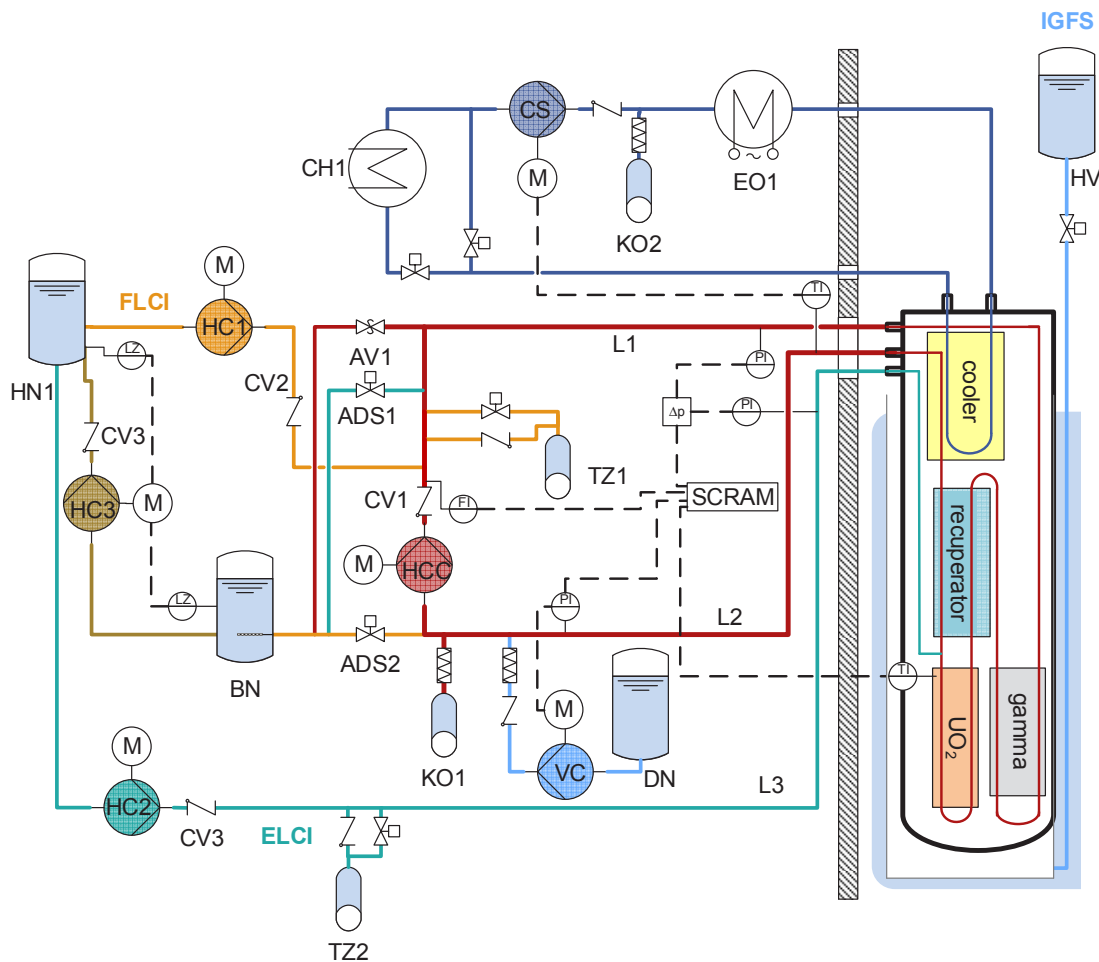
In the safety requirements of the Czech regulator [20] the following two major needs are addressed to the reliability and robustness of the primary circuit and the safety systems design:

- 1) The design of the primary circuit must take into account any influence of normal and abnormal operation as well as accident conditions, which can result in its damage and fuel failure.
- 2) The protection system must be designed so that no single failure causes loss of system protective function; however, such failure can result in reactor shutdown.

As sketched in Fig. 2-6, the primary circuit, drawn in red color, consists of the pressure tube, a hermetic multistage recirculation pump (HCC) with a nominal pump head of 110 m and a nominal mass flow rate of 1.23 m³/h and a downstream check valve CV1.

On the high pressure side, the coolant is injected into the fuel element through the feed line 1 (L1). The circuit is closed by the return line 2 (L2) on the low pressure side of the pump HCC. Before starting operation, the primary system is filled and the pressure gets increased by boost pump VC, taking water from the refilling tank DN. Furthermore, a bladder type accumulator (KO1), prefilled with nitrogen gas, contains 30 l of water and minimizes pressure fluctuations inside the system. As this pressurizer is directly connected to the 300 °C loop, an upstream air cooler is applied to meet the temperature limit of 80 °C for the bladder material.

The loop is equipped with two active safety systems to cool the rods in case of an accident: the so called feed line coolant injection (FLCI, orange) and the emergency line coolant injection (ELCI, dark green). Each system is driven by a separate emergency pump (HC1, HC2) and fed by the emergency cooling reservoir (HN1) containing 1.2 m³ of water. Both pumps are hermetically sealed displacement pumps with an assumed nominal head of 1000 m, a maximum head of 1250 m and a nominal mass flow rate of 0.36 m³/h. With these two systems, it is possible to inject emergency coolant over different lines into the test fuel element. The FLCI system uses the regular coolant supply line (L1), whereas with the ELCI system it is possible to quench the fuel rods very effectively by injecting water over the emergency cooling line (L3), which is located in the center of the geometry and ends directly on top of the heated section. Using the emergency cooling line, however, requires a change of flow direction in the loop. During normal operation this line contains stagnant water. Check valves are installed downstream of all pumps to prevent backflows and shortcuts of the coolant. A run-up and coast down time of two seconds was assumed for all pumps.



ADS – Automatic depress. system	EO1 – Electrical heater	HN1 – Emergency coolant reservoir
AV – Pressure relief valve	HC1 – Emergency pump 1	HV – Reservoir
BN – Pressure suppression tank	HC2 – Emergency pump 2	KO – Pressurizer
CV – Check valve	HC3 – Refilling pump	TZ – Pressure accumulator
DN – Refilling tank	HCC – Recirculation pump	VC – Boost pump

Fig. 2-6 Schematic drawing of the SCWR-FQT loop with safety systems (purification systems are not shown).

In the event that a critical incident occurs, the system has to be depressurized quickly. For this reason, each emergency system is connected to a depressurization line (ADS1, ADS2). The coolant gets routed to the depressurization tank (BN) via a common sparger which is spiraling down into the water volume. This leads to a substantial temperature decrease of the incoming water even before it gets in contact with the tank inventory, stored at ambient conditions. At the end of the sparger line, the hot coolant is ejected through 50 outlet holes ($d = 2$ mm). Furthermore, overpressure is limited using a spring loaded pressure relief valve (AV1) opening another line forking off into the sparger. In order to realize a closed emergency cooling loop, it is possible to refill coolant from the depressurization tank to the emergency coolant reservoir by activation of the refilling pump HC3. This is necessary because, during incidents with intact piping, the water level in the depressurization tank will rise while it decreases in the reservoir HN1. The pump gets automatically activated once the

coolant level in the depressurization tank exceeds a maximum or if the coolant storage in the reservoir falls below a certain minimum. Both tanks are assumed to be of cylindrical shape, installed in upright direction and having an inner diameter of 1 m and a height of 1.5 m. They are vented and kept always at ambient pressure.

Two additional bladder accumulators (TZ1, TZ2) are installed: one in the feed line and the other one in the emergency cooling line. In case the system pressure falls below the specified pre-charge pressure of the accumulators, they will immediately empty their contents and quench the test section with a high coolant mass flow rate. Thus, a boiling crisis can be avoided in most cases or its consequences are considerably reduced. Furthermore, this measure will give a grace period for the emergency pumps to run up. The bladder accumulators are completely passive devices. To prevent hot coolant from entering the accumulators, check valves are installed, which only allow outflows.

In order to support the active safety systems, there is another independent and completely passive system, the so-called insulation gap flooding system (IGFS). This system consists of a 50 liter water tank (HV) which is connected to the bottom of the aluminum displacer enclosing the fuel element. After a reactor scram, a valve can be opened manually and water from the tank floods the insulation gap, which is separating fuel element and reactor pool. Thus, the pressure tube gets effectively cooled from the outside as the heat transfer from fuel element to the reactor pool gets strongly improved. The gap created by the aluminum displacer is shown in sectional views on Fig. 2-7.

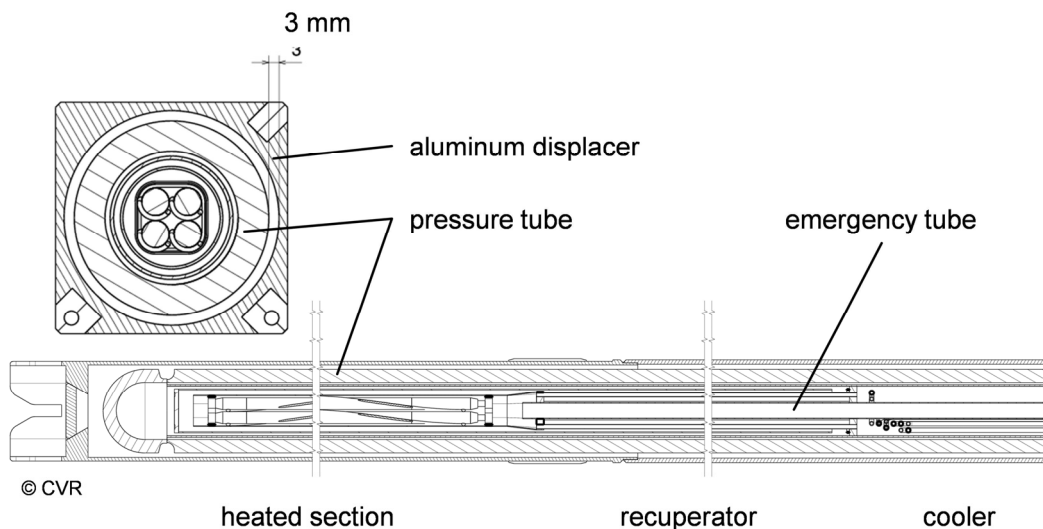


Fig. 2-7 Longitudinal cut through the test fuel element and cross section of the heated section⁸.

b) Secondary Circuit

The secondary circuit (illustrated in dark blue in Fig. 2-6) has to ‘ensure reliable removal of heat from the primary circuit’ [20]. For this reason, a quite large heat transfer area between primary and secondary loop is realized by the insertion of 17 u-shaped cooler tubes into the top part of the test

⁸ Design by CVR, with permission from CVR from 2014.

fuel element. This cooler, described in Chapter 2.2.3, serves under normal operation conditions as the sole heat sink of the system. It removes the fissile and γ -power generated in the test section via u-shaped cooler pipes. Hence, the added heat is removed from the primary coolant even before it leaves the test fuel element. The secondary circuit pressure of 25 MPa is being held by the pressurizer (KO2), while the centrifugal pump (CS) provides the required coolant mass flow rate. The pump speed is controlled with a PI (proportional-integral) control using the outlet temperature of the pressure tube in the primary system as the controlled variable with a set point of $T = 300\text{ }^{\circ}\text{C}$. At design operation this results in a secondary side mass flow rate of 0.7 kg/s .

A double-pipe heat exchanger (CH1) removes the heat from the secondary circuit once again and transfers it to the tertiary side low pressure cooling circuit ($p = 0.6\text{ MPa}$), which is part of the reactor cooling system. As illustrated in Fig. 2-8, the heat exchanger consists of 37 pipes, carrying the hot, high pressure coolant, while the cold, low pressure coolant flows on the shell side, guided by a hexagonal tube. Baffle plates inside the heat exchanger improve the mixing of the coolant. A helium filled gap in the tube walls prevents the coolant on the low pressure side from boiling. As the cooler is slightly over dimensioned with a tube length of 2.25 m , a cooler bypass is installed to adjust the desired inlet temperature at the u-tube cooler of $190\text{ }^{\circ}\text{C}$. Thus, a content of 0.31 kg/s , which is passing through the cooler, gets cooled down from 211 to $159\text{ }^{\circ}\text{C}$. At the same time the tertiary side coolant is heated up from $60\text{ }^{\circ}\text{C}$ to $95\text{ }^{\circ}\text{C}$.

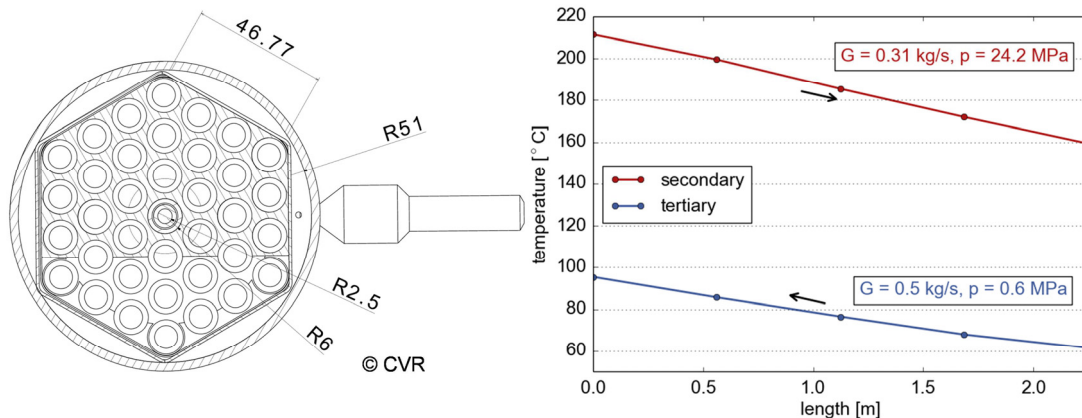


Fig. 2-8 Cross section of heat exchanger CH1⁹ and temperature distribution.

Next to being a heat sink, the secondary circuit has the additional function of being a heat source to the primary circuit during the system start-up procedure, as described by Vojáček [32]. For this reason, an electrical heater EO1 with a maximum power of 50 kW is part of the secondary circuit, which consists of ten heating rods with a length of 2.85 m . For the duration of start-up, the cooler CH1 has to be bypassed, leaving only a very small mass flow through the cooler to avoid thermal shocks after switching to normal operation.

⁹ Design by CVR, with permission from CVR from 2014.

2.3.4 Trigger Signals of the Safety Systems

The safety system of the FQT loop is designed according to the requirements demanded in [20]. Thus, it has to ‘be capable of identifying abnormal conditions and actuating automatically the relevant equipment including subsystem for reactor shutdown with the objective not to exceed the design limits’. Thus, the emergency systems are designed such that the integrity of the fuel rod claddings is maintained in case of any design basis accident, as described by Schulenberg et al. [33] As e.g. the position of any break of the coolant lines can hardly be determined automatically, the triggers activating either one of the emergency cooling systems must rely on the available signals listed in Tab. 2-2.

Tab. 2-2 Signals and actions of the safety systems.

Signal	Warning level	Scram level	Actions	
<ul style="list-style-type: none"> • System pressure low [MPa] • Coolant mass flow low [g/s] 	<p>< 23.5 < 200</p>	<p>< 22.5 < 150</p>	<p>Reactor scram ADS2 opens HC1 pump starts HCC pump stops</p>	FLCI
<ul style="list-style-type: none"> • Coolant temp. in test section high [°C] • Pressure diff. L1-L3 negative [MPa] 	<p>> 420 < 0</p>	<p>> 500 < -3</p>	<p>Reactor scram ADS1 opens HC2 pump starts HCC pump stops</p>	ELCI
<ul style="list-style-type: none"> • System pressure high [MPa] 	<p>> 30</p>	<p>none</p>	<p>AV1 opens (spring loaded)</p>	PRV

As visible from Table 1, the FLCI and the ELCI systems are activated by different, independent signals. The decision criteria are based on the parameters temperature, pressure and coolant mass flow rate. For monitoring these values the primary loop is equipped with the following safety instrumentation:

Three pressure taps are connected to the primary loop, giving a warning at high or low pressures (< 23.5 MPa, > 26 MPa). A scram is released as soon as the system pressure drops below 22.5 MPa. In case of a decreasing system pressure, it is mandatory to scram the reactor already at supercritical pressure. In this manner, running into post-dryout conditions at full heating power can be avoided. This scenario, which is accompanied with temporarily very high cladding temperatures, has been numerically analyzed by Schulenberg et al. [34].

The mass flow rate inside the primary loop is measured with an orifice downstream of recirculation pump HCC, causing a warning at a rate of 200 g/s and a scram if the value falls below 150 g/s. At the same time the FLCI system gets triggered.

Inside the test section, there are three thermocouples positioned, causing a warning at 420 °C, and a reactor scram if the local coolant temperature exceeds 500 °C. Furthermore, the reactor shutdown is initiated in case that two thermocouples have failed. This temperature surveillance activates the

ELCI system. (Cladding surface temperatures will also be measured; however, they are not used as a safety signal to avoid triggering the wrong emergency system.)

Another activating signal for the ELCI system is a negative differential pressure over the test fuel element, measured with pressure taps between the feed line and the emergency cooling line. This is indicating a reversal of flow direction, for example caused by a break of line 1. In this case, the correct emergency system gets activated much faster than it would by the temperature signal. Here, an offset of -3 MPa was chosen to mitigate an erroneous triggering due to pressure pulses. Signals for the ELCI system are dominant in order to avoid conflicts in case both systems are addressed. Furthermore, the ELCI system is a backup for the FLCI system if the latter system fails, e.g. due to a break of the feed line.

Whenever the reactor scram is initiated, the loop gets depressurized via one of the two automatic depressurization systems ADS1 or 2, and the recirculation pump gets stopped. As soon as the system pressure decreases below 12 MPa, either emergency pump HC1 or 2 starts to inject coolant from the reservoir HN1.

After a scram, a delay time of 1 second is foreseen before activation of the ADS valves, corresponding to the insertion time of the control rods. Again, this shall prevent running into the post-dryout heat transfer regime due to the depressurization of the loop at elevated powers (discussed in Chapter 3.6.3), as the power got reduced to residual heat during the delay.

Excess pressures (> 26 MPa) are automatically corrected by a spring loaded pressure relief valve (AV1), which is opening passively.

In order to establish a closed coolant recirculation for long-term residual heat removal, pump HC3 is applied, which transfers water collected in the depressurization tank BN back to the emergency reservoir. The pump is activated in case the depressurization tank is filled up to a high level of 1.1 m, it is stopped again once the low level of 0.8 m is reached. Another signal activating the pump is given by a low inventory of the emergency reservoir. This signal is released in case the threshold of 0.2 m is underrun. Thus, the stored water in the depressurization tank is available to extend the duration of emergency cooling, e.g. in case of loss-of-coolant accidents.

The depressurization system is designed according to the so-called fail-safe principle, which provides additional protection. This means that a loss of power supply will trigger safety-related actions. Therefore, valve ADS1 is opened by a spring and kept close electrically during normal operation. A loss of power causes an automatic depressurization of the loop and allows the FLCI system, which is connected to the emergency power supply system, to take action.

3 Thermal-hydraulic Code APROS

For the optimization of safety system design parameters and for the performance of safety analyses, the loop with all safety-relevant components is represented by a one-dimensional model (cp. Fig. 2-6). The advanced numerical code used for this task is the commercial best-estimate system code APROS [35] developed in co-operation by VTT Technical Research Centre of Finland and Fortum Nuclear Services Ltd. It has already been used widely in the field of thermal and especially nuclear power plants. For instance, accident analyses performed with APROS have been approved as official licensing analyses for Finnish NPPs by the Finnish Radiation and Nuclear Safety Authority (STUK). Furthermore, the code is applied for simulations of the European Pressurized Water Reactor (EPR), which is currently under construction at Olkiluoto 3 site in Finland [36]. Here, it finds use over the complete project cycle from plant design to operator training. The code is suitable for a broad range of application areas, such as process and automation design, development of emergency operating procedures, testing of instrumentation and control systems, accident analyses, and simulator application training. 1D and 3D reactor neutronics are included in the calculation models. The thermal-hydraulic model is based on a finite difference scheme. For the calculation of one-dimensional two-phase flows, there are 3-, 5- and 6-equation models available. Moreover, fast access material property tables enable a quick and efficient computation of water and steam material properties. Pre-defined process components such as pipes, valves, pumps and heat exchangers are provided. Properties can be specified by the user, by using the graphical user interface (GUI).

More recently, the development of Gen IV features in APROS came into focus, including the implementation of new cooling media such as sodium and lead. Moreover, an extension of the thermodynamic properties for water and steam to the supercritical pressure region, according to the international standard IAPWS-IF97 [37] is featured by APROS version 5.09. In addition, Kurki [38] implemented pressure loss and heat transfer correlations for supercritical water. These code modifications also enable a stable transition from the super- to the subcritical pressure state. For these reasons, APROS has already been used to perform comprehensive dynamic simulations of the water-steam cycle [39] and safety analyses [26] of the HPLWR. Within this thesis, the code shall be applied for modeling of a nuclear test facility with supercritical water.

3.1 Six-equation Model

Choosing a one-dimensional two-fluid model for super- and subcritical conditions allows a reliable and accurate physical description of the process state. The model developed by Hänninen and Ylijoki [40], called six-equation model, is based on the one-dimensional conservation equations of mass (3.1), momentum (3.2) and energy (3.3), which are applied to the liquid and the gas phase. Thus, the phases are treated as separate fluids. However, both phases are coupled to each other by empirical heat transfer and friction correlations.

$$\frac{\partial(\alpha_k \rho_k)}{\partial t} + \frac{\partial(\alpha_k \rho_k u_k)}{\partial z} = \Gamma_k \quad (3.1)$$

$$\frac{\partial(\alpha_k \rho_k u_k)}{\partial t} + \frac{\partial(\alpha_k \rho_k u_k^2)}{\partial z} + \alpha_k \frac{\partial p}{\partial z} = \Gamma_k u_{ik} + \alpha_k \rho_k \vec{g} + F_{wk} + F_{ik} + F_{va} + F_{fl} + \Delta p_{pu} \quad (3.2)$$

$$\frac{\partial(\alpha_k \rho_k h_k)}{\partial t} + \frac{\partial(\alpha_k \rho_k u_k h_k)}{\partial z} = \alpha_k \frac{\partial p}{\partial t} + \Gamma_k h_{ik} + \dot{Q}_{wk} + \dot{Q}_{ik} + F_{ik} u_{ik} \quad (3.3)$$

The density is denoted by ρ , the velocity by u , and the pressure by p . The time is t and the space coordinate in longitudinal direction is z . Furthermore, the index k stands for the phase of the fluid, either liquid l or gaseous g . Interfaces are either denoted by i for the gas-liquid interface or by w for the wall surface. The term Γ is the mass change rate between the phases due to evaporation – positive or condensation – negative values. α is the volume fraction of each phase and \vec{g} is the gravitational acceleration. Heat flows are denoted as \dot{Q} , friction forces as F (va – valves, fl – form loss, pu – pump head). Furthermore, the term h represents the enthalpy in the energy equation (3.3) including kinetic fractions.

The numerical solution of the governing equations is based on a staggered grid. An upwind finite difference scheme is used to solve the convection terms [41]. This means that the variables of state, pressure and enthalpy are calculated in nodes, representing the center of a mesh cell, whereas the flow variables are calculated at the interface between two cells, called branch. The implicit solution procedure for the numerical problem is described by Siikonen [42]. The partial differential equations are discretized with respect to time and space. By inserting the momentum equation into the mass equation a linear system of equations is derived, which allows solving the pressure field. The calculated pressures, in turn, yield new mass flow rates in all branches. With this data, the equation system for the enthalpy can be solved. This iterative algorithm is continued until the convergence criterion for the mass flow error for both phases is met, which can be specified by the user. In case the desired accuracy is not reached within a defined number of iterations, the code automatically halves the calculation time step. In this work, a maximum relative mass error of 10^{-4} is allowed. For fast transients e.g. large break loss-of-coolant accidents (LOCAs) a maximum time step of 0.001 s or less is recommended, according to [41]. The remaining material properties of water/steam, which are implemented according to IAPWS-IF97 [37] are derived from tables as functions of pressure and enthalpy. As some correlations implemented in APROS depend on the existing flow regime, the code provides models for stratified flow and non-stratified flow consisting of bubbly, annular and droplet flow. Moreover, weighting coefficients are applied in order to achieve a smooth transition between the models, as described by Bestion [43]. These are void fraction, rate of stratification and rate of entrainment. A detailed description of the applied models can be found in [44] and [40]. Furthermore, Kurki [38] extended the model for the supercritical pressure region by introducing a so-called pseudo-critical enthalpy, which allows the smooth transition of the fluid from liquid-like to vapor-like, as described in Chapter 3.3.

3.2 Pressure Loss

Here, f_k is the friction factor of phase k . It consists of a single-phase friction factor $f_{sp,k}$ and a two-phase friction multiplier c_k :

$$f_k = f_{sp,k} \cdot c_k \quad (3.4)$$

To determine the single-phase friction factor, the Colebrook equation (3.5) is applied as cited by Kolev [45], considering the roughness ε of the pipe walls:

$$\frac{1}{\sqrt{f_k}} = 1.74 - 2 \cdot \log \left[\frac{1}{\sqrt{f_k}} \frac{18.7}{Re_k} + 2 \cdot \frac{\varepsilon}{d_H} \right]. \quad (3.5)$$

For high Reynolds numbers Re_k the friction factor for a fully developed turbulent flow according to Eq. (3.5) is applied, assuming that the Reynolds number approaches infinity. This results in:

$$f_{cr,k} = \left[1.74 - 2 \cdot \log \left(2 \cdot \frac{\varepsilon}{d_H} \right)^{-2} \right]. \quad (3.6)$$

The corresponding critical Reynolds number is approximated as:

$$Re_{cr,k} = \frac{378.3}{f_{cr,k}} \left(2 \cdot \frac{\varepsilon}{d_H} \right)^{-0.9} \cdot 0.355. \quad (3.7)$$

For small Reynolds numbers ($Re < 4000$) APROS uses the maximum of the friction factor of a laminar flow (3.8) [46]

$$f_{sp,k} = \frac{64}{Re_k} \quad (3.8)$$

and of the turbulent friction factor according to the Blasius equation (3.9) [46]

$$f_{sp,k} = \frac{0.316}{Re_k^{0.25}} \quad (3.9)$$

as single-phase friction factor. For Reynolds numbers between 4000 and the critical Reynolds number, the friction factor is interpolated between fully developed turbulent flow and the Blasius equation with $Re = 4000$ [40].

The two-phase friction multiplier is needed to extend the pressure drop calculation of a single phase flow and to estimate the phase distribution on flow channel wall [47]. It depends on the flow regime, using the stratification and entrainment rates as weighting factors.

At supercritical pressures the wall skin friction factor $f_{sp,k}$ for heated walls is calculated with the correlation of Kirillov et al. [48]:

$$f_{sp,k} = \frac{1}{(1.82 \log_{10}(Re_b) - 1.64)^2} \left(\frac{\rho_w}{\rho_b} \right)^{0.4}. \quad (3.10)$$

3.3 Wall Heat Transfer

For the six-equation model of APROS, there are three heat transfer zones (so-called HTZ 1 - 3) available to simulate the different heat transfer regimes [40] at subcritical pressures. HTZ 1 is defined as heat transfer in case of a wetted wall. A dry wall, where only the gaseous phase is in contact with the wall, is denoted as HTZ 3. The transition zone between wetted and dry wall is called HTZ 2. For the selection of the correct heat transfer zone, the code uses following parameters: wall tem-

perature T_w , Leidenfrost temperature T_L , saturation temperature T_{sat} , critical heat flux q_{cr} , wall heat flux q_w , and void fraction α_g .

The selection method for the three heat transfer zones is done according to the following conditions (3.11)-(3.16):

$$\text{if } \alpha > 0.99999, HTZ = 3 \quad (3.11)$$

$$\text{else if } z_{old} > 1 \ \& \ T_w \leq T_L, HTZ = 2 \quad (3.12)$$

$$\text{else if } z_{old} > 1 \ \& \ T_w > T_L, HTZ = 3 \quad (3.13)$$

$$\text{else if } q_w > q_{cr} \ \& \ T_w \leq T_L, HTZ = 2 \quad (3.14)$$

$$\text{else if } q_w > q_{cr} \ \& \ T_w > T_L, HTZ = 3 \quad (3.15)$$

$$\text{else, HTZ} = 1 \quad (3.16)$$

In case heat transfer zone 1 is selected, indicating a wetted wall, the heat is transferred by forced convection and nucleate boiling. Here, the entire heat is passed over to the liquid phase. To describe forced convection heat transfer, the Dittus-Boelter correlation [49] for circular geometries is applied:

$$Nu = 0.023 Re_l^{0.8} Pr_l^{0.4} . \quad (3.17)$$

For small Reynolds numbers the Nusselt number is limited to 3.66. The Thom correlation [50] is used to determine the heat transfer coefficient h_{nb} for nucleate boiling:

$$h_{nb} = 1971.2 e^{2p/8687000} (T_w - T_{sat}) . \quad (3.18)$$

The total heat flux is obtained by summing up the results of both mechanisms.

If the wall is dry (HTZ 3), there are three correlations implemented in the code to calculate the heat transfer to the gaseous phase. For low void fractions and mass flows, the Berenson correlation [51] is applied, which was originally developed for pool boiling but was found also reasonable for vertical flows. For forced convective heat transfer to the gas phase, which is dominant at high void fractions and mass flow rates, the Dittus-Boelter correlation is applied once again. In case natural convection is existent and the flow rate is close to zero, the heat transfer coefficient from wall to gaseous phase h_{wg} is determined according to:

$$h_{wg} = \frac{\lambda_g}{d_{Hg}} \max \left(0.401 Gr_g^{1/4} Pr_g^{1/4}, 0.12 Gr_g^{1/3} Pr_g^{1/3} \right) . \quad (3.19)$$

The Grashof number is defined as:

$$Gr_g = \frac{g \rho_g^2 d_{Hg}^3 |T_w - T_g|}{\eta_g^2 (T_g + 273.15)} , \quad (3.20)$$

with the dynamic viscosity η and the hydraulic diameter of the gas film

$$d_{Hg} = (1 - \sqrt{1 - \alpha}) d_H . \quad (3.21)$$

Finally, the largest heat transfer coefficient obtained from the three correlations is used to calculate the heat flux from the wall to the gaseous phase.

For the transition zone between a wetted and a dry wall (HTZ 2) the heat flux gets interpolated between the heat flux determined for a dry wall and the critical heat flux q_{cr} . Here, the assumption is made that the critical heat flux is equal to the heat flux of nucleate boiling, analogue to Eq. (3.18):

$$q_{cr} = 1971.2e^{2p/8687000}(T_{cr} - T_{sat})^2. \quad (3.22)$$

Eq. (3.22) can be solved for the critical temperature T_{cr} . Then, the heat flux is distributed between the liquid and the gaseous phase in dependence of the wall temperature, the critical heat flux and the Leidenfrost temperature (Eq. (3.30), (3.31)):

$$q_{wl} = \left(\frac{T_L - T_w}{T_L - T_{cr}} \right)^2 q_{cr}, \quad (3.23)$$

$$q_{wg} = \left[1 - \left(\frac{T_L - T_w}{T_L - T_{cr}} \right)^2 \right] \max(h_{wg})(T_w - T_g). \quad (3.24)$$

According to [40], the interfacial heat transfer q_{ik} is calculated for both phases, liquid and gaseous, separately. Next, the energy balance of the interface yields the phase change rates Γ due to evaporation or condensation as:

$$\Gamma = \Gamma_g = -\Gamma_l = \frac{-q_{il} - q_{ig}}{h_{g,sat} - h_{l,sat}}. \quad (3.25)$$

The specific enthalpies of saturated vapor and liquid are denoted as $h_{g,sat}$ and $h_{l,sat}$. Different heat transfer correlations are applied for phase changes due to evaporation or condensation, as described in detail in the description of the APROS six-equation model [40].

At supercritical pressure conditions, there exist only single-phase convective mechanisms for the heat transfer to the wetted wall, due to the absence of boiling. In this case, the homogeneous model [52] would be best but this, in turn, would not lead to a smooth transition to the subcritical state. As it is not possible to change between flow models, the contribution of boiling is suppressed at supercritical pressures in the six-equation model. Furthermore, the formalism of interfacial heat and mass transfer has to be extended artificially to the supercritical pressure regime. Therefore, a pseudo-critical enthalpy h_{pc} and the concept of a pseudo-critical-line are introduced [25], [53]. A constant value of 200 kJ/kg is applied for the latent heat of vaporization L_{pe} . Thus, the pseudo-saturation enthalpies can be determined as:

$$h_{l,sat}(p) = h_{pc}(p) - \frac{L_{pe}}{2}, \quad (3.26)$$

$$h_{g,sat}(p) = h_{pc}(p) + \frac{L_{pe}}{2}. \quad (3.27)$$

These definitions allow calculating the interfacial heat and mass transfer analogously to the subcritical pressure region. The fluid is treated as liquid when its enthalpy is below the pseudo-critical enthalpy and as gas when its enthalpy is above the pseudo-critical enthalpy, as illustrated in Fig. 3-1.

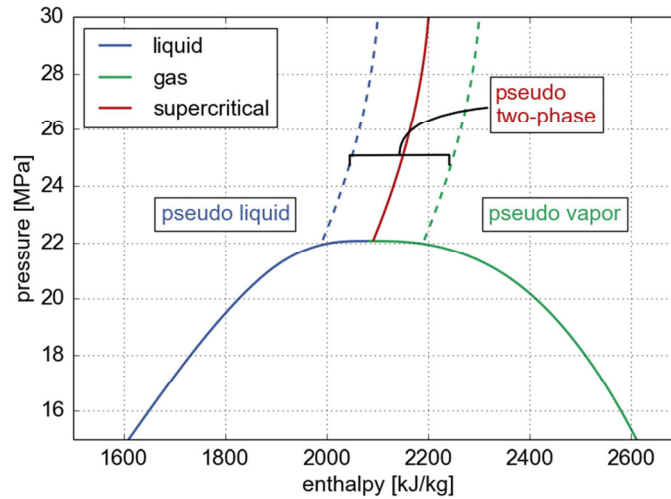


Fig. 3-1 Saturation enthalpies for liquid and gas phase. At supercritical pressures a pseudo-critical enthalpy is applied [53].

A transition zone (HTZ 2) like in the subcritical state is not needed for supercritical pressures. Furthermore, HTZ 1 is selected, if the average enthalpy is below the pseudo-evaporation enthalpy; whereas HTZ 3 is chosen for higher enthalpies. For both zones, the Jackson-Hall correlation [54] is used to predict the heat transfer coefficient, nevertheless for deterioration of heat transfer the prediction of the fuel cladding temperatures is not very precise [25]. The mentioned correlation is of Dittus-Boelter type and defined as:

$$Nu = 0.0183 Re_b^{0.82} Pr_b^{0.5} \left(\frac{\rho_w}{\rho_b} \right)^{0.3} \left(\frac{\bar{c}_p}{c_{pb}} \right)^n. \quad (3.28)$$

Here, the index b denotes bulk and the index w wall parameters. The exponent n is not constant and depends on the values of T_w and T_b in relation to the pseudo-critical temperature T_{pc} . For the conditions to be discussed in Chapter 7, it ranges between 0.4 and 0.6. The average heat capacity at constant pressure is defined as:

$$\bar{c}_p = \frac{1}{T_w - T_b} \int_{T_b}^{T_w} c_p dT. \quad (3.29)$$

When the system pressure falls to subcritical, it depends on the temperature of the wall, which heat transfer zone is activated. If the wall temperature is greater than the Leidenfrost temperature, HTZ 3 is active and the heat transfer of the dry wall is determined by the maximum of either film boiling according to Berenson [51], single phase heat transfer to the gas phase or natural convection heat transfer [40]. For wall temperatures between the Leidenfrost temperature and the saturation temperature, HTZ 2 is used. The heat flux is then interpolated between the critical heat flux q_{cr} and the heat flux over the dry wall. HTZ 1 is activated as soon as the wall temperature falls below saturation temperature. For this zone, the wall temperature is determined with the heat flux of the wetted wall.

There are different correlations implemented in APROS to calculate the critical heat flux in the six-equation model. Here, an interpolation between the Zuber-Griffith correlation [50] and the Biasi correlation [55] is chosen which depends on the mass flux. The Zuber-Griffith correlation is recommended for vertical flows and a mass flux below $300 \text{ kg/m}^2\text{s}$. As the critical heat flux gets overesti-

mated for high void fractions, this value is limited to $\alpha = 0.8$ [40]. This correlation is solely used for a mass flux below $100 \text{ kg/m}^2\text{s}$. The Biasi correlation is split up into two formulas – one for low steam qualities and another one for high steam qualities. Only the maximum value obtained from the two correlations is applied. This correlation is employed alone in case the mass flux is higher than $200 \text{ kg/m}^2\text{s}$.

Moreover, the Groeneveld-Stewart correlation [50] is used to calculate the Leidenfrost temperature. For pressures $> 9 \cdot 10^6 \text{ Pa}$ the correlation reads as:

$$T_L = [T_L(9 \cdot 10^6 \text{ Pa}) - T_{sat}(9 \cdot 10^6 \text{ Pa})] \frac{p_{cr} - p}{p_{cr} - 9 \cdot 10^6 \text{ Pa}} + T_{sat} \cdot \quad (3.30)$$

At lower pressures the following is applied:

$$T_L = 284.7 + 4.41 \cdot 10^{-5} p - 3.72 \cdot 10^{-12} p^2 - \frac{10^4 (h_l - h_{l,sat})}{(2.82 + 1.22 \cdot 10^{-6} p)(h_{s,sat} - h_{l,sat})} \cdot \quad (3.31)$$

3.4 Critical Mass Flow

The six-equation model of APROS applies two correlations to determine the critical mass flow. For liquid and two-phase flows the Moody model [56] is used, whereas the De Laval approximation is used for pure steam flows under the assumption of an isentropic flow of ideal gas through a convergent-divergent nozzle.

3.5 Non-condensable Gas

Treating non-condensable gases with APROS requires the extension of the basic six-equation model by a mass equation for the non-condensable gas itself and another equation for the concentration of the dissolved gas, according to [57]. There are four non-condensable gases available in the model; these are air, nitrogen, hydrogen and helium. However, only one gas can be simulated at a time. Furthermore, the model assumes that steam forms a homogeneous mixture with the non-condensable gas, having equal temperatures and velocities. The maximum concentration of dissolved gas in the liquid phase is a function of liquid temperature and pressure. A mass transport equation is needed to calculate the densities and pressures of the non-condensable gas in the gaseous phase of the system:

$$\frac{\partial(\alpha_g \rho_{nc})}{\partial t} + \frac{\partial(\alpha_g \rho_{nc} u_g)}{\partial z} = \Gamma_{nc} \cdot \quad (3.32)$$

The volume fraction of a phase is denoted with α . The subscripts g and nc refer to the gas mixture and to non-condensable gas, respectively. The transferred specific mass flow of non-condensable gas is indicated with Γ_{nc} , which is either positive for release or negative for dissolution.

3.6 Validation of the Commercial System Code APROS

In order to run safety analyses for the SCWR-FQT loop, the appropriateness of the commercial thermal-hydraulic code APROS Version 5.09 [35] for this task has to be approved. This is generally done by validation computations.

For this purpose, two adequate single effect experiments from literature are chosen to validate the code for predictions of transient flow phenomena, as they particularly could occur in the course accident sequences. They are characterized by highly dynamic effects, which shall be predicted with reasonable accuracy.

The water hammer experiments carried out by Fujii and Akagawa in 1993 [58] investigate hydraulic shocks as they will occur in case a pipe, which is stationary passed through by water, is abruptly closed. Such a water hammer can eventually result in surprisingly high pressure peaks. But, a simple numerical model with adapted time and space nodalization is able to reproduce the observed physical phenomena, such as the magnitude of the initial pressure wave and reflection time, in detail.

In a second experiment, a test series is performed by Becker et al. [59] and Mathisen [60] in order to examine the natural circulation in a closed loop for different heating rates and system pressures. For a stepwise power increase, the typical mass flow characteristic for boiling channels is recorded until the onset of flow oscillations. In further runs, the effect of different initial conditions on the flow stability is investigated.

Validations, published by Raqué et al. [61] and presented in the following subchapters are carried out in order to avoid additional stability analyses and water hammer simulations with specialized codes. This is justified, as the results show that APROS is able to properly predict both. Each subchapter begins with the explanation of the basic physics as well as the experimental setup and the corresponding numerical model developed in APROS. Afterwards, the outcome of the distinct numerical predictions is compared with the experimental data sets.

A third validation experiment, carried out by Köhler and Hein [62] focuses on post-dryout heat transfer conditions as they occur in case the heated test sections gets depressurized from supercritical pressure with a tube wall being above Leidenfrost temperature at the same time. Such effects may occur in the SCWR-FQT project in case of a pipe rupture at full power. However, as found from the simulation results, presented in chapter 3.6.3, APROS does not simulate a boiling crisis in these cases. For this reason, an analytical model has been developed by Schulenberg and Raqué [63] to determine the cladding temperatures under these conditions correctly.

3.6.1 Water Hammer Experiments

In case that a pipe with a constant liquid mass flow ($u = u_0$) is suddenly closed, e.g. by a shut-off valve, the inertia of the liquid induces a force on the end face. The pressure at the entrance of the valve gets increased, whereas it drops at the valve outlet. The resulting pressure wave travels with the sonic speed of the liquid in inverse flow direction through the pipe. At the same time, the flow velocity of the liquid between the valve and the pressure wave is reduced to zero, i.e. $u = 0$. In case there is a tank with a constant pressure at the inlet of the pipe, the pressure wave is reflected. This relaxation wave passes through the pipe, changing the sign of the flow velocity ($u = -u_0$). As soon as the relaxation wave is reflected at the valve once more, the flow velocity becomes zero ($u = 0$),

which causes a negative pressure jump. After another reflection at the beginning of the pipe (tank) the pressure reaches its original value again and the flow continues with its original speed ($u = u_0$). If the valve is opened at that point of time, the initial conditions would be re-established. In case the valve is still closed, another cycle begins. This process is damped in principle only by a deformation of the pipe and by the friction of the flow due to the roughness of the pipe wall.

In the planned fuel qualification test, similar shocks might occur in the event of an accident, e.g. if the test section, being filled with steam, is suddenly quenched with cold water.

The reflection time t_R , i.e. the time that is needed until the wave passes the complete pipe length, can be determined as [64]:

$$t_R = \frac{2 \cdot L}{a_S}, \quad (3.33)$$

where the pipe length is denoted by L and the speed of sound by a_S . According to the Joukowsky equation [65], the height of the pressure wave Δp is:

$$\Delta p = \rho \cdot u_0 \cdot a_S. \quad (3.34)$$

Here, ρ denotes the liquid density and u_0 the initial flow velocity.

Fig. 3-2 shows a sketch of the apparatus used by Fujii and Akagawa [58] for the water hammer experiments. The horizontal test section with a total length of 16.17 m is placed between two tanks of equal size. The inner diameter of the stainless steel duct is 21.4 mm. A fast closure valve forms the test section outlet. Inside surge tank T1, the water is heated up to nearly saturation conditions. Then, a pump permanently transfers the sub-cooled liquid from tank T1 to the upstream surge tank T2. At the inlet of the test section a submerged electrical heater produces a two-phase bubbly flow of very low quality, which passes through the test section back into tank T1. The gas volume of both tanks is filled with N_2 to achieve a constant system pressure.

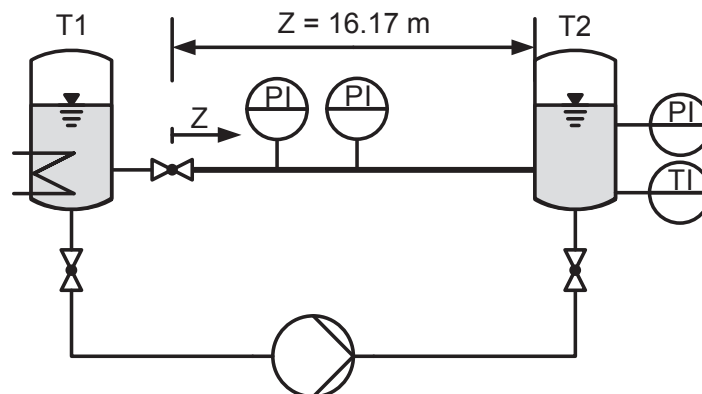


Fig. 3-2 Flow scheme of the water hammer experiments of Fujii and Akagawa [58].

The experiments, presented in Fig. 3-2, started with stationary flow conditions: a flow velocity of 1 m/s and a water temperature of 160 °C. The first run is performed at a system pressure of 0.7 MPa, which means a sub-cooling of $\Delta T_{sub} = 5$ °C. The boundary condition for the second run is given by a pressure of 0.9 MPa, which results in 15 °C sub-cooling. The third run is performed at an initial

pressure of $p_0 = 1.3 \text{ MPa}$ ($\Delta T_{sub} = 30 \text{ }^\circ\text{C}$). The corresponding saturation pressure of water at $160 \text{ }^\circ\text{C}$ is 0.62 MPa . By abruptly activating the fast closure valve – the closing time ranges between 9 to 15 ms – and operating the two solenoid valves, a pressure wave can be observed travelling through the test section. The test section is equipped with pressure sensors at several positions to measure the pressure pulse. The published experimental data [58] is taken and analyzed with APROS for validation purposes.

According to equations (3.33) and (3.34), the reflection time t_R and the height of the Joukowsky pressure surge Δp of these experiments are predicted as listed in Tab. 3-1.

Tab. 3-1 Reflection time and Joukowsky pressure surge obtained for 0.7, 0.9 and 1.3 MPa.

$p \text{ [MPa]}$	$\rho \text{ [kg/m}^3\text{]}$	$a_s \text{ [m/s]}$	$\Delta p \text{ [MPa]}$	$t_R \text{ [s]}$
0.7	911.2	1443	1.315	0.022
0.9	912.4	1444	1.317	0.022
1.3	914.7	1445	1.321	0.022

For the system code simulations with APROS, the six-equation thermal-hydraulic model is applied. The simulation time step is fixed to 0.1 ms. As depicted in Fig. 3-3, the numerical setup, which is based on the model developed by Herbell [66], consists of the test section with the fast closure valve on the left side, the two surge tanks and the shut-off valve of tank T2. The 16.17 m long test section is represented by 165 calculation nodes. Furthermore, the pressures of tank T1 and at the intake of tank T2 are fixed as boundary conditions. The inlet pressure is adjusted to gain the initial flow velocity of 1 m/s.

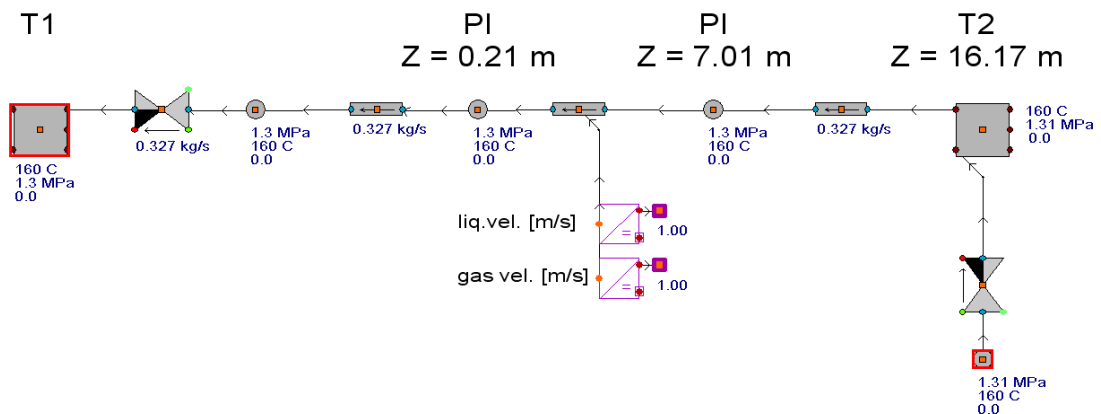


Fig. 3-3 APROS model of the water hammer experiments.

Fig. 3-4 compares the simulation results obtained with the numerical model (lines) versus the experimental results (markers) for three initial pressures p_0 at different measurement locations. The plotted experimental data points are extracted from [58] in steps of 2 ms.

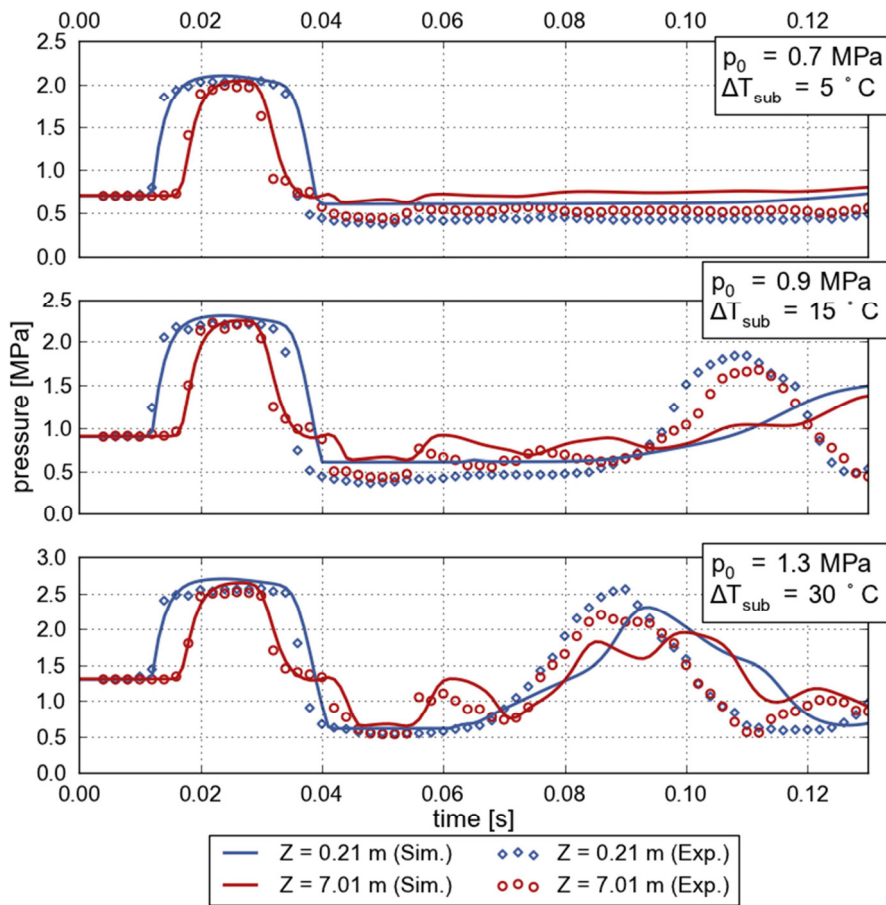


Fig. 3-4 APROS simulations and experimental results of the water hammer experiment [58] for initial pressures of 0.7 MPa, 0.9 MPa and 1.3 MPa.

In general, simulation and experimental results agree well. The first pressure step of 1.3 MPa, predicted by Eq. (3.34) is found in the experimental data and in the simulation of all three cases with an error of less than 0.1 MPa. After the first reflection at the fast closure valve at about $t = 40$ ms, the predicted pressure remains at 0.62 MPa at minimum, which is the saturation pressure for the initial temperature of 160 °C. Note that Fujii and Akagawa measured a pressure which is slightly lower than the saturation pressure, eventually caused by a lack of nucleation sites in the water. After multiple reflections, the APROS simulations become more and more uncertain, but they still reflect the observed trend properly. Accordingly, APROS detects water hammer phenomena if the time step is chosen sufficiently small compared with the reflection time.

However, it has to be mentioned that APROS is not selecting such a small time step automatically. The automatic time step selection is based solely on the requirement that the mass conservation equations are fulfilled. Thus, the user is responsible for selecting the maximum allowed time step so that all relevant phenomena are captured, i.e. dt_max should be less than the characteristic time of the interesting phenomenon.

3.6.2 Natural Circulation in a Closed Loop

Two-phase flow in a closed loop, driven by natural circulation due to an external heat source, is a very sensitive test for numerical models and their interfacial friction forces. In boiler tubes at low heat input, a bubbly flow will raise the fluid. At first, the coolant mass flow rate increases with increasing power. At elevated heat exposure, the flow pattern in the upper part of the heated section will become an annular flow and growing friction pressure losses will decrease the flow rate with further increasing power again. The mass flow is thus reaching a maximum between these two regimes. Finally, above a certain critical power level, density wave oscillations will cause flow instabilities with violent mass flow pulsations. An inlet orifice, upstream of the heated section, can shift the onset of instabilities to a higher power level, whereas an outlet orifice causes the instabilities to occur at lower power.

Numerous experiments have been performed by Becker et al. [59] and Mathisen [60] to study the onset of instabilities depending on different parameters, such as throttling at the outlet of the test section and varying the inlet sub-cooling. Fig. 3-5 schematically depicts the flow scheme of the experimental natural circulation loop ‘Skälvan’ at Studsvik [60].

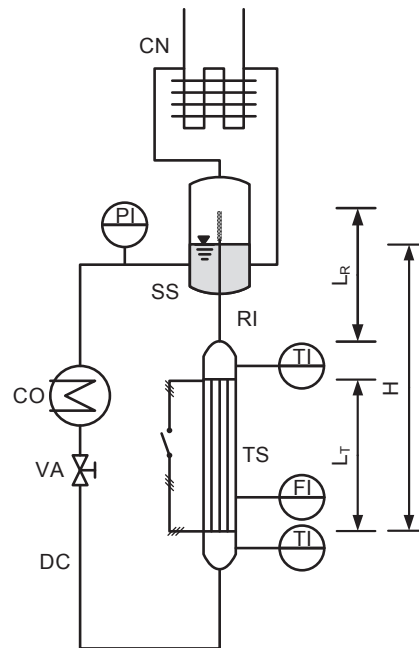


Fig. 3-5 Flow scheme of the natural circulation loop [60]; TS: test section, CN: condenser, DC: downcomer, H: effective head, L_R : riser length, L_T : test section length, RI: riser, SS: steam separator, CO: sub-cooler.

The test section of the loop is formed by a vertical stainless steel pipe of length $L_T = 4.89$ m and 20 mm inner diameter. It is electrically heated with a given power. After passing the heated section in upward direction the steam-water mixture flows through a riser ($d_i = 36$ mm) of length L_R , which ends up as a sparger inside a steam separator. The sparger is formed by a pipe perforated with 96 holes of 8.2 mm diameter. The steam is condensed in an air-cooled condenser and the liquid returns through a downcomer to the inlet of the test section. The inner diameter of the downcomer is $d_i = 51$ mm. A sub-cooler is applied to adjust the inlet temperature of the water. For all experiments, the effective head $H = 5.835$ m.

A reliable prediction of this phenomenon with APROS is also relevant for the SCWR-FQT project, as it is intended to increase the robustness of the safety concept by adopting natural convection for passive long-term heat removal [67]. In the numerical model of the natural circulation boiling channel, the test section is modeled with the APROS module pipe with heat structure. For simplification, the steam separator with attached condenser CN is not part of the model, but the static pressure at this point is applied as inlet and outlet boundary condition of 4 MPa, as shown in Fig. 3-6.

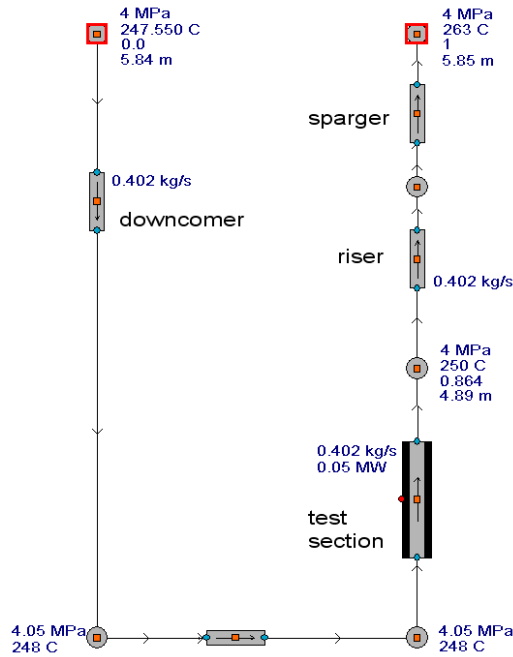


Fig. 3-6 APROS model of the natural circulation experiments.

The heated length is subdivided by 1000 nodes. Throughout all simulations, the heating power is increased in steps of 0.01 MW (= 6.5 kW/l power density in the heated section) until the flow begins to oscillate. Fig. 3-7 shows exemplarily the system response close to the stability limit predicted with APROS.

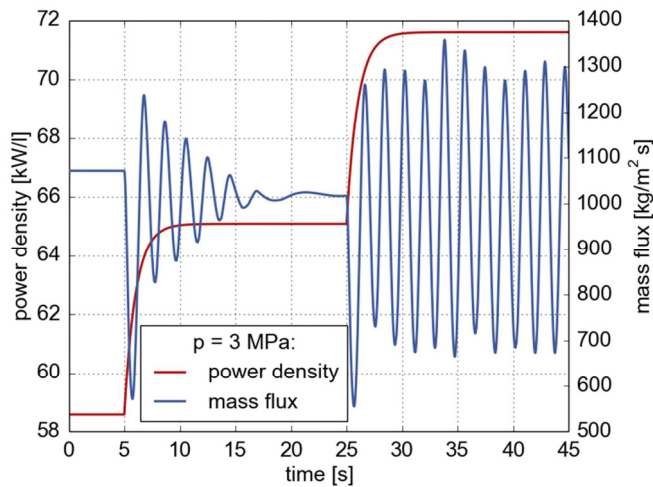


Fig. 3-7 Mass flux oscillations close to the stability limit.

Simulation results which are presented in the following figures 6 to 8 end with the last stable simulation point. Again, the six-equation model is applied for a detailed physical description of two-phase flow phenomena.

As the wall roughness of the experimental duct is unknown, the following simulations are performed applying the default relative roughness (absolute roughness divided by the hydraulic diameter of the pipe) of 10^{-5} . Moreover, the form loss coefficients for the two 90°-elbows are assumed to be 0.14 [68]. The pressure loss in the system is calculated according to chapter 3.2.

The first set of simulations investigates the effect of system pressure on the flow dynamics. In the experiments, the static pressure level inside the steam separator is varied between 1 and 7 MPa. At the same time the sub-cooling ranged between 2.1 °C and 5 °C. For each pressure, the heating power is increased until the flow becomes unstable or burnout conditions are reached.

As visible from the experimental data (markers) in Fig. 3-8, the onset of instability shifts to higher power levels with increasing system pressure. At pressures higher than 6.5 MPa, dryout is observed at the stability limit.

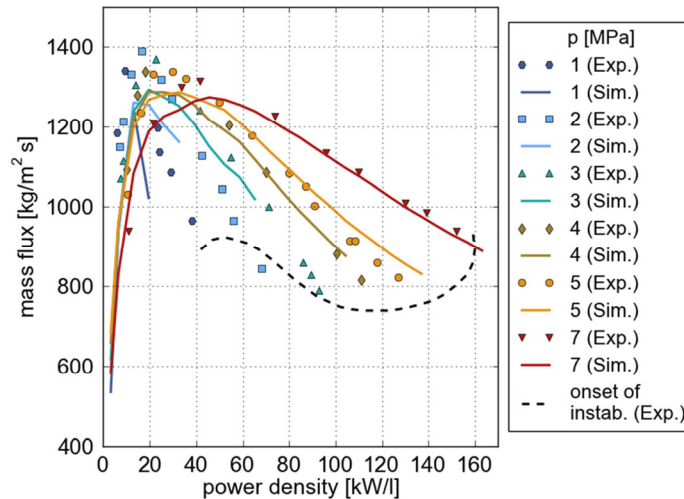


Fig. 3-8 Comparison of experimental [59] and simulation results for the effect of pressure on natural circulation.

The obtained simulation results, illustrated as solid lines, are also depicted in Fig. 3-8. Onset of instability is predicted within an interval of 6.5 kW/l after the end of each solid line. In general, the numerical code reproduces the typical characteristic of both: first the increasing and then the decreasing mass flow rates with increasing power. In detail, the simulations for a pressure of 7 MPa show that the onset of instability, as well as the mass flux for high power densities is in agreement with the experimental data. With decreasing pressure, the code underestimates the mass flux. Boiling with an exit void fraction around 0.8, when the highest mass flux is achieved, is underestimated by the code compared to the experimental data. The predicted peak mass flow rate differs in general from the measured one by approximately 4 % at 7 MPa to around 9 % at 2 MPa. The onset of instabilities, which agrees well with the measured limits at 7 MPa, is generally under predicted at lower pressures. Note a factor of two between predicted and measured onset of instabilities at a pressure of 2 MPa.

In the experiments, the influence of outlet orifices is evaluated by reducing the number of sparger holes. Thus, different flow area ratios A_0/A have been studied, where A is the cross section of the heated duct and A_0 is the total cross section of all sparger holes. These runs are performed with a constant sub-cooling of approximately $2\text{ }^\circ\text{C}$ and a pressure of 5 MPa . The applied A_0/A ratios are 16.15, which corresponds to a maximum number of 96 holes, 0.655 (4 holes), 0.492 (3 holes), and 0.329 (2 holes). Fig. 3-9 illustrates that an increasing outlet throttling results in an earlier onset of instabilities and in decreasing mass fluxes. APROS predicts this effect quite well with the exception of the smallest outlet cross sections which overestimated the onset of instabilities.

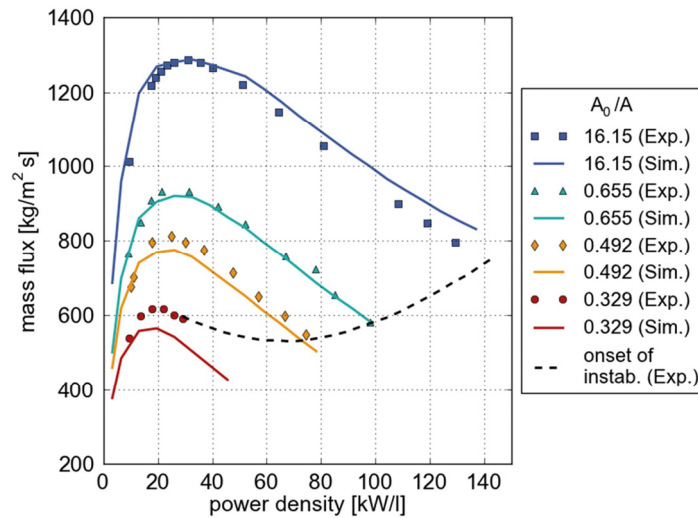


Fig. 3-9 Effect of outlet throttling on flow stability. Experimental data [59] (markers) and simulation results (lines).

Another test series examines the influence of inlet sub-cooling for a constant system pressure of 5 MPa . Fig. 3-10 depicts the predicted and measured mass fluxes versus power density.

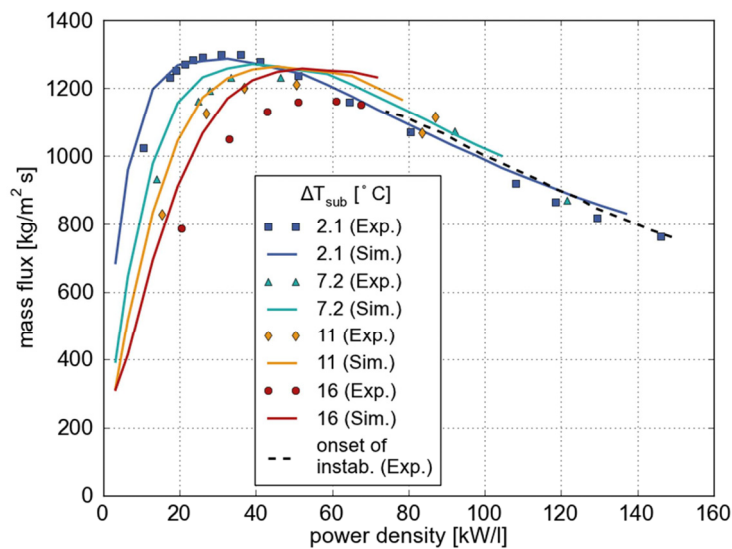


Fig. 3-10 Effect of inlet sub-cooling on flow stability. Experimental data [59] (markers) and simulation results (lines).

As visible, an increased inlet sub-cooling leads to a reduced stability of the flow. In the experiments the amount of inlet sub-cooling varies between 2.1 °C and 16 °C. The effect that a higher sub-cooling leads to an earlier onset of instabilities is also found in the simulation results. However, slightly higher mass flow rates are reached before the flow begins to oscillate. At the same time, the maximum possible heat input is slightly underestimated by the numerical model by less than 10 %.

A sensitivity analysis on the pressure dependency of two-phase flow in the test section shows that the wall roughness has a strong influence on the predicted results. Increasing the relative roughness of the test section to $3.15 \cdot 10^{-4}$, which corresponds to an absolute roughness of 6.3 µm, further reduces the mass flux shown in Fig. 3-8; however, the onset of instability occurred still at the same power. The maximum error in mass flux compared with the experimental results is increased to 9.5 % at 7 MPa and to 13 % at 2 MPa. A mean error of -7.9 % (standard deviation = 2.2 %) is determined for all ten measurement points at a pressure of 7 MPa. In comparison, the data set of Fig. 3-8 yields a mean error of only 2.8 % with a standard deviation of 2 %.

Discussion

Two one-dimensional models are developed with the commercial system code APROS to be validated against experimental data. Both experiments investigated transient flow phenomena, which could be captured by the numerical simulations with good accuracy. The magnitude and reflection time of the pressure wave observed in the water hammer experiments are predicted with high precision for all examined pressure levels. The output of the second APROS model shows that the mass flow characteristic for a natural circulation loop with boiling channel is captured by the code in general. Furthermore, the onset of instability is predicted with the model such that additional linear analyses are not required. However, the accuracy decreases with decreasing pressures. Best agreement is achieved in the pressure range of 5 to 7 MPa. Moreover, the maximum attainable mass flux is underestimated by the code for the natural convection loop. It is found that the wall roughness significantly affects the simulation results for two-phase natural circulation flows. Taken as a whole, one can say that APROS describes the examined flow phenomena with appropriate accuracy. For this reason, the code is regarded suitable for the performance of safety analyses and to support the design process in the SCWR-FQT project.

3.6.3 Depressurization Transients

In case the loop gets depressurized from supercritical to subcritical pressure and the cladding temperature has been above Leidenfrost temperature before, there is the risk of temporary temperature peaks by running into film boiling or post-dryout conditions, which are characterized by a very low heat transfer. A subsequent developing process of rewetting of the dry region, which is called quenching, can be achieved due to heat conduction to the wetted region inside the metal tube going along with a decline of wall temperature below Leidenfrost temperature. Such a scenario could be caused by a small break LOCA or by malfunction of the pressure control system. In such case, it is likely to occur even when the critical heat flux was never exceeded.

a) APROS Simulation of a Boiler Tube Experiment

Köhler and Hein [62] investigated this process experimentally with the Benson test facility. A significant worsening of post-dryout heat transfer was found, which occurred in the proximity of the critical pressure during a slow depressurization transient from the supercritical pressure region. Their

experimental setup consists of a high pressure loop connected to a vertical test section. This boiler tube, with an inner diameter of 14 mm, a wall thickness of 2 mm and a length of 6 m, is operated in a once-through mode. A piston pump provides an upward mass flow with a velocity of $2000 \text{ kg/m}^2\text{s}$. The heating of the test section is performed by direct current, uniformly distributed in axial and circumferential direction. The applied heat flux is 619 kW/m^2 and the enthalpy of the water at the inlet of the test section is 1625 kJ/kg . The experiment starts with steady-state conditions. Within the first 165 seconds, the pressure at the test section outlet is gradually decreased from 24.7 MPa to 19 MPa by injection of cold water into the connected pressurizer. The pressure ramp applied on the test section outlet is depicted in Fig. 3-11.

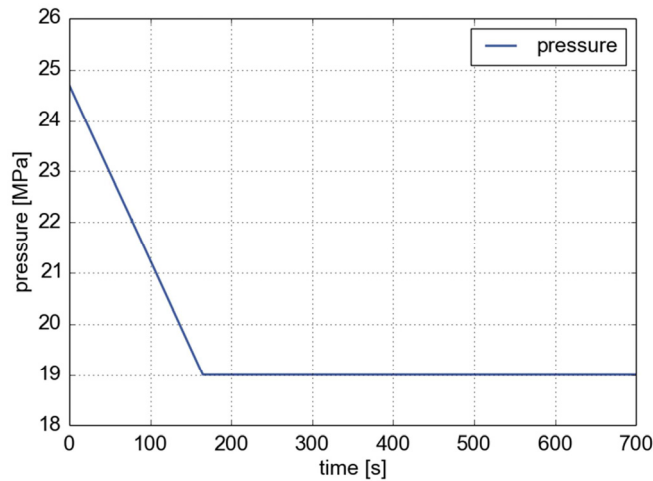


Fig. 3-11 Pressure ramp applied at the tube outlet.

The diagram in Fig. 3-12 shows the experimental results as wall temperatures over specific enthalpy of the fluid.

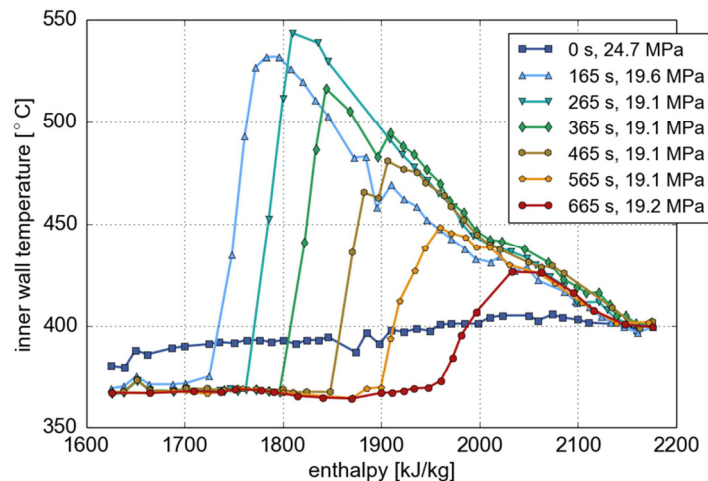


Fig. 3-12 Progression of tube wall temperature during a slow depressurization [62].

At the initial state, the pressure is 24.7 MPa and the wall temperatures are in the range of 380 to 400 °C. After 165 seconds a steep wall temperature increase takes place at the location where the boiling crisis occurs, which is close to the test section inlet.

These experimental results are used to validate the capability of APROS to predict post-dryout heat transfer regime and the moving of a quench front after a slow depressurization from supercritical to subcritical pressure. The numerical model is illustrated in Fig. 3-13. It mainly consists of a pipe with heat structure, where the heat input is defined. The pipe is discretized in axial direction by 600 nodes. The pressure ramp is defined by a boundary condition at the outlet point 4. A constant mass flow of 0.308 kg/s is applied over pipe 1, which is taken out of the simulation, while the inlet enthalpy of 1627 kJ/kg is given by point 1 in the same manner. This setup is based on the model developed and described in detail in the diploma thesis of Szygalski [69].

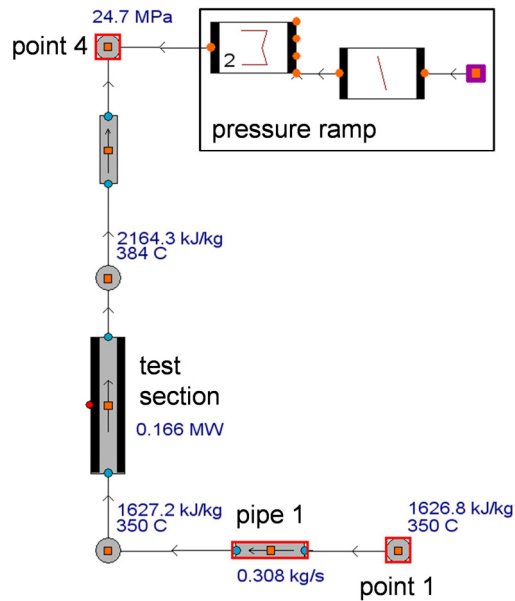


Fig. 3-13 Simulation setup in APROS.

Simulation results depicted in Fig. 3-14 show neither post-dryout conditions nor a transient moving of the quench front when passing the critical pressure.

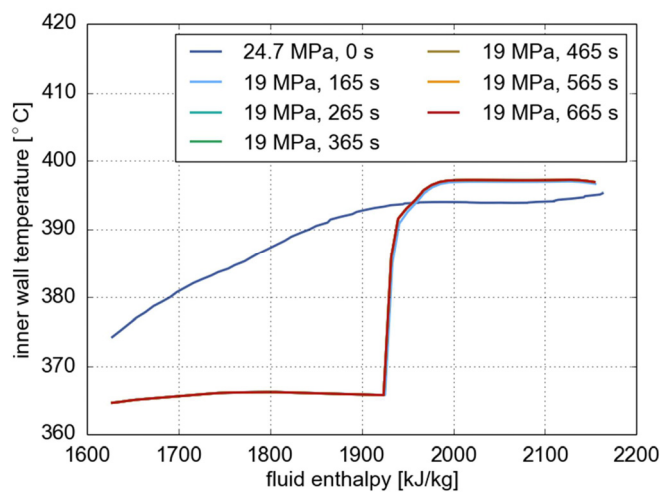


Fig. 3-14 APROS results: inner wall temperature over fluid enthalpy.

In fact, immediately after reaching the lower pressure level of 19 MPa, steady-state equilibrium conditions are reached and the wall stays wetted (HTZ 1) over the complete simulation time. The reason for this erroneous prediction can be found when looking at the decision criteria for the applied heat transfer zone, as described in Chapter 3.3. The boundary conditions at the beginning of the experiment are a pressure of nearly 25 MPa and a pseudo void fraction α_{pc} of zero, which results in heat transfer zone 1 (wetted wall). After depressurization to the subcritical pressure state, the wall heat flux q_w is smaller than the critical heat flux q_{cr} but the temperature of the wall T_w is greater than Leidenfrost temperature T_L . In this case, the decision criteria of APROS still predicts a wetted wall (HTZ 1), however, in reality the wall is dry.

b) Analytical Model for Depressurization Transients

As shown by the validation analysis, the effect that a surface is hotter than Leidenfrost temperature when passing the critical point from super to subcritical pressure, which would avert the wetting of the surface and thus leads to a temporary boiling crisis, has not yet been properly included in the APROS code.

For this reason, a model has been developed by Schulenberg and Raqué [63], which allows the analytical prediction of the surface temperatures during an eventual boiling crisis in the short depressurization period in the course of an accident sequence. The model uses a quasi-steady-state approach, meaning steady-state heat transfer correlations and fluid enthalpy distribution but transient heat conduction in the tube wall, respectively fuel cladding. For the supercritical pressure region the explicit heat transfer correlation of Cheng et al. [70] is applied. Moreover, at critical pressure, the critical temperature is equal to the Leidenfrost temperature, which allows defining the location of the quench front. At subcritical pressure conditions, the Rohsenow correlation [71] is applied to calculate the heat transfer coefficient k_{wet} for nucleate boiling in case of a wetted wall ($T_w < T_L$). If the wall temperature is above Leidenfrost temperature, indicating a dry surface, the heat transfer coefficient k_{dry} is determined according to the correlation of Groeneveld and Delorme [72] for non-equilibrium, post-dryout conditions.

The fast heat up of the cladding at the peak power location can be predicted with the transient heat balance Eq. (3.35), disregarding axial heat conduction in a fuel cladding:

$$\rho c_p A \frac{\partial T}{\partial t} = q' - k \pi d (T - T_{sat}). \quad (3.35)$$

Here, ρ and c_p denote density and specific heat of the cladding material. The local linear heat rate of a fuel rod is denoted as q' . A is the cross section of the cladding and d the outer fuel rod diameter. The heat transfer coefficient k is determined depending on the heat transfer regime as described above. It can be either k_{wet} or k_{dry} .

Comparing the analytical results with the experimental data of Köhler and Hein [62] shows good agreement, as demonstrated in [63]. A first exemplary application to the in-pile test is presented in [34], which points out the necessity to scram the reactor before reaching subcritical pressures in order to avoid a boiling crisis with potential fuel rod damage. In Chapter 7, this model will be supplementary applied on the APROS results with the aim to examine the cladding temperature progression during the first seconds of each accident sequence.

Discussion

A prediction of wall temperature peaks during post-dryout conditions in the course of depressurization transients is not yet possible with APROS. For this purpose, an analytical model has been developed assuming quasi-steady-state heat transfer conditions but transient wall temperatures. This aims at completing the safety analyses for the fuel qualification test by calculating the peak temperatures after sudden pressure drops during the relevant period of analyzed accident sequences.

3.7 Code-to-code Comparison of APROS and ATHLET

A code-to-code validation is performed applying the system codes APROS Version 5.09, which is used within the present thesis, and the related best estimate thermal-hydraulic code ATHLET Mod 2.1 Cycle A. [73], basically developed by Gesellschaft für Anlagen- und Reaktorsicherheit (GRS) for safety analysis of light water reactors. Similar to APROS, ATHLET is validated for nuclear applications. However, this code also required a modification for supercritical water conditions as described by Zhou et al. [74]. For this modification, named ATHLET-SC a methodology similar to the one described by Hänninen and Kurki [25] is applied. Thus, extended water steam-properties are used and a pseudo two-phase method is adopted. Amongst others, the Bishop correlation [75] is implemented for the prediction of heat transfer coefficients in the supercritical pressure region. This correlation is selected for the simulations presented here. The aim of this code-to-code comparison is not primarily the validation of the physical models but rather the elimination of input errors and the avoidance of incorrect use of the codes. For this reason, the setup of the numerical models is developed independently by different users. The ATHLET model of the loop has been programmed by Zhou [76]. Both numerical models are based on the same but earlier design stage of the SCWR-FQT loop. In the following, simulation results obtained with both codes for the cases of design operation, as well as for a break of the feed line are compared against each other. These and further compared accident analyses are documented in more detail in the SCWR-FQT project deliverable E3.1 [77].

Fig. 3-15 shows the coolant temperature progression inside the test fuel element obtained for design operation of the loop with ATHLET (circles) and with APROS (solid lines).

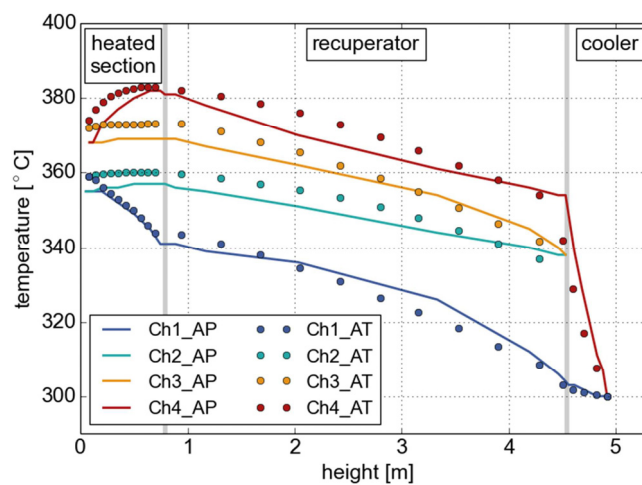


Fig. 3-15 Coolant temperatures inside the flow channels of the test fuel element at design operation, predicted with ATHLET (AT, circles) and with APROS (AP, solid lines).

The assumed fissile power is 53 kW plus additional 23 kW of gamma power. The design coolant mass flow rate of 0.25 kg/s is provided by pump HCC. The diagram shows the coolant temperatures inside the four flow channels created by the pressure tube and the internals, which are plotted against the height of the fuel element.

The coolant enters the outermost channel 1 (Ch1) through the test element head piece at a height of 4.9 m (Fig. 2-4). In the core section, a considerable heat-up occurs due to gamma heat released in the pressure tube. Reaching the bottom, the flow direction changes and the coolant passes channel 2 (Ch2) in upward direction (Fig. 2-3 left). Turning downward again, the coolant gets further preheated when passing the shell side of the recuperator (Ch3) (Fig. 2-3 right). After changing its flow direction one more time, when reaching the closed bottom of guide tube 2, a second considerable temperature increase of the coolant takes place inside the assembly box (Ch4). At the top of the fuel rods a maximum temperature of 383 °C is predicted by both codes, before the coolant gets cooled down again to 300 °C, passing the recuperator and the cooler section located above.

Comparing both steady state analyses, good agreement of the coolant temperature distribution inside the fuel element is found. Minor deviations have the same order of magnitude as the heat transfer correlation applied in ATHLET (cp. [77]).

For a code to code comparison of an accident analysis, a complete rupture of the feed line L1 has been postulated. The accident is initiated at $t = 0$ s, as shown in the simulation results for the progression of coolant temperature and pressure at the top of the test section, depicted in Fig. 3-16. In the course of this accident, the flow direction in the test fuel element is reversed, as accumulator TZ1 and pump HC1 feed straight into the break. Thus, the ELCI system is used to quench and cool the test section. The results obtained with ATHLET (denoted with *_AT*) are illustrated with markers, whereas the APROS results (denoted with *_AP*) are shown as solid lines.

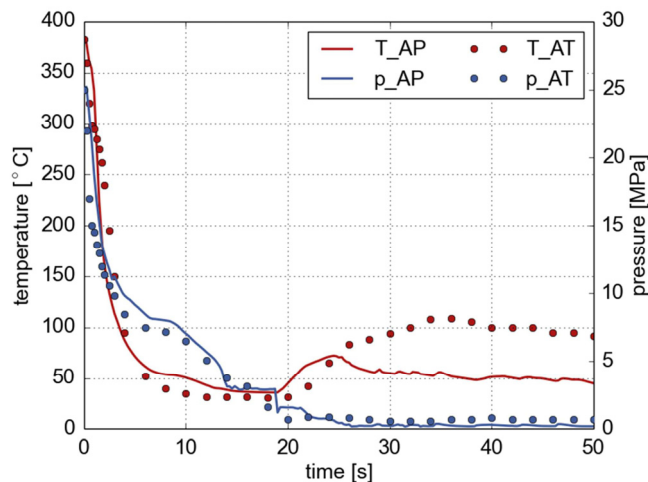


Fig. 3-16 Coolant pressure and temperature inside the test section for a break of the feed line L1. Simulation results of ATHLET (AT, markers) and APROS (AP, solid lines).

Both codes predict a sharp coolant temperature decrease right after the break of the feed line. This is caused by the high water mass flow rate injected on top of the fuel rods via emergency cooling line L3, being followed by the active residual removal operated by pump HC2. The emergency coolant mass flow rates are depicted in Fig. 3-17.

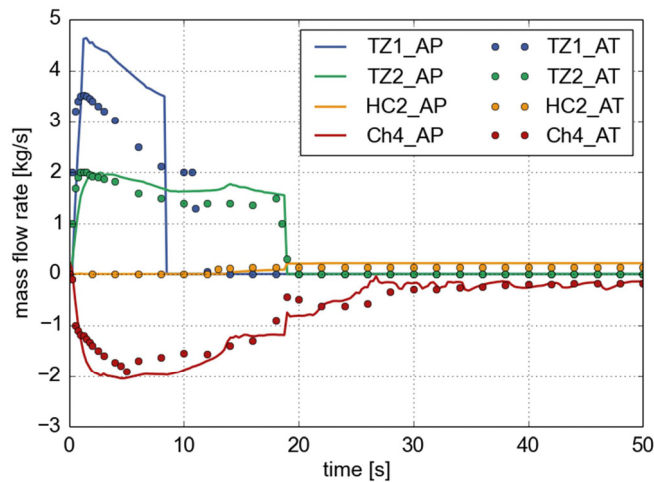


Fig. 3-17 Emergency coolant injection provided by the accumulators TZ1, TZ2 and emergency pump HC2 and the resulting mass flow rate through the assembly box Ch4 for a break of feed line L1. Simulation results of ATHLET (markers) and APROS (solid lines).

Again the ATHLET results are illustrated with circles and the APROS results with solid lines. Both codes predict a consistent depressurization period of 18 seconds, according to the injection period of accumulator TZ2. Afterwards, a temperature increase is found in both results, which is a result of the lower emergency coolant mass flow provided by pump HC2. However, the temperatures predicted with ATHLET are slightly higher and decrease slower than predicted with APROS. This deviation is caused by different assumptions for the coolant mass flow rate provided by pump HC2. For the ATHLET simulations, a mass flow of 0.1 kg/s has been applied, which is half the value assumed in APROS. Moreover, the discharge of accumulator TZ1, which is feeding into the break, takes place more slowly in the ATHLET simulation.

Similarly good agreement between the results of ATHLET and APROS is demonstrated for rupture simulation of the return line and the emergency cooling line, as presented in [77].

Discussion

A code-to-code comparison between the system codes APROS and ATHLET showed good agreement for the regarded design basis accident. Thus, a correct implementation of the loop geometry can be assumed. The validation of heat transfer models was not the aim of this comparison. Instead, this will be in the focus of ongoing research for the supercritical and near critical pressure region. For this purpose, more experimental data of supercritical water reactors will be required. Such data is expected e.g. from the electrically heated SWAMUP test facility [78], which has already been erected at the Jiao Tong University of Shanghai. In the near future, this facility will provide experimental data, which will be close to the planned fuel qualification test conditions.

4 Numerical Model of the Loop

For the simulation of the SCWR-FQT loop with all safety-relevant components, as schematically depicted in Fig. 2-6, the commercial system code APROS version 5.09, described in Chapter 3, is applied. A first conceptual design has been developed by Schneider, which is presented in [79]. As several parts and components of the loop cannot be modeled by given standard components of the code, alternative ways for modeling have to be found. This chapter presents such implementations, set up for certain components with the help of basic modules that are implemented in the code. The numerical model consists of 892 thermal hydraulic nodes and 446 automation signals and is divided into sub models. The use of such nets is a convenient method, provided by APROS, to gather components that belong to certain sections of the system in individual GUI windows. Thus, a clear and structured overview of the numerical project can be achieved. The SCWR-FQT facility is composed by the following six nets, which can be seen in Annex A: the first two nets cover the primary and secondary circuits with the exception of the test fuel element, which itself is split up into three nets: cooler, recuperator and heated section. The last net represents the control window for the thermal-hydraulic model as well as for the emergency systems. These nets communicate with each other via so-called reference copies – duplicate components which occur in several nets. The application of this model allows performing numerous safety analyses for the prediction of the system response to design basis (Chapter 7) and beyond-design-basis (Chapter 8) accidents. Furthermore, the code is a highly useful tool for dimensioning and optimization of the system design and the emergency system settings. An example of the latter is given by a parametric study of channel and structure dimensions. A flow area variation of the fuel element connection nozzles (Chapter 6) yields an optimum tradeoff between a high pressure loss during normal operation, on the one hand, and a deformation of the weak internals due to impermissible pressure gradients across walls during depressurization transients, on the other hand.

4.1 Multichannel Configuration of the Test Fuel Element

The heated section is located in the bottom part of the test fuel element. It consists of four UO_2 fuel rods of 60 cm length with a fissile power of 15.9 kW each. In total, the heating power equals to 73.4 kW including 9.8 kW of gamma power, which is mainly released by the pressure tube surrounding the test section. The assumed axial power profile, predicted with the Monte Carlo code MCNP by Dostal [80], is of bottom peaked shape as plotted in Fig. 4-1:

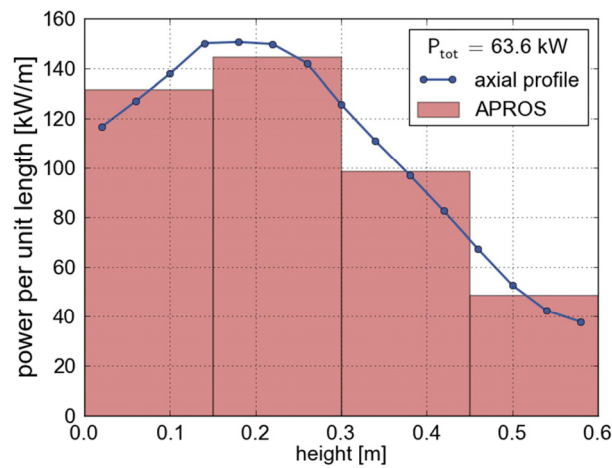


Fig. 4-1 Bottom peaked axial power profile [80] with corresponding four segment power distribution, as assumed for APROS analyses at design conditions.

In the APROS model, the fuel rods are axially divided into four segments of 15 cm length. Thus, the corresponding power distribution is 19.8 kW, 21.7 kW, 14.8 kW, and 7.3 kW from bottom to top.

It is not possible to model the heat transfer between the parallel flow channels of the test fuel element with standard components implemented in APROS. Heat exchanger components provided in APROS exchange heat only with a single neighboring channel. However, the multichannel configuration of the test section is forming a co-axial flow path, which often exchanges heat across two walls with two neighboring flow channels. For this reason, a numerical model of the test section was assembled manually by the use of APROS basic modules. The modeling of one axial segment of the heated section with APROS is shown in parts in Fig. 4-2. Every channel consists of a node (TH node) and a branch (TH branch) for each segment. In the staggered grid discretization of APROS, the variables of state, pressure and enthalpy, are computed in the center of a node resembling a computational cell. These nodes describe the shape of the flow volume. A branch resembles the border of a computational cell and links two nodes. Here, mass flow and pressure loss are computed.

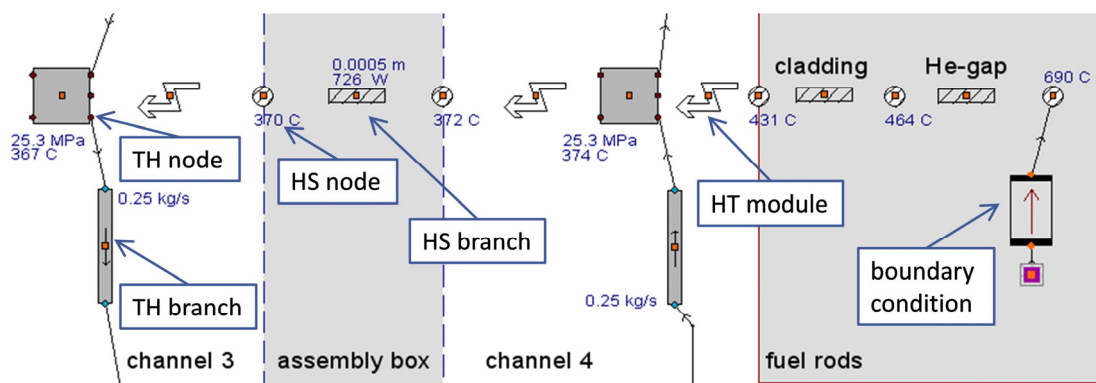


Fig. 4-2 One segment of the heated section as modeled with APROS.

To model the heat transfer over the wall between two nodes, located at the same height of two neighboring channels, three different module types are used, as depicted in Fig. 4-4. The two surfaces of a wall are modeled by two heat structure nodes (HS node). These nodes are described by the

applied coordinate system, their heat transfer area and their angle towards the horizontal, which is compared with the flow direction. In the heat structure nodes the surface temperature is calculated. A heat structure branch (HS branch) thermally connects two heat structure nodes with each other and calculates the heat flow through the wall with respect to the thickness of the wall and its material. A heat transfer module (HT module) links a heat structure node with the thermal-hydraulic node of a related flow volume. To calculate the heat transfer coefficient for the respective side of the wall, the heat transfer area as well as the thermal hydraulic diameter is needed. If these values are not explicitly entered by the user they are automatically deduced from the geometries of the connected thermal hydraulic and heat structure nodes.

The heat input of the fuel rods is modeled as a volumetric heat source according to the schematic drawing of Fig. 4-3. For this purpose, the UO_2 pellets are radially subdivided into three segments. Each segment consists of two heat structure nodes (HSN) which are linked by a heat structure branch. The fissile power (Fig. 4-1) is assigned to each of these three segments according to their volume fraction. The 0.5 mm helium gap between fuel and cladding is represented by another heat structure branch (HSB). Identically, the heat conduction through the cladding is modeled. Finally, a heat transfer module HT6 is applied for the heat transfer to the fluid node NO6. By setting the variable number of parallel heat structures in the heat structure nodes to 4, all fuel rods are modeled collectively.

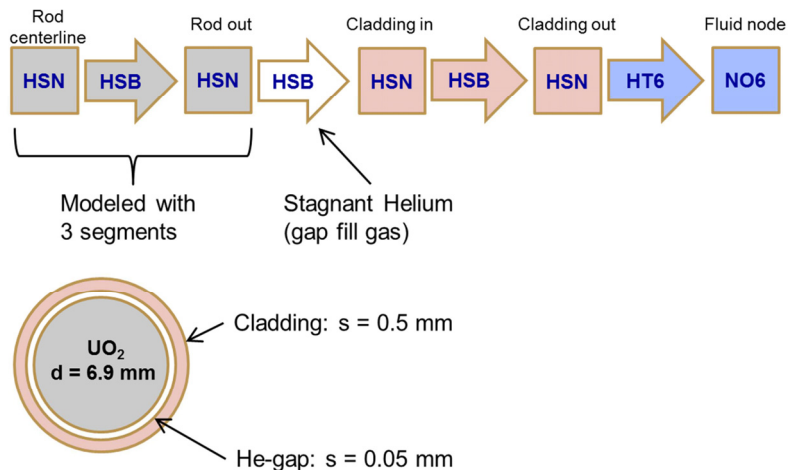


Fig. 4-3 Schematic composition of the fuel rod model used in APROS.

It is assumed that the gamma power of 9.8 kW is equally released over the height of the core. The distribution to the four sub channels is conducted according to the mass fractions of the guide tubes and the pressure tube. The heat input released from the guide tubes is evenly distributed to the adjacent sub channels as listed in Tab. 4-1. Thus, approximately 90 % of gamma heat is transferred to channel 1 due to the surrounding thick-walled pressure tube. Boundary conditions are used to model the gamma heat input in consideration of the respective heat transfer area. The gamma power released from the fuel rods of 2.4 kW in total is already included in the fuel rod power of 63.6 kW.

The modeling of the recuperator and cooler sections is implemented in the same way. Both sections are axially subdivided into seven segments of variable length.

Tab. 4-1 Gamma power distribution on flow channels according to the mass fraction of structural internals of the test fuel element.

	Channel 1	Channel 2	Channel 3	Channel 4
Ratio [%]	89.9	5.7	3.3	1.1

For design operation, the following temperature profiles, illustrated in Fig. 4-4, arise along the radius of the fuel rods:

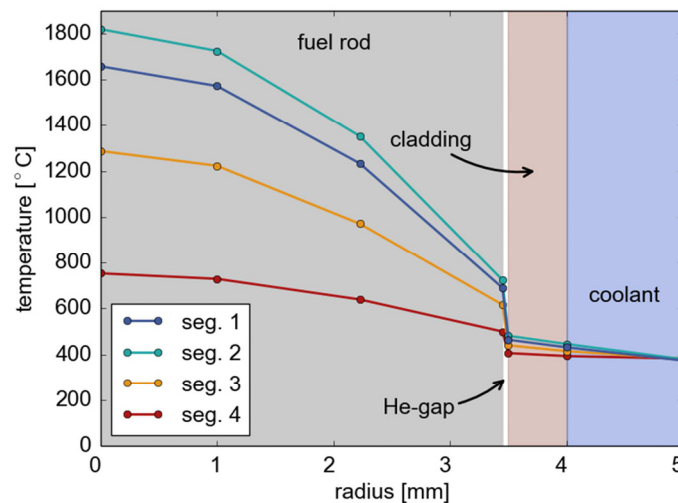


Fig. 4-4 Radial temperature profiles along the heated length.

The maximum fuel centerline temperature of 1818 °C occurs in in the second lowest segment were the heat flux is highest (cp. Fig. 4-1).

4.1.1 Coolant Density Feedback

The Monte Carlo N-Particle Code MCNP5 [81] has been applied by Vasari [82] for preliminary simulations of the neutron flux in the LVR-15 reactor core containing the test fuel element. In these simulations, the core is represented by a box of 80 vertical channels arranged in an 8x10 square grid with a pitch of 7.15 cm. A box height of 54 cm is assumed. This simplified reactor core is placed into a water-filled cylinder of 280 cm in diameter and 700 cm height, representing the reactor vessel. Furthermore, the geometry consists of the following components: the fuel assemblies of highly enriched uranium (36wt% ^{235}U), the control rod assemblies, the neutron reflector, air and water displacement channels and the test fuel element. The model of the reactor core and the test fuel element is depicted in Fig. 4-5.

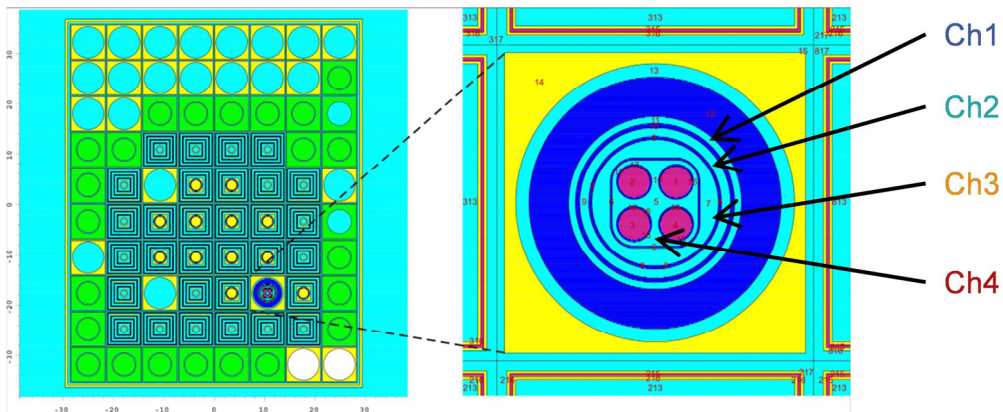


Fig. 4-5 LVR-15 core arrangement (right) and MCNP5 model of the test section (left) [82].

The calculations are performed assuming the control rods being completely removed. Thus, the calculated axial power profiles show a symmetric cosine-shaped distribution. For the analysis of the fuel element fissile power, the active length is divided into 14 segments of 4 cm length each. Two different cases are studied in these simulations. The first one, called Test Run 1, assumes that the coolant temperature is varied in all four channels of the test fuel element (Ch1-4), numbered from 1 to 4 from outside to inside, as illustrated on the right hand side of Fig. 4-5. In Test Run 2, a temperature variation is assumed only in the central channel (Ch4), composed by the four fuel pins and the enclosing quadratic assembly box. The latter case shall simulate a sudden evaporation of the coolant in the innermost channel. The simulation results for different coolant temperatures and densities show that the fuel element power increases with coolant density, as shown in Fig. 4-6.

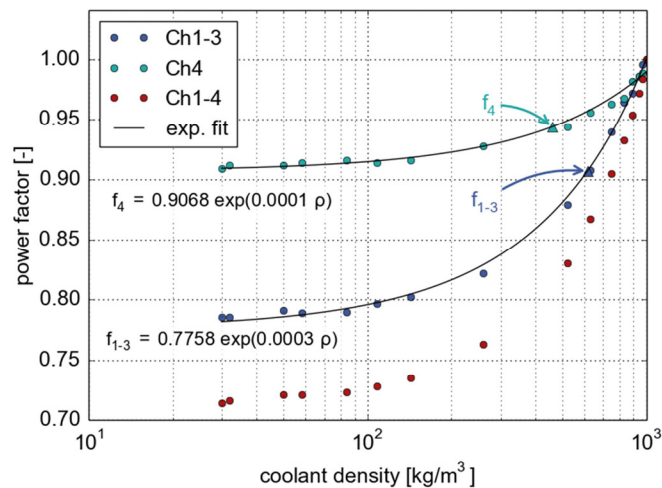


Fig. 4-6 Fuel element power as a function of coolant density.

Moreover, it is found that the coolant temperature inside the pressure tube has very low influence on the effective multiplication factor of k_{eff} . Thus no significant reactivity response of the reactor core is provoked. To implement the density feedback on heating power in the APROS model, the power factor of Test Run 1 (Ch1-4) is split between a factor f_4 arising from density changes in channel 4 only, and a factor f_{1-3} caused by the average density change in channels 1 to 3. The latter factor is derived from the simulation results by dividing f_{1-4} by f_4 :

$$f_{1-3} = \frac{f_{1-4}}{f_4}. \quad (4.1)$$

This new curve (Ch1-3) and the curve for a density change in the inner channel 4 (Ch4) are fitted with exponential functions as shown in Fig. 4-6. From the average coolant density in the channels 1 to 3 and the average density in channel 4, APROS calculates the factors f_4 and f_{1-3} . Multiplying these factors with the nominal power gives the actual fissile fuel element power. For a nominal power of 74.3 kW the desired fuel element power of 63.6 kW for steady-state operation is obtained. The application of the density feedback can be switched on or off in the numerical model.

4.1.2 Decay Heat Curve

As soon as a reactor SCRAM happens, the fuel element power decreases rapidly. After 0.06 seconds delay, in which the control rods are released, they need another second to fall into the reactor core. In this latter period, the power is assumed to decrease linearly with time. Afterwards, a conservative decay heat distribution is applied, which was obtained by Brolly et al. [80], who performed irradiation and cooling calculations for the test fuel using the best estimate code TIBSO [83] and considering several irradiation times. Out of these simulation results, the maximum decay heat percentage is selected for each cooling period. According to Rudstam [84] the one sigma uncertainty for decay heat of 5.5 % was applied together with an additional engineering factor of 1.165, which corresponds to three sigma. The obtained decay heat progression is plotted on a semi-logarithmic scale in Fig. 4-7.

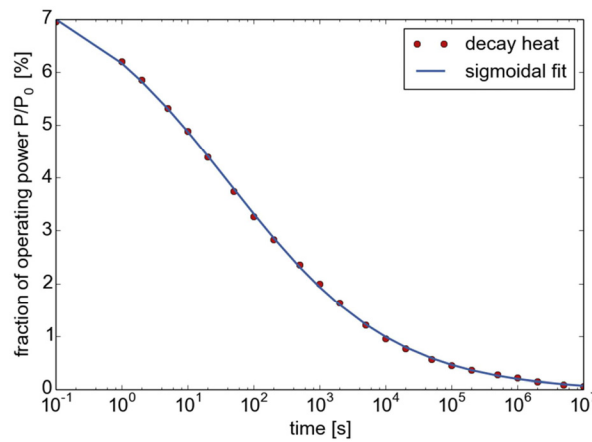


Fig. 4-7 Decay heat as fraction of operating power over time after the reactor was scrammed [83] and corresponding sigmoidal fit as applied in APROS.

The s-shaped curve is fitted with a sigmoidal equation (1) and is valid for $t > 0.1$ s:

$$P(t) = C_2 + \frac{C_1 - C_2}{1 + \left(\frac{t}{t_0}\right)^f}. \quad (4.2)$$

With the coefficients $C_1 = 7.86259$, $C_2 = -0.0403$, $t_0 = 41.97635$, and $f = 0.34749$, the coefficient of determination results in $R^2 = 0.99981$.

4.2 Depressurization System

A controlled depressurization of the primary circuit can be carried out via one of the two depressurization lines and their associated valves ADS1 and ADS2 depending on the triggered emergency system. Furthermore, an additional line can be opened by a spring loaded pressure relief valve (AV1), which automatically regulates excess pressures. Behind these valves, the three lines come together in a single line, ending up submerged in the water storage of the depressurization tank. The end of the depressurization line is designed as a sparger, created by 50 holes of 2 mm diameter arranged in ten rows with a pitch of 10 mm. The vented depressurization tank BN works as the pressure sink of the loop. In this volume bubbles or steam jets shall be condensed without penetrating the water surface. The assumed geometry of the tank has an inner diameter of 1 m and a height of 1.5 m. During design operation, the liquid level inside the tank is 0.8 m. This leaves a gas volume of 0.55 m^3 , capable to take over the coolant injected by pressurizer KO1 and both accumulators in case of a depressurization. A water volume of 0.63 m^3 is large enough to keep the coolant temperature below saturation temperature for any kind of accident. For a tank of 1 m in diameter and a height of 1.5 m this adds up to a liquid level of 0.8 m during normal operation of the loop.

In the numerical model, the porous end of the sparger tube is represented by a node with a corresponding volume. The 50 sparger holes are resembled by a single pipe module, whose flow length of 4 mm is equal to the wall thickness of the depressurization line. For the evaluation of the pressure drop the hydraulic diameter for one hole is used in combination with the total flow area of all holes. A discharge coefficient of 1 is applied for free discharge, according to [68].

A flow through these holes is limited to the critical mass flow when the maximum speed at the narrowest cross section reaches sound velocity. For liquid single-phase and for two-phase flows, the critical flow is calculated according to Moody [56]. In case the two-phase flow is changing to steam flow, a linear interpolation between the Moody model and a single-phase Laval nozzle is applied.

The sparger is connected to a tank module, shown in Fig. 4-8, which is defined by its geometry and the variables pressure, temperature, enthalpy, liquid level, and the mass fraction of non-condensable gas. Initially, the tank is partially filled with water at $30 \text{ }^\circ\text{C}$. The gas volume is modeled with non-condensable gas and the dissolved mass fraction of gas is set to 0. For continuous venting, the top of the tank is connected to a point, which is constantly at ambient pressure. The void fraction in this point as well as the mass fraction of non-condensable gas in the gas phase is set to 1, meaning that only non-condensable gas can enter the system through this point. As non-condensable gas air is selected.

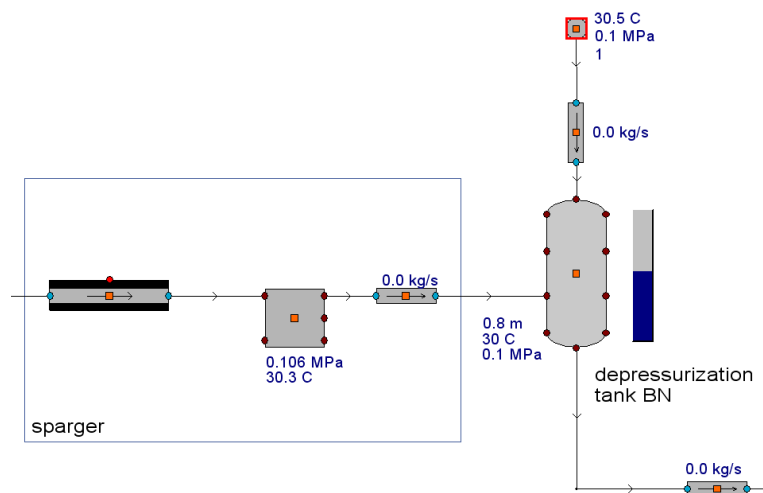


Fig. 4-8 APROS model of the depressurization system with tank BN and sparger.

4.3 Accumulator and Pressurizers

As accumulators and pressurizers, bladder accumulators are chosen which are connected to the loop. These passive devices contain an elastomeric membrane, which is separating the stored water volume from a compressed nitrogen volume. As the APROS code does not support changing volumes, no standard component could be used for modeling. For this reason, the actual pressure in the numerical model is calculated by the amount of coolant that is entering or leaving the pressurizer. Then, a boundary condition module is used to permanently pass over the resulting pressure to a point, which is taken out of the simulation. The APROS model of the accumulators TZ1 and 2 generated for this purpose is depicted in Fig. 4-9.

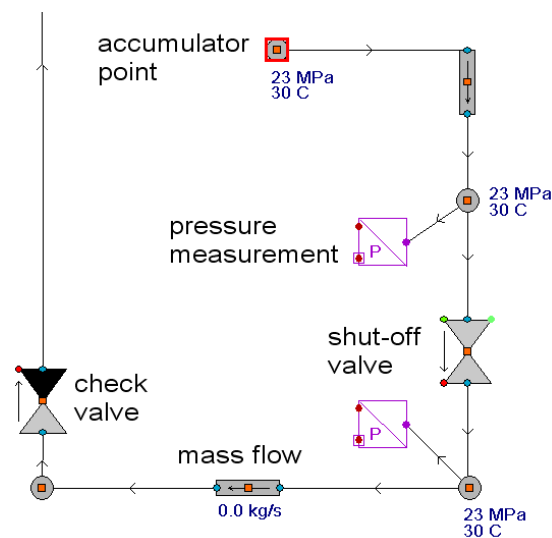


Fig. 4-9 APROS model of the passive bladder accumulators TZ1 and TZ2.

Assuming an adiabatic process and applying the ideal gas correlation, the gas pressure can be calculated as a function of the stored water inventory. The accumulator has a total inner volume of 54 dm³. For an operating pressure of 23 MPa the water inventory results in 30 dm³. Furthermore, a gas volume of 17.25 dm³ corresponds to the maximum allowed pressure of 32 MPa. Thus, the following correlation gives the pressure p [MPa] in dependence of the stored liquid mass m [kg]:

$$p(m) = 1.5981 \cdot 10^{-5}m^4 - 6.7953 \cdot 10^{-4}m^3 + 1.6357 \cdot 10^{-2}m^2 + 0.1167m + 10.2811. \quad (4.3)$$

In order to avert inflows of hot coolant, a check valve is installed in front of the accumulator. In the numerical model, an additional shut-off valve is needed to prevent further outflow of coolant in case the accumulator inventory is depleted.

The pressurizers KO1 (primary circuit) and KO2 (secondary circuit) are modeled in the same way. However, no check valve is needed, as inflows are allowed. Moreover, in correspondency with the system pressure, their design pressure is 25 MPa. Thus, the correlation between gas pressure and water inventory is given by:

$$p(m) = 1.4536 \cdot 10^{-5}m^4 - 5.3771 \cdot 10^{-4}m^3 + 1.381 \cdot 10^{-2}m^2 + 0.1582m + 11.1493. \quad (4.4)$$

In the loop, an air cooler is installed at the inlet of the pressurizers to cool down incoming water. For this reason, the coolant temperature inside the pressurizers in the numerical model is assumed to be constantly 30 °C.

4.4 Double-pipe Heat Exchanger CH1

The cooler CH1, which transfers heat from the high pressure secondary circuit to the cold low pressure tertiary circuit, is illustrated by a cross section depicted in Fig. 2-8. This complex shell and tube assembly cannot be reproduced by standard heat exchanger components of APROS. In order to model the bundle of tubes which is carrying the hot coolant, a pipe with heat structure is applied. In the properties of this pipe, the number of parallel pipes is set to 37 in order to model the complete rod bundle by a single component. The tube wall is composed by three layers. For the two external ones, stainless steel is chosen as material, while the middle one is formed by a gap containing helium. The surrounding hexagonal tube, which is carrying the cold low pressure coolant, is also modeled by a pipe with heat structure. Finally, heat transfer modules are applied to link the outermost heat structure nodes of the tube bundle directly to the thermal hydraulic nodes of the shell side. In axial direction, the heat exchanger is discretized by the help of 20 segments, as illustrated in Fig. 4-10. The tertiary circuit is connected to the cooling system of the research reactor and operated at a pressure of 0.6 MPa. The inlet temperature on the shell side is fixed to 60 °C. Via a bypass, a certain fraction of the secondary coolant can be routed around the cooler in order to yield the desired inlet temperature of the downstream u-tube cooler.

5 Design Operation

The objective of the SCWR-FQT project is to investigate the behavior of the test fuel element under evaporator conditions as expected for the central fuel elements of the HPLWR. Here, the coolant enters the fuel elements at supercritical pressure but subcritical temperature and gets pseudo-evaporated while flowing upwards through the core. In order to emulate the conditions inside the HPLWR core with a coolant mass flux in the range of 1200 to 1500 kg/m²s, a mass flow rate of 0.25 kg/s (1380 kg/m²s) has been chosen for design operation of the test section. By the use of guide tubes and a recuperator, the flow pattern is created such that an effective preheating of the coolant is achieved before it enters the test section, where a maximum coolant temperature of approximately 383 °C is reached. The heat balance over the test fuel element is visualized in Fig. 5-1 by a Sankey diagram for the case of stationary design operation. The unit of the illustrated heat flows is kW, the colors indicate the four flow channels created by the internal structures. The hatching of the paths indicates the three sections cooler (none), recuperator (diagonal), and heated section (crossed). In this diagram the quantity of a heat flow is proportional to the width of an arrow.

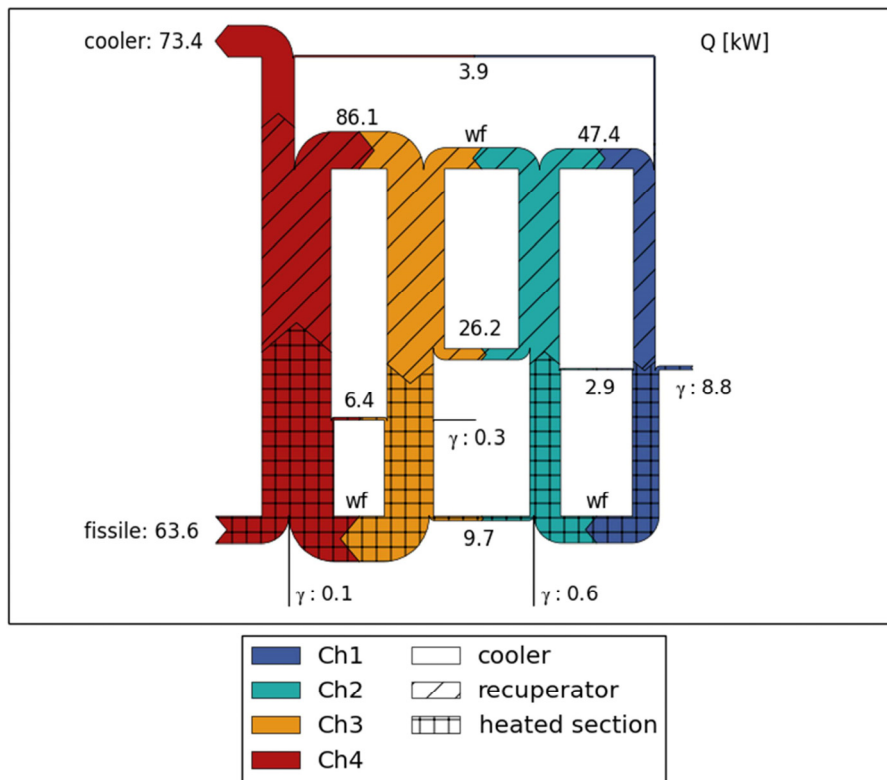


Fig. 5-1 Heat flows inside the test fuel element visualized by a Sankey diagram.

Heat is supplied at various locations of the cycle. The major input of 63.6 kW is released in the test section by the fissile power of the fuel rods, but there are also four minor heat sources created by gamma heat, which is released in the metal structures in the lowest section of the fuel element. In total, the gamma power adds up to 9.8 kW; however, the majority is supplied to channel 1 (Ch1) emitted by the thick-walled pressure tube (8.8 kW). The only heat sink is realized by the u-tube

cooler in the uppermost section which, in stationary operation, removes the inserted heat of 73.4 kW in total via the secondary loop¹⁰. Furthermore, the remaining arrows represent either regenerating heat flows across baffles separating neighboring flow channels, or water flows through redirections connecting two channels. For the first ones, the amount of transferred heat is given; the latter ones are labeled as *wf*. These heat flows are the result of temperature differences between the respective channels. As intended, the small recuperator pipes subsequent to the heated section serve for an effective preheating of the coolant transferring 86.1 kW of heat. The coolant temperature distribution inside the four channels of the test fuel element, corresponding to the above presented heat flows, is shown in the upper half of Fig. 5-2.

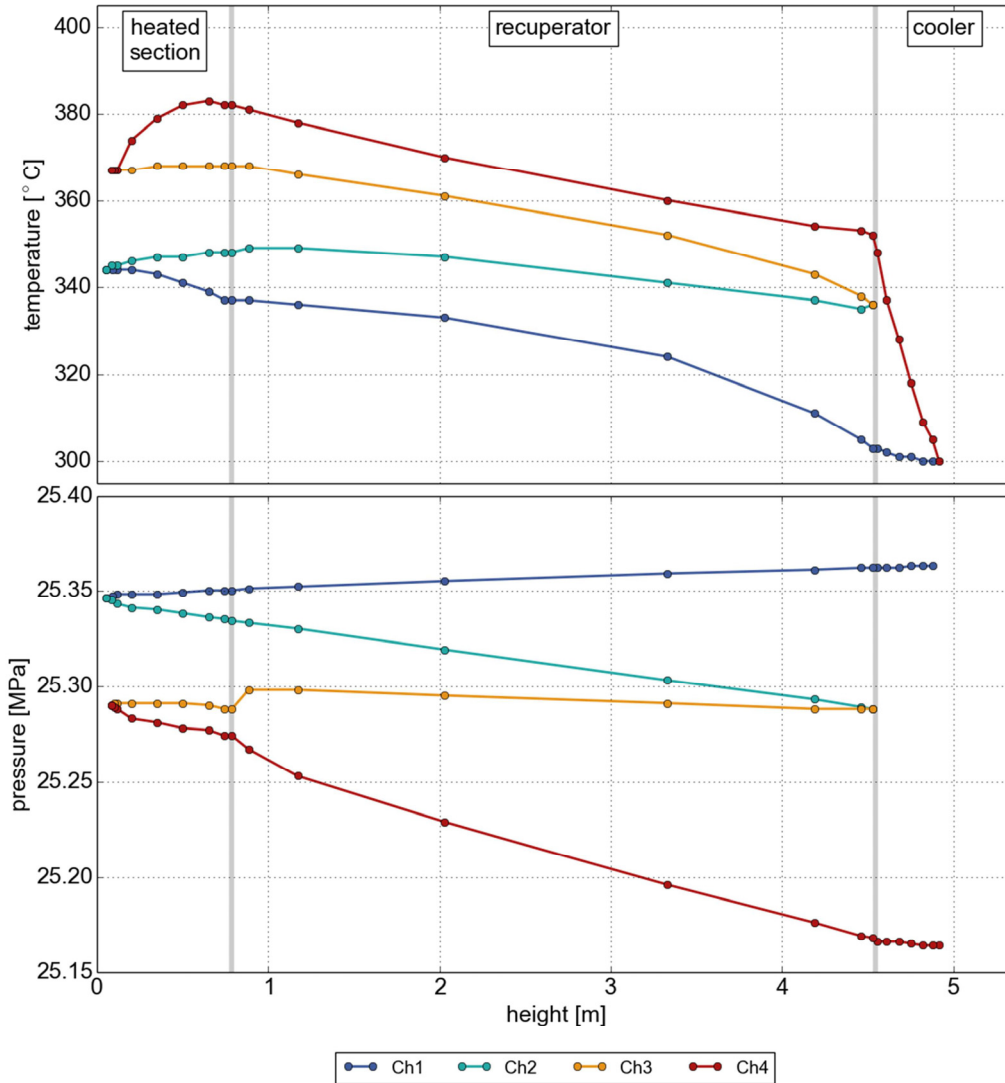


Fig. 5-2 Coolant temperature (top) and pressure (bottom) distribution in the test fuel element at design operation conditions.

¹⁰ The pressure tube is assumed to be adiabatic due to the insulation of the air gap separating it from the reactor pool.

The coolant enters the test fuel element at the top of channel 1 (Ch1) with a temperature of 300 °C. A relatively high heat up is noticeable in the heated section of channel 1, due to the high gamma power generated in the thick-walled pressure tube. Upon passing the fuel rods inside the assembly box (Ch4), the coolant reaches its maximum temperature of 383 °C. From there it passes first through the bundle of 28 recuperator tubes losing 30° in temperature while preheating channel 3, and next through the cooler, which brings it back to 300 °C. The corresponding pressure drop over all four channels, calculated with the correlation of Kirillov et al., cited in [48], is 0.2 MPa, as illustrated in the same way in the lower diagram of Fig. 5-2.

6 Design Optimization for Fast Depressurization Transients

The active channel, i.e. the pressure tube with its internals, is equipped with thin-walled guide tubes to create the intended flow pattern in order to preheat the coolant before reaching the test section. These guide tubes, however, turned out to be a cause for concern in case of fast depressurization transients. Unavoidable pressure differences across the thin tube walls might cause a buckling collapse in case the active depressurization system would be opened or in case of a large break loss-of-coolant accident, which would damage the internal structure as a consequence. Therefore, the active channel was optimized to withstand such transients without buckling, as published in [85].

6.1 Buckling of the Guide Tubes

A first dimensioning of the pressure tube and its internals has been performed by Kremers [86] according to the German KTA (Kerntechnischer Ausschuss) Safety Standard 3201.2 (1996) [87] for Components of the Reactor Coolant Pressure Boundary of Light Water Reactors. This dimensioning is based on design operation parameters, thus load case NB (normal operation) in combination with loading level A (transient loads) as defined in this safety standard, were chosen as design criteria.

In the present analysis, instead, the resistance of the guide tubes shall be evaluated against buckling during off-design conditions. Different from steady-state operation, a fast depressurization of the loop could cause considerably higher pressure differences across the thin-walled pressure tube internals. Buckling collapse of the internals, however, has to be prevented in any case to enable an effective residual heat removal. Applying the KTA standard Annex A 2.2.3.3 [87], the criteria for elastic instability of cylindrical shells under external pressure reads:

$$p_{all} = \frac{E}{f_k} \left\{ \frac{2}{(n^2-1) \cdot \left[1 + \left(\frac{n}{Y}\right)^2\right]^2} \frac{s_{0n}}{d_{out}} + \frac{2}{3(1-\nu^2)} \cdot \left[n^2 - 1 + \frac{2n^2-1-\nu}{1 + \left(\frac{n}{Y}\right)^2} \right] \cdot \left(\frac{s_{0n}}{d_{out}} \right)^3 \right\} \quad (6.1)$$

with a design value Y defined as

$$Y = \frac{\pi d_{out}}{2L}. \quad (6.2)$$

Here, a safety factor $f_k = 3$ against elastic instability has to be applied. According to the guideline, the number of lobes n is set to 2. The geometrical data such as length of the shell L , the outer diameter d_{out} and nominal wall thickness s_{0n} are listed in Tab. 6-1 together with the attained allowable pressure p_{all} for each guide tube. As material for the internals, the austenitic steel 08Ch18N10T has been assumed. The Young's modulus E equals 170 GPa and the Poisson's ratio ν equals 0.3 at a maximum design temperature of 400 °C [88].

Tab. 6-1 Geometrical data and corresponding allowable pressures for the pressure tube internals.

	guide tube 1	guide tube 2	emergency line	recuperator tubes
L [mm]	4822.2	4448.2	4161.7	3692
d_{out} [mm]	36	30	11	3
s_{on} [mm]	1	0.75	0.75	0.2
p_{all} [MPa]	2.67	1.95	39.48	36.90

Thus, the additional safety factor against buckling S_b , i.e. the allowable pressure p_{all} divided by the peak pressure difference across a tube wall Δp , must be greater than 1:

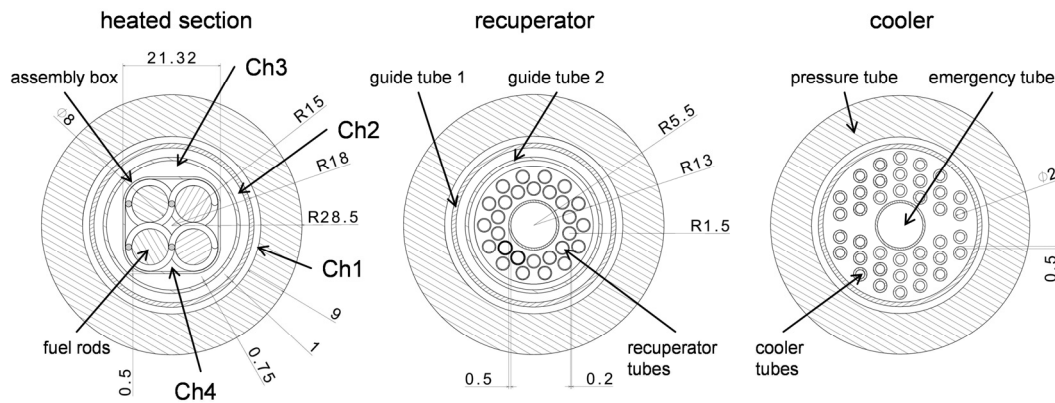
$$S_b = \frac{p_{all}}{\Delta p}. \quad (6.3)$$

As the assembly box is not of cylindrical shape, the above criteria cannot be applied there.

6.2 Pressure Histories during a Loss-of-coolant Accident

Several loss-of-coolant accidents are analyzed with APROS to determine the peak pressure differences across the guide tubes. All simulations start at design conditions. A double-ended break of any line is assumed to happen after two seconds. Two different break locations are considered for each line (L1, L2, and L3): one break position close to the head piece of the fuel element and another one close to the respective pump either HCC or HC2.

The pressures inside the fuel element are evaluated at points of maximum pressure difference across each guide tube. Cross sections, including definitions of discussed guide tubes and flow channels, are depicted in Fig. 6-1.

Fig. 6-1 Cross sections of the active channel¹¹.

The axial measuring locations are given in Tab. 6-2 for each tube. The top of the reactor core grid plate is defined as zero level. For guide tube 1, the differential pressures are evaluated at the top of the cooler and of the recuperator sections. For guide tube 2, the pressures are analyzed at its lower end. The pressure difference across the recuperator tubes is assessed in the middle of the recuperator section. For the assembly box and for the emergency cooling line, the maximum pressure differences occur at the top end of each tube, accordingly.

Tab. 6-2 Locations of pressure readings along the vertical axis of the fuel element.

	guide tube 1 (cooler)	guide tube 1 (recup.)	guide tube 2	recuperator tubes	emergency tube	assembly box
height [m]	4.8775	4.461	0.501	2.031	4.8775	0.501

As an example of such transient analyses, Fig. 6-2 shows the simulation results for a double-ended break of line L3 close to the emergency pump HC2 (Fig. 2-6). The left hand side of Fig. 6-2 illustrates the pressure histories in the flow channels of the fuel element within the first 50 seconds of the accident. It is obvious that the speed of depressurization depends on the flow distance to the break. The sudden pressure drop at after 22 seconds is caused by emptying accumulator TZ1. Along with the decreasing coolant inventory of the accumulators, the differential pressures, shown on the right hand side of Fig. 6-2, decrease steadily until the end of the depressurization period. The differential pressure across a tube wall results from the pressure at the outside channel minus the internal pressure of the particular tube. Due to the coolant injection of accumulator TZ2 over line L3, the pressure difference across the emergency tube wall (yellow line) is negative indicating that the pressure on the inside of the tube is greater than on the outside. Negative values are not relevant for buckling, but they could lead to a plastic tube deformation in case the equivalent stress exceeds the yield strength of the material due to the internal overpressure. In such cases, the deformed tube may re-

¹¹ Design by CVR, with permission from CVR from 2014.

duce the cross section of the outside flow channel as well. However, for a temperature of 400 °C, the yield strength of the assumed material is $R_{p0.2} = 162$ MPa.

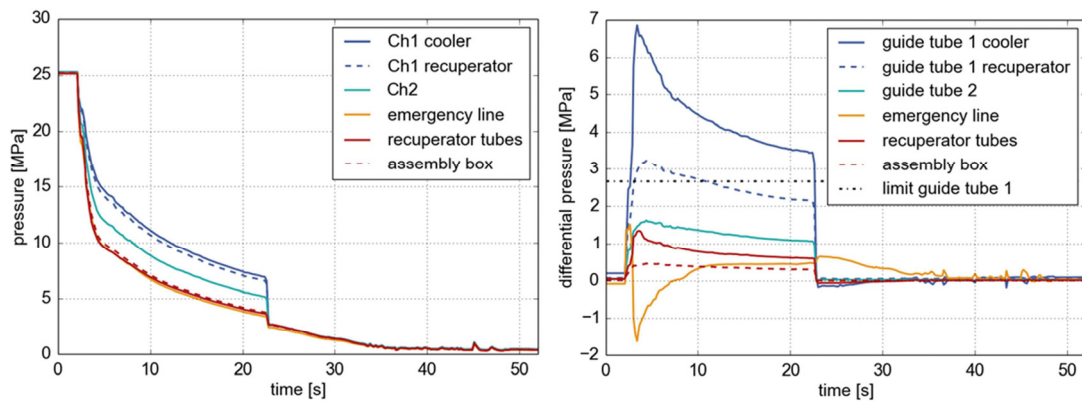


Fig. 6-2 Pressure history in the channels of the fuel element (left) and pressure differences across the according guide tube walls (right) for a break in the emergency line close to pump HC2.

As shown in Fig. 6-2, the pressure differences across guide tube 1 differ significantly between the cooler (solid blue line) and the recuperator (dashed blue line) section. In the recuperator section, guide tube 1 separates channels 1 and 2, and a maximum differential pressure of $\Delta p = 3.24$ MPa is predicted. Whereas in the cooler section, the same tube separates the incoming coolant in Ch1 from the outgoing coolant in Ch4, thus facing the overall pressure loss of the fuel element. This leads to a considerably higher Δp of 6.86 MPa. According to Eq.(6.3), the additional safety factor against buckling would be less than 1 for both sections ($S_b = 0.82$ or 0.39, resp.). This causes a need for design refinement. The other tubes, i.e. guide tube 2, the recuperator tubes and the emergency cooling line experience smaller pressure differences so that their wall thickness is sufficient to avoid failure.

As a first measure, the wall thickness of guide tube 1 in the cooler section is increased from 1 to 1.5 mm as there remains enough spare space in this part of the fuel element. For the strengthened guide tube 1, the allowable pressure increases to $p_{all} = 9.0$ MPa. But, in the other sections of the fuel element, there is no space for thicker walls. For this reason, other design modifications needed to be considered.

6.3 Optimization of the Outlet Cross Sections in the Head Piece of the Fuel Element

In order to reduce the flow velocity of the coolant and thus the pressure differences in case of a loss-of-coolant accident, the cross sections of the connecting nozzles in the head piece of the fuel element are adjusted. A parametric study is performed, analyzing bore diameters in the range of 5 to 14 mm.

Fig. 5.6.3 shows the decrease of differential pressures for a break of the emergency cooling line (L3), close to pump HC2, for reduced outlet diameters.

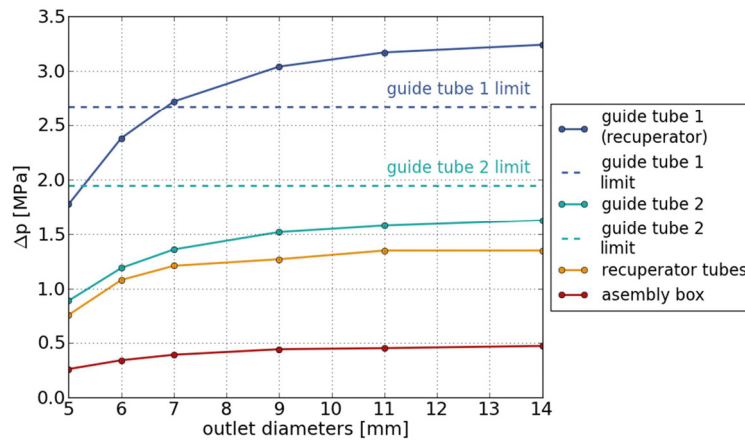


Fig. 6-3 Differential pressures in case of a rupture of the emergency cooling line L3 close to pump HC2 for outlet diameters in the range from 5 to 14 mm.

In general, guide tubes 1 and 2 are most sensitive for buckling due to their high ratio of outer diameter to wall thickness. The maximum pressure differences across guide tube 1 for all break locations are illustrated in Fig. 6-4. The allowable differential pressure is exceeded only in case of a break of the emergency line. The limits for guide tube 2 are always met.

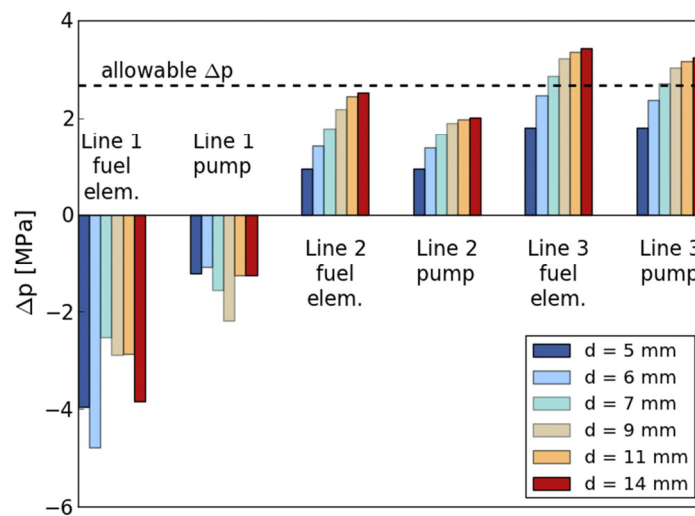


Fig. 6-4 Maximum pressure differences across guide tube 1 at the top of the recuperator section for different break locations and different outlet diameters.

Analyzing the simulation results, it turns out that the pressure differences stay within the allowable limits for any break position if the outlet diameters are chosen to be less or equal to 6 mm. In the cooler section, the pressure difference across guide tube 1 decreases similarly. Here, a maximum Δp of 3.645 MPa is predicted which is far below the limit of 9.0 MPa for the enforced tube. Among all simulations, the maximum internal overpressure was detected across guide tube 1 with $\Delta p = 4.789$ MPa. This pressure causes an equivalent stress in the tube wall of 81.4 MPa. Compared to a yield strength of $R_{p0.2} = 162$ MPa, there is still a safety margin of two against plastic deformation. For this reason, deformations due to internal overpressures are not to be expected for any guide tube.

Pressure histories for a break of line L3 close to emergency pump HC2 are shown exemplarily in Fig. 6-5, assuming an inner diameter of 5 mm for all nozzles of the head piece. The pressure differences between the flow channels of the test fuel element decreased as intended. Now, the pressure differences across the guide tubes stay within the determined limits, as depicted on the right hand side of Fig. 6-5. In addition, buckling of the assembly box is very unlikely as the maximum pressure difference across its wall is only 0.26 MPa.

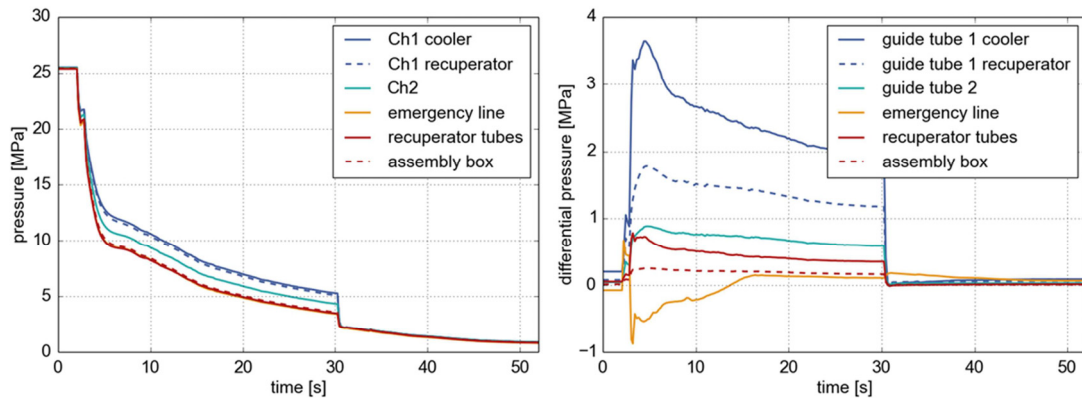


Fig. 6-5 Pressure history in the flow channels of the fuel element (left) and differential pressures across the guide tubes (right) for a break of line L3 close to emergency pump HC2, assuming outlet diameters of 5 mm.

As another benefit of this optimization, the depressurization period and thus the injection time of accumulator TZ1 is expanded from 22 to 30 seconds. The resulting emergency coolant mass flow rates are depicted on the left hand side of Fig. 6-6.

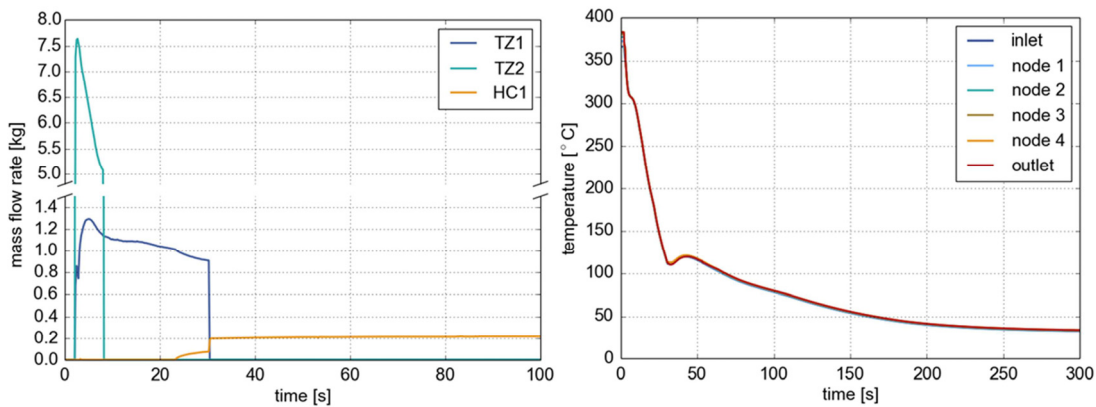


Fig. 6-6 Emergency coolant mass flows provided by the accumulators and by the emergency pump HC1 (left) and resulting coolant temperatures in the test section (right) for a rupture of the emergency cooling line close to pump HC2.

Both emergency accumulators inject their inventory within the first 30 seconds of the accident. During this period, the mass flow through the test section is still about 3 to 4 times higher than during normal operation. As soon as the system pressure falls below 12 MPa, emergency pump HC1 provides long-term residual heat removal. The injected mass flow rate reaches a constant value of

6.3 Optimization of the Outlet Cross Sections in the Head Piece of the Fuel Element

0.21 kg/s as soon as both accumulators got empty. The right hand side of Fig. 6-6 shows the coolant temperature progression inside the assembly box. Within the injection period of the pressure accumulators, the coolant temperatures fall below 120 °C. Subsequently, the stored heat of the thick-walled pressure tube leads to a slight, short-time temperature increase due to the reduced coolant mass flow provided by emergency pump HC1. After 300 seconds the coolant temperature is constantly kept below 40 °C.

During normal operation, the reduced bore diameter leads to an additional pressure loss of 0.5 MPa. This adds up to a total pressure loss across the test fuel element of 0.85 MPa, as listed in Tab. 6-3.

Tab. 6-3 Pressure loss across the test fuel element at stationary operation for outlet diameters of 14, 6, and 5 mm.

Outlet diameters [mm]	Δp fuel element [MPa]
14	0.35
6	0.54
5	0.85

Discussion

Transient LOCA analyses have been performed with the system code APROS, showing that a fast depressurization of the SCWR-FQT loop causes high pressure differences across the thin-walled guide tubes which are installed inside the test fuel element. A reduction of the bore diameter of the connecting nozzles in the head piece of the fuel element is able to attenuate the pressure drop inside the fuel element. This measure results in considerably declined differential pressures across the guide tubes. Thus, potential buckling which could reduce the flow cross sections and impede the injection of emergency coolant is prevented. With respect to the provided pressure head of the recirculation pump, outlet diameters of 6 mm are recommended for all bore holes in the head piece. This modification has been applied for all APROS simulations presented hereinafter. Moreover, it was found that guide tube 1 in the cooler section of the fuel element faces the highest pressure differences. For this purpose, the wall thickness in this section has been additionally increased from 1 to 1.5 mm in order to bear possible loads. For the optimized design, failure due to plastic deformation caused by internal overpressures is not to be expected as the arising equivalent stresses are low compared to the yield strength of the utilized austenitic steel. Another benefit of the reduced diameters in the head piece is an extended injection period of the pressure accumulators and a longer grace period for the active emergency pumps to run up for long-term residual heat removal.

7 Safety Analyses of Design Basis Accidents

In this chapter safety analyses are presented, performed with APROS for anticipated design basis accidents, which are all based on single component failures. The considered accident scenarios are listed in Tab. 7-1:

Tab. 7-1 Design basis accidents analyzed with APROS.

- Trip of recirculation pump HCC (Chapter 7.1)
- Loss of heat sink (failure of pump CS) (Chapter 7.2)
- Loss of electric power supply with passive long-term residual heat removal (Chapter 7.3)
- Blockage of the coolant flow path:
 - in return line L2 (Chapter 7.4.1)
 - in feed line L1 (Chapter 7.4.2)
- Coolant shortcut inside the test fuel element:
 - Between emergency line and channel 4 (Chapter 7.5.1)
 - Between channel 1 and channel 4 (Chapter 7.5.2)
- Loss-of-coolant accidents:
 - Large break of the emergency cooling line L3 (Chapter 7.6.1)
 - Large break of the return line L2 (Chapter 7.6.2)
 - Large break of the feed line L1 (Chapter 7.6.3)

The numerical model developed with APROS covers all of the safety-relevant components of the SCWR-FQT loop as illustrated by the flow scheme in Fig. 2-6. Furthermore, the actions of the emergency systems and their triggers are implemented as described in Tab. 2-2. Each of the presented accident sequences is initiated after two seconds of design operation.

7.1 Trip of the Recirculation Pump

A trip of the primary pump HCC is assumed to occur at $t = 2$ s. The pump speed is reducing to zero within a coast down time of 2 s. The coolant mass flow of the primary system is measured with an orifice at the pump outlet. As soon as the coolant mass flow becomes less than 0.15 kg/s, reactor scram is released, and the reactor is shut down within 1 s. Valve ADS2 opens 1 second after the scram signal has been given, activating the FLCI system. While the power is quickly reducing to the residual heat, the coolant mass flow continues to decrease to around 80 g/s. 1.5 s after the scram signal, the automatic depressurization system ADS2 is sufficiently open, causing the water inventory of accumulator TZ1 to be injected into coolant line L1.

The histories of power, mass flow, pressure, and coolant temperature at the inlet of the test section within the first seconds are shown in Fig. 7-1. After opening the automatic depressurization valve, the coolant mass flow gets increased to more than 0.5 kg/s, which cools down the fuel rods effectively. Fig. 7-2 shows the history of the cladding temperature within the first 5 s of the accident. The cladding temperature is calculated according to the quasi-steady-state approach developed by Schulenberg et al. [63], which is outlined in Chapter 3.6.3b). As visible, a boiling crisis at the fuel rods will be avoided. As soon as the pressure passes the critical pressure, the fuel rods are wetted and thus well cooled.

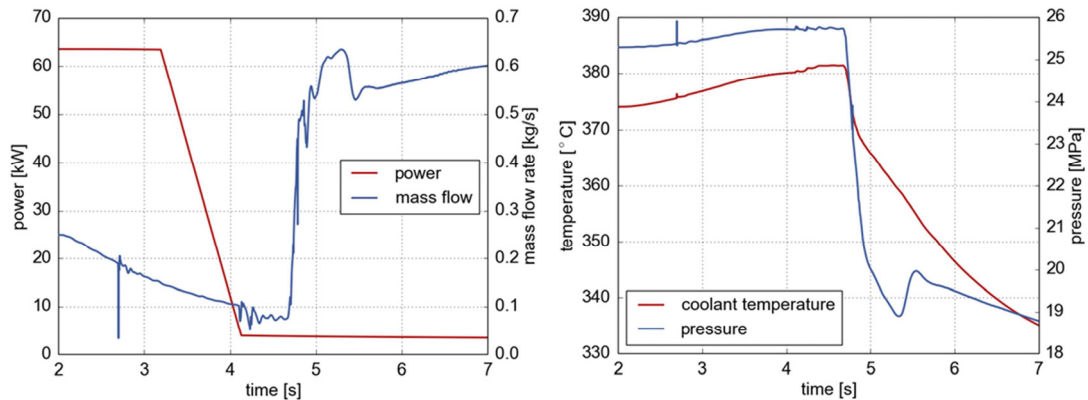


Fig. 7-1 Power of the fuel rods, coolant mass flow rate, temperature and pressure at the inlet of the test section after a trip of the primary pump.

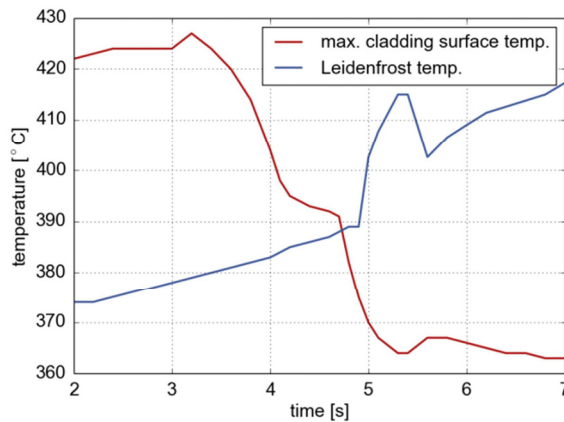


Fig. 7-2 Maximum cladding surface temperature after a trip of the primary pump HCC.

Fig. 7-3 shows pressure progression and coolant temperatures occurring inside the assembly box during the first minutes. The loop gets depressurized via the ADS2 valve within 55 seconds. During this period, cooling of the fuel rods is provided passively by the injection of accumulator TZ1, which reduces the coolant temperatures at the fuel rods below 100 °C.

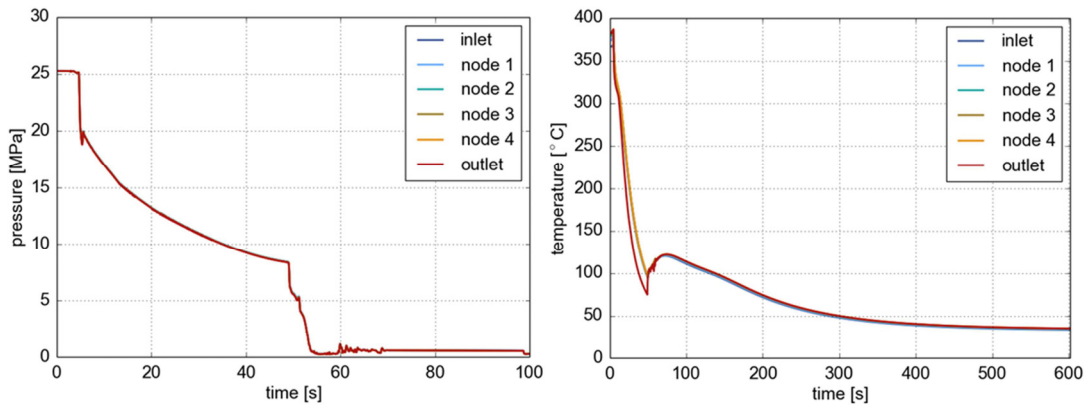


Fig. 7-3 Pressure (left) and temperature progression (right) inside the assembly box for a trip of pump HCC.

As soon as the pressure level at emergency pump HC1 reaches 12 MPa, the active coolant injection into line L1 via the FLCI system starts, ensuring the removal of residual heat. The reduced mass flow rate leads to a small temperature increase up to a maximum of 125 °C before the temperatures steadily decrease to 30 °C. Fig. 7-4 shows the emergency coolant injection provided by the accumulators followed by emergency pump HC1 in the transition phase from passive to active residual heat removal. The resulting distribution of coolant mass flows inside the test fuel element is illustrated in Fig. 7-5.

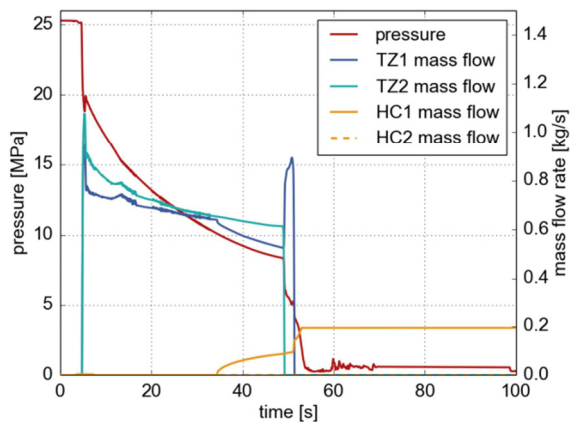


Fig. 7-4 Assembly box pressure and emergency coolant mass flow rate provided by the accumulators and pump HC1.

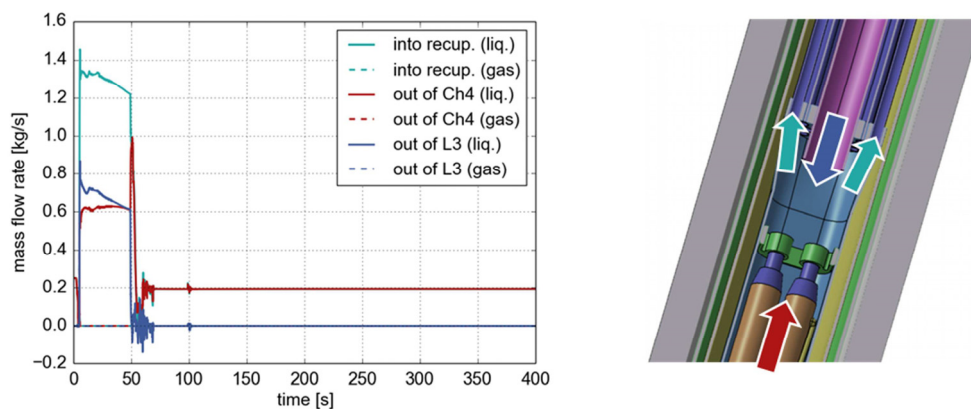


Fig. 7-5 Coolant mass flow rate distribution inside the test fuel element with schematic illustration of flow paths in the transition piece between assembly box and recuperator section¹². Red – coolant flowing upwards through the assembly box, blue – coolant ejected from emergency line L3, cyan – coolant entering the recuperator. The orientations of the arrows indicate positive flow directions.

Discussion

Opening of the automatic depressurization system activates the passive accumulator TZ1 to inject coolant in case of any loss of flow in the test section. Thus the emergency cooling system, in this case pump HC1, has around 50 s time to start up and to take over the cooling task. The delay of ~1 s between scram and depressurization avoids a boiling crisis right after passing the critical pressure. Neither the second nor the third barrier will be damaged during this accident.

7.2 Loss of Heat Sink

This simulation assumes a trip of the secondary circuit recirculation pump CS, which means a loss of heat sink. In this case, the reactor is scrammed and the feed line injection system (FLCI) is activated by the loss of flow signal of the cooler circuit. As a consequence, the loop gets depressurized by opening valve ADS2 one second after the reactor shutdown has been initiated and pump HCC stops. Accumulator TZ1 automatically injects coolant for the first period until emergency pump HC1 takes over for active residual heat removal. During this time, the residual heat released by the fuel rods is dumped in the depressurization tank BN. The IGFS system is manually activated around 140 seconds after the pump trip and the insulation gap surrounding the pressure tube gets flooded. Here, the aim is to turn the encapsulation into a heat sink and by doing so to keep the coolant temperature in the primary circuit below the point of saturation. The 50 l water inventory of tank HV is depleted 1000 seconds later and the flow inside the gap comes to a halt. From now on, the residual heat gets transferred to the reactor pool by conduction through the water filled gap. The left hand side of Fig. 7-6 shows the progression of the coolant temperatures inside the depressurization tank BN and inside the emergency reservoir HN1 during the first ten hours of the accident sequence, as well as the periodic mass flow through the connecting pump HC3.

¹² Design by CVR, with permission from CVR from 2014.

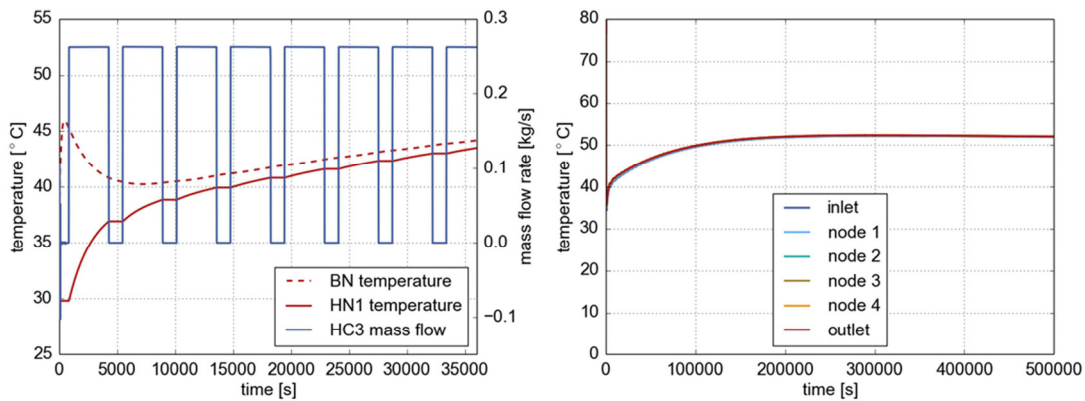


Fig. 7-6 Water temperatures inside depressurization tank BN and inside emergency reservoir HN1 as well as flow rate through pump HC3 (left). Coolant temperatures along the fuel rods over the total simulation period of 500000 seconds (right).

Within the first 500 seconds, the heat which had been stored in the coolant and in the piping of the primary loop, which is now released into tank BN, raises the water temperature from 30 to 46 °C. In the following, the temperature decreases again as the coolant coming from emergency reservoir HN1 gets only slightly heated up due to the substantially decreased residual power of the fuel pins. By recirculating and reusing the coolant, its temperature slowly increases again, until it reaches 50 °C after 104000 seconds (~29 hours), which is the assumed temperature of the reactor pool. After 5000000 seconds, the system is near steady-state conditions with a maximum coolant temperature of 52 °C at the outlet of the test section, which can be seen on the right hand side of Fig. 7-6. This means that the forced convection in combination with the heat bridge to the reactor pool, thanks to the flooded insulation gap, manages to cool the fuel rods efficiently. Thus, the reactor pool serves as a redundant heat sink.

7.3 Loss of Electric Power Supply with Passive Residual Heat Removal

In this chapter a loss of electric power supply is assumed, as discussed in [67]. In this case, a signal loss of power would be given, being followed by the reactor scram and, with a delay of 1 s, depressurization and activation of the FLCI system. In this case, diesel generators and batteries provide power for the active emergency coolant injection but not for the main cooling pumps HCC and CS. Therefore, a loss of off-site power will imply a loss of heat sink. The accident analysis, following afterwards, is identical with the case studied in Chapter 7.2. In contrary to the chapter before, a simplified strategy for long-term passive residual heat removal has been elaborated, which enables to cool without any active emergency system. A supplementary passive system, which however, is not considered to be safety-relevant, is able to provide enough heat removal to cool the test section after a certain period of time. This strategy again implies the filling of the insulation gap with water of 30 °C, stored in the 50 l tank HV. Moreover, free convection inside the primary loop can be used as a driving force to maintain the coolant circulation through the test section, provided that the secondary system can be cooled again by additional cold water supply (e.g. tap water). Thus, the decay heat of the fuel pins can be transferred to the cooler, which is located above the active section. The cooling circuit may be operated at low pressure in this case. The applicability of this procedure is demonstrated by the following transient analyses.

7.3.1 Passive Midterm Residual Heat Removal

Simulation results are presented using this passive heat removal six hours after shutdown of the reactor. The cooling circuit, however, is still assumed to be operating in depressurized state with a mass flow rate of only 0.1 kg/s and 30 °C. At $t = 6$ h, the total residual heat is still 565 W. Once, the forced convection in the primary loop stops, the coolant temperatures in the test section rapidly increase, almost up to the point of saturation, as shown on the left hand side of Fig. 7-7. Hereinafter, hot coolant is rising from the test section to the cooler, driving a natural convection loop of only 3 g/s, which sufficiently cools the fuel rods and prevents damage of the claddings. Over the simulated period of 60000 s (16.7 h), the maximum coolant temperature decreases from 104 °C to 94 °C. The slight coolant temperature increase in the interim is caused by a loss of flow in the insulation gap since tank HV got empty. The right hand side of Fig. 7-7 depicts the radial temperature distribution across the test fuel element at the end of the simulation time (~1 day). Over the complete simulation period, the cladding temperatures are close to the coolant temperatures inside the assembly box and boiling is excluded. The temperature of the pressure tube never exceeds 60 °C, which is far below the material limit of 400 °C.

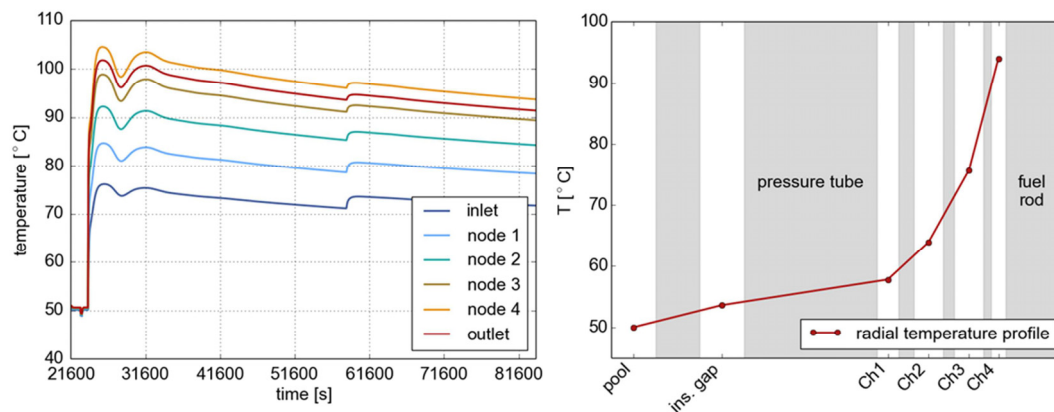


Fig. 7-7 Coolant temperatures along the fuel rods for passive midterm heat removal starting after six hours (left) and radial temperature distribution across the fuel element walls after ~1 day (right).

The secondary cooling circuit may be switched off finally twelve days after the reactor was shut down. From then on, the residual heat can completely be removed through the flooded gap to the reactor pool, as approved by CFD calculations presented in [67].

Discussion

For the event of a loss of electric power, the SCWR-FQT loop is equipped with an emergency power supply system, consisting of batteries and a diesel generator. This system is capable to supply the safety systems with electricity for a defined period of time. The reactor is scrammed and the system is depressurized, which activates a short term coolant injection from the passive accumulators and long-term residual heat removal by the active FLCI system. In order to achieve independence of power supply, however, a strategy for passive long-term decay heat removal has been elaborated. Within six hours after scram, the active coolant injection system is still needed to remove the residual heat. After six hours, the residual heat can be removed by natural convection in the closed primary loop. In this case, the depressurization system and both safety injection systems must be closed but

the cooler must still continue to run, while the cooling loop may be depressurized. For long-term heat removal, the insulation gap flooding system allows increasing the heat transfer across the pressure tube by flooding the air gap between fuel element and reactor pool. Additional CFD analyses show that after twelve days, at the latest, the heat conduction across the flooded gap suffices for the cooling of the fuel rods, as described in [67]. Due to these simulation results, the minimum period for emergency power supply can be determined in order to counteract against overheating of the fuel rods in the event of a long-lasting loss of power.

7.4 Blockage of the Coolant Flow Path

This chapter examines pipe blockages, which are leading to a hampered coolant supply of the test section, assuming different locations and reduction rates of the narrowed cross section. The blockage is assumed to occur in the bridge between reactor and experimental hall, Fig. 2-5, either in the feed line L1 or in the return line L2. The impact of such a reduction of flow area is simulated in APROS with a 5 cm long pipe segment in the duct between experimental hall and the reactor, whose inner diameter is suddenly reduced to a certain value. Such a blockage could, for example, be caused by clogging with foreign matter, by crud deposition or by pipe bending.

7.4.1 Blockage of the Return Line L2

In case of a partially blocked line L2, the mass flow rate through the loop gets reduced, which leads to increased coolant temperatures at the outlet of the test section. As long as the residual flow area is still larger than an equivalent pipe diameter of 3 mm, the temperature rise will be compensated by an automatically raised flow rate in the cooler circuit, maintaining the outlet temperature of the active channel still at 300°C. Scram is not released in such case. A blockage with a flow area equivalent to a diameter of 3 mm results in a primary loop mass flow rate of 0.22 kg/s and a maximum temperature of 385 °C at the outlet of the test section. A warning is given at a flow rate of 0.2 kg/s, according to Tab. 2-2. If the flow area is reduced to an equivalent diameter of 2 mm, the mass flow falls below 0.15 kg/s, which immediately causes the shutdown of the reactor and activates emergency system FLCI. However, due to the considerably blocked connection to the ADS2 valve, the depressurization time of the loop takes up to 250 s until the accumulators are empty, as shown in Fig. 7-8.

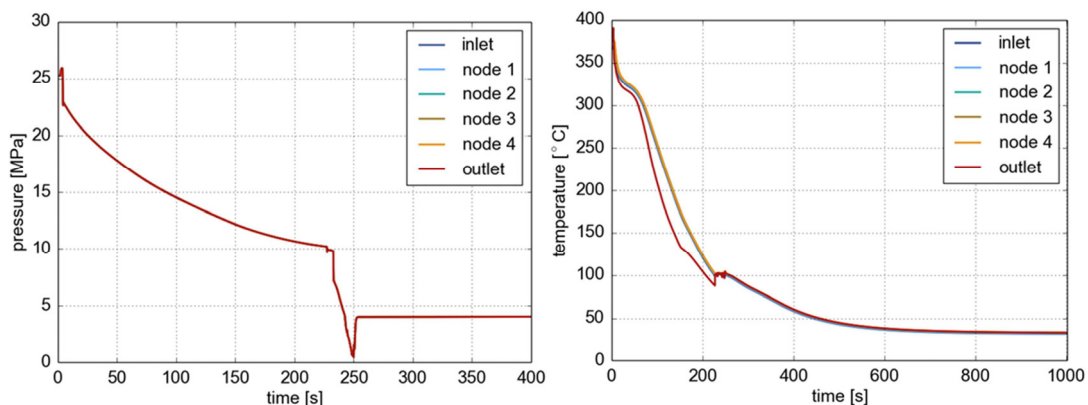


Fig. 7-8 Test section pressure (left) and coolant temperatures (right) for a flow area reduction in the return line equivalent to a pipe diameter of 2 mm.

After depressurization, the high pressure losses in the return line keep the pressure inside the fuel element up at ~ 4 MPa. The coolant temperatures drop slowly as well, which is caused by the impaired emergency coolant injection, illustrated in Fig. 7-9. The accumulators TZ1 and TZ2 can only provide a mass flow of 0.1 to 0.2 kg/s through the test section.

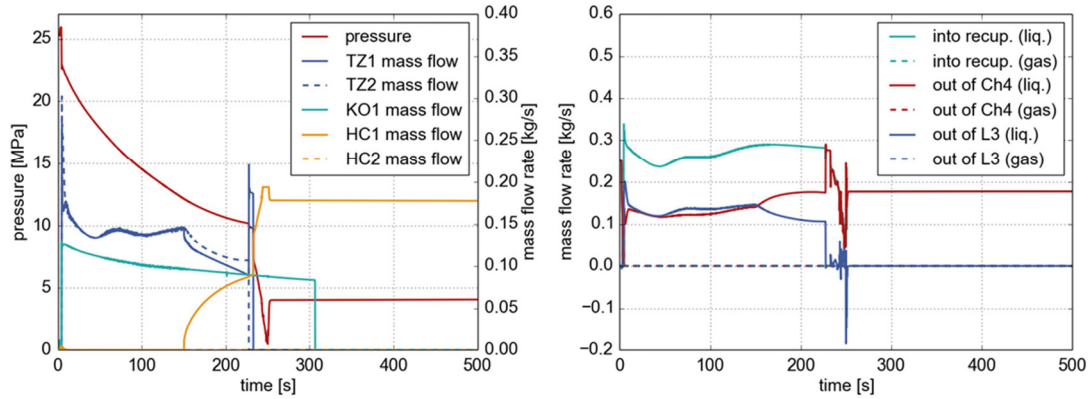


Fig. 7-9 Emergency cooling injection (left) and coolant mass flow rates inside the test fuel element (right) for the first 500 s after line L2 was partially blocked to 2 mm diameter.

In a further analysis, a full blockage of line L2 is assumed. The resulting loss of flow immediately activates scram and opens the ADS2 valve with 1 s delay. Thus, the feed line coolant injection system FLCI is activated at $t = 3.9$ s. However, the completely blocked return line L2 does not allow the coolant provided by pump HC1 to enter the test section. Instead, the stagnant water in the test section rapidly heats up until the high temperature signal, measured at the top of the test section (node 4), is released at $t = 34$ s, as shown in Fig. 7-10. Now the ELCI system is activated according to Tab. 2.1, the depressurization system ADS1 is opened and valve ADS2 is closed instead, the system gets depressurized and both accumulators start to inject. Once a pressure of 12 MPa has been reached, emergency pump HC2 starts to remove the residual heat, injecting over the emergency tube and not requiring line L2.

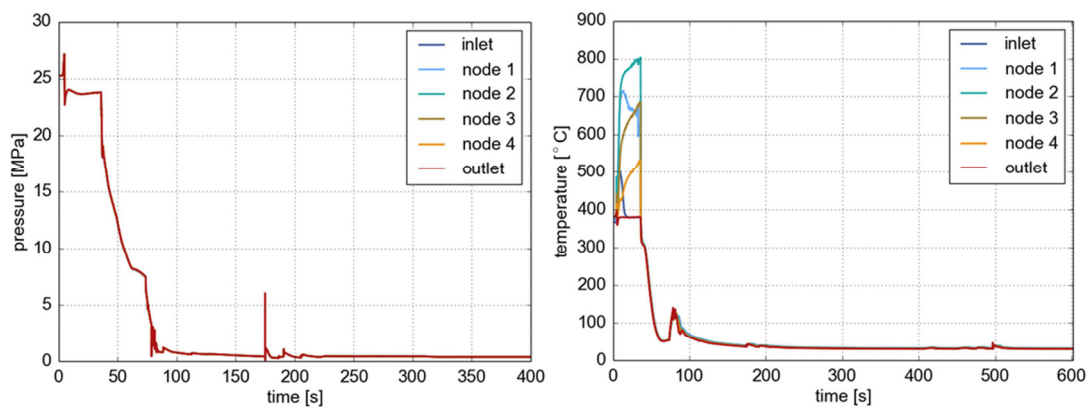


Fig. 7-10 Pressure (left) and coolant temperatures (right) in the test section in case of a full blockage of line L2.

The high coolant temperature of up to 800 °C in the test section means that a damage of the fuel cladding cannot be excluded anymore in these cases, but the third barrier, the primary loop, can be assumed to stay intact in such cases.

7.4.2 Blockage of the Feed Line L1

Similar as in the cases above, a flow area reduction to 3 mm equivalent diameter or more does not decrease the flow rate to less than 0.2 kg/s. The system will just continue to run, even without a warning. Again, a reduction to a diameter of 2 mm will be needed to release a low mass flow signal which scrams the reactor and activates the feed line cooling system FLCI, comparable to the trip of pump HCC. The delayed opening of valve ADS2 starts depressurizing the loop as soon as the power level is reduced such that there is no risk of running into a boiling crisis. In this case, the assumed blockage in the feed line L1 does not affect the depressurization over ADS2 and the pressure drops rapidly to the saturation pressure of 16 MPa. After 39 seconds, accumulator TZ2 is drained, but, as shown in Fig. 7-12, the coolant supply over the feed line L1 is strongly reduced. Thus, as depicted in Fig. 7-12 (left), accumulator TZ1 injects over a period of 110 seconds with an average flow rate of only 0.3 kg/s leading to slowly falling coolant temperatures, as illustrated on the right of Fig. 7-11.

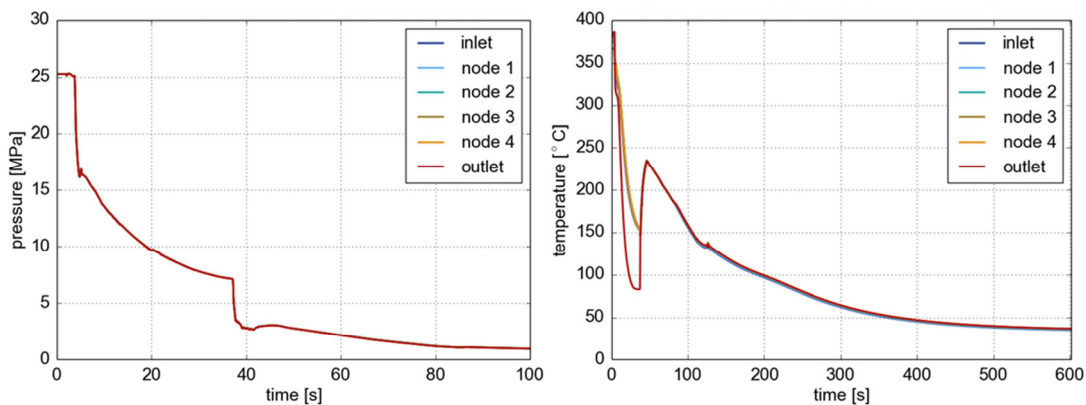


Fig. 7-11 Pressure (left) and coolant temperatures (right) inside the test section after a blockage in the feed line L1, leaving a gap with an equivalent diameter of 2 mm.

In case of a 100 % blockage of the feed line L1, neither accumulator TZ1 nor pump HC1 would be able to inject any coolant into the fuel element. The low mass flow signal would first activate the FLCI system according to Tab. 2-2, causing reactor scram and opening valve ADS2. The pressure would be reduced, but the flow through the test section would continue to be stagnant. After a certain time of lost flow, the high temperature signal would activate the ELCI system, opening valve ADS1 and closing valve ADS2 instead. The system is now further depressurized through pump HCC and through the check valve CV1, since line L1 is fully blocked. Now a cold coolant jet of the emergency cooling line is injected downwards into the central sub-channel of the test section, and hot coolant or steam is released upwards through the outer sub-channels towards the recuperator tubes, from where it leaves the fuel element through line L2. The one-dimensional APROS model cannot predict this counter current flow situation properly. However, we have to assume again that the fuel claddings will be overheated in case of such a full blockage, but the third barrier, i.e. the primary system, can still be assumed to stay intact during such an accident.

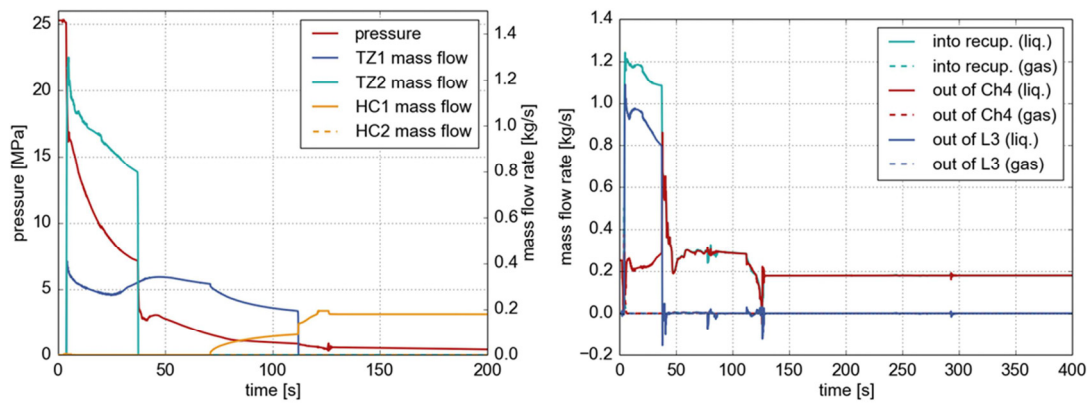


Fig. 7-12 Pressure and emergency coolant mass flow rate provided by the accumulators and pump HC1 (left) with the resulting mass flow distribution inside the test fuel element (right) after a partial blockage in line L1.

Discussion

If the blockage is assumed to increase continuously, the coolant mass flow will be reduced and the safety system will shut down the reactor, depressurize the system and activate the safety injection system FLCI at a mass flow of 0.15 kg/s, such that a damage of fuel cladding can be excluded. A sudden, full blockage of the feed line L1 or of the return line L2 will shut down the reactor and depressurize the system, but the test section will not be cooled properly until the high temperature signal is activating the ELCI system. Temporary overheating of the fuel rods, exceeding the criterion of 816 °C cladding temperature, cannot be excluded before the ELCI system got activated. Radioactive material will then be contained by the third barrier only, which can be assumed to stay intact.

7.5 Coolant Shortcut inside the Test Fuel Element

After analyzing the consequences of pipe blockages, the focus is now on coolant shortcuts inside the fuel element causing a reduced flow rate through the test section. Such shortcuts could e.g. happen in case of fatigue cracks in the thin-walled internals of the pressure tube. Two exemplary crack positions have been assessed here to illustrate potential consequences of such an incident. To model a shortcut two points at the same geodetic height belonging to neighboring flow channels get linked by opening an additional flow path. The flow area of the pipe, which is used for this purpose and whose length corresponds to the thickness of the respective wall, can be varied by the user.

7.5.1 Coolant Shortcut between the Emergency Line and Channel 4

Here, a crack of the emergency line is assumed to occur inside the fuel element at the upper end of the recuperator section, as illustrated in Fig. 7-13. This creates a coolant shortcut between the emergency line and the surrounding channel 4, where coolant coming from the recuperator tubes flows towards the fuel element outlet.

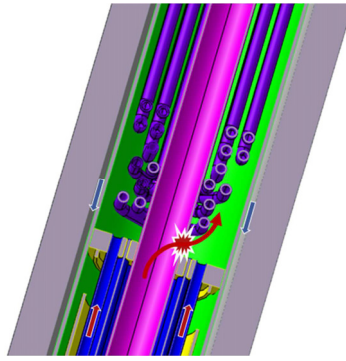


Fig. 7-13 Schematic illustration of a crack in the emergency line between cooler and recuperator section¹³.

This case does not cause any accidental situation and a scram signal does not need to be activated. In fact, coolant coming from the assembly box partially uses the emergency line to bypass the recuperator due to the lower pressure drop here. This even leads to reduced coolant temperatures inside the test section, on the one hand, as the preheating of the coolant is impaired and, on the other hand, the reduced pressure drop allows pump HCC to provide an increased mass flow rate.

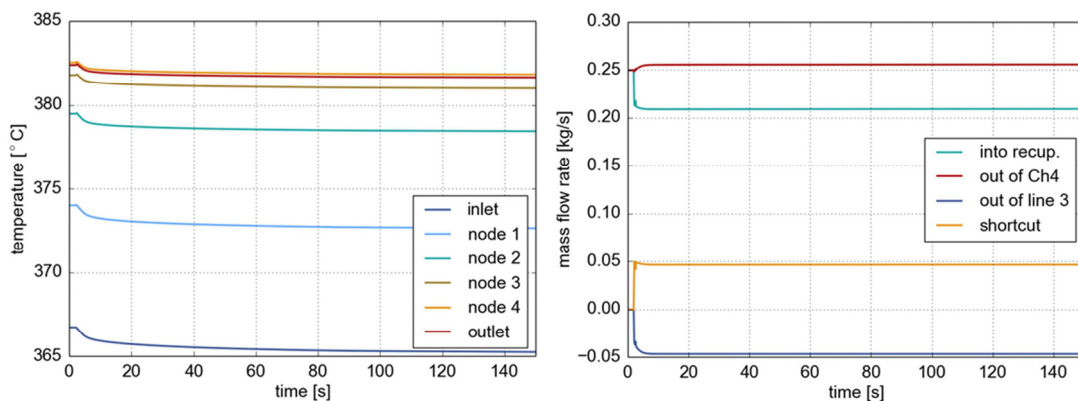


Fig. 7-14 A shortcut of 3 mm diameter between the emergency tube and channel 4 leads to slightly reduced coolant temperatures inside the test section (left).

In case of a crack with a flow area equivalent to a diameter of 3 mm, this effect results in a reduced maximum temperature of 382 °C as depicted on the left of Fig. 7-14. On the right hand side, the adapted mass flow distribution is shown. After the crack opens, the coolant leaving the test section (red) is distributed to the recuperator (green) tubes and to the emergency cooling tube (blue). Thus, the reduced pressure drop inside the fuel element leads to a slightly increased mass flow rate through the test section. A portion of ~ 0.05 kg/s of the provided coolant is taking the shortcut (yellow).

As scram does not occur, the temperature control system automatically reduces the rotational speed of pump CS in the cooler circuit to yield the primary circuit temperature set point of 300 °C. Thus, a new steady state operation point is reached approximately 1500 seconds after initiation of the crack,

¹³ Design by CVR, with permission from CVR from 2014.

as illustrated on the left hand side of Fig. 7-15. The diagram on the right shows the pressure progression inside the test section.

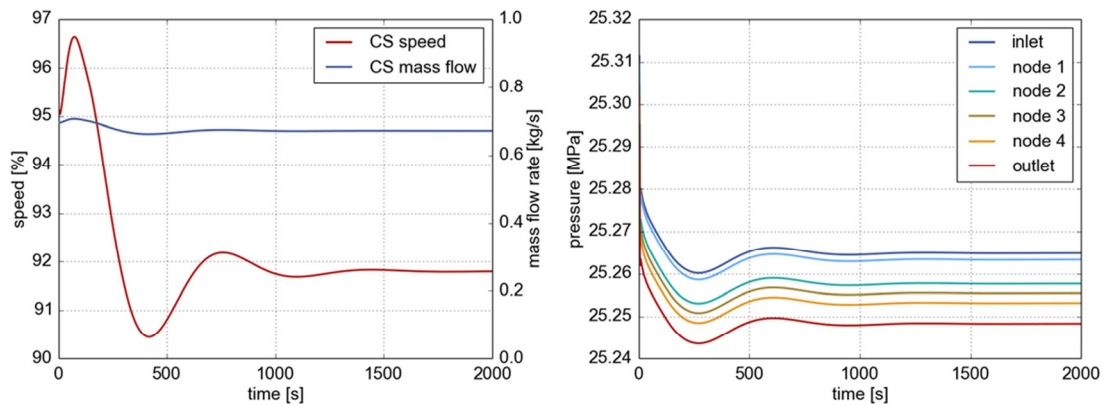


Fig. 7-15 Percental speed of pump CS and coolant mass flow rate of the secondary circuit (left). Slightly reduced pressures inside the test section (right).

A parametric study was performed, varying the flow area of the shortcut equivalent to diameters between 3 and 10 mm. As shown in Fig. 7-16, increasing the break diameter shifts the coolant mass flow rate distribution. An increased mass flow through the shortcut results in a reduced preheating and a maximum coolant temperature of only 376 °C for a diameter of 10 mm.

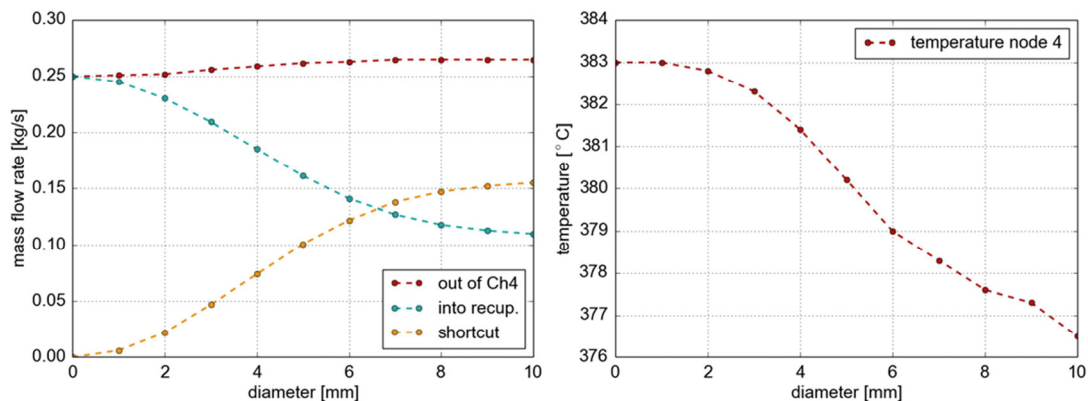


Fig. 7-16 Influence of shortcut diameter on coolant distribution (left) and maximum coolant temperature inside the test section (right).

7.5.2 Coolant Shortcut between Channel 1 and Channel 4

While a crack in the emergency line inside the test fuel element does not cause a problem, as the fuel rods are still well cooled, a crack in guide tube 1 (see Fig. 6-1), as illustrated by a cross section of the fuel element head shown in Fig. 7-17, allows the incoming coolant from channel 1 to bypass the test section and leave the fuel element directly via channel 4. In the worst case, this leads to a stagnation of flow inside the assembly box causing overheating of the fuel and the claddings.

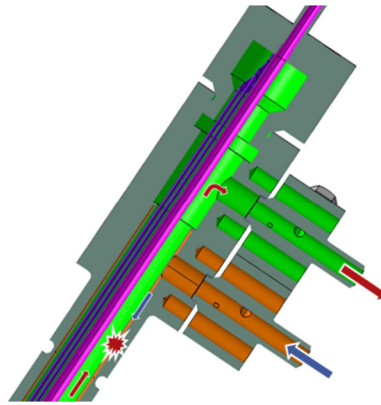


Fig. 7-17 Cross section of the fuel element head piece¹⁴: A crack in guide tube 1 allows the incoming coolant from channel 1 (orange) to bypass the test section via channel 4 (green).

In case of a small shortcut, up to a flow area equivalent with a diameter of 5 mm, a coolant mass flow of 0.12 kg/s through the test section is left which is just sufficient to cool the rods. The safety instrumentation does not even give a warning, as the maximum coolant temperature at the outlet of the test sections increases to 399 °C only, while the pressure is controlled by the spring-loaded pressure relief valve AV1.

In Fig. 7-18, simulation results are shown for a larger crack with an equivalent diameter of 7 mm.

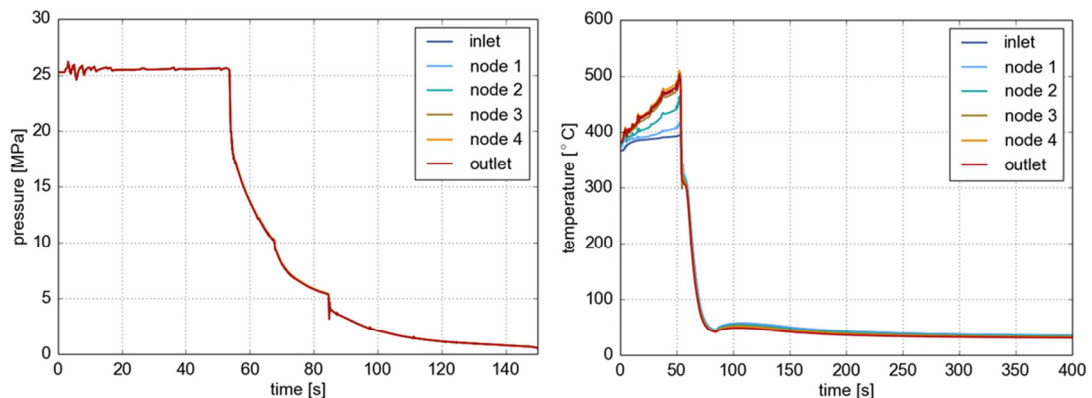


Fig. 7-18 Pressure (left) and coolant temperature progression (right) for a coolant shortcut with 7 mm diameter between inlet and outlet of the test fuel element.

Here, the coolant mass flow rate along the fuel rods drops below 0.08 kg/s, which causes a rise of coolant temperatures, shown on the right hand side of Fig. 7-19. However, the heat transfer to the supercritical water is still effective so that the cladding temperatures stay below 600 °C in this period. At the same time, the system pressure, depicted on the left of Fig. 7-19, is restricted by the pressure relief valve to 26 MPa, as visible from the small pressure fluctuations during the first 40 seconds of the transient. After ~10 s, the coolant temperature at the outlet of the test section would exceed 420°C, releasing a warning according to Tab. 2-2. After 52 seconds, the coolant temperature

¹⁴ Design by CVR, with permission from CVR from 2014.

limit of 500 °C would be exceeded, which causes a reactor shutdown and, one second later, the depressurization of the primary loop via valve ADS1. The following emergency heat removal taken over by the ELCI system is not negatively affected by the crack, as obvious from the coolant mass flow rate distribution shown on the right hand side of Fig. 7-19. Approximately half of the coolant mass injected over the emergency line flows downwards through the assembly box, whereas the other half leaves the fuel element over the recuperator.

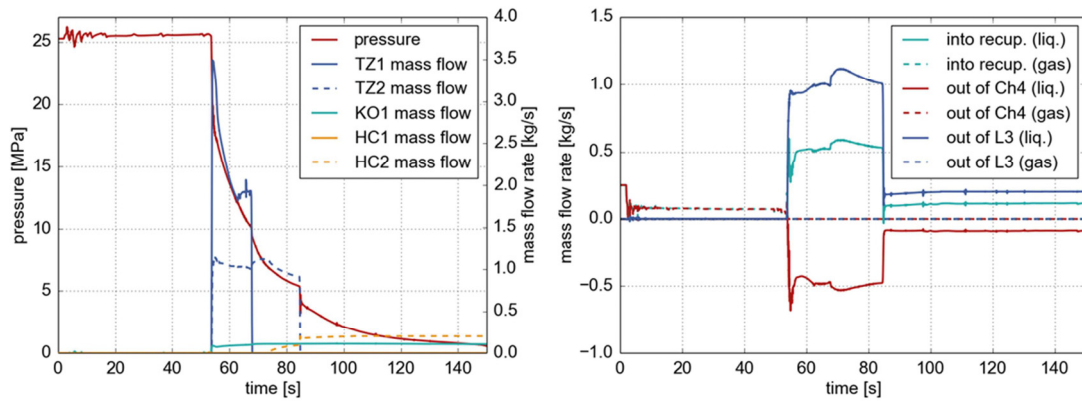


Fig. 7-19 System pressure and emergency coolant mass flows injected by the accumulators and pump HC2 (left). Coolant mass flow distribution inside the test fuel element (right).

Fig. 7-20 shows details of fuel rod power, mass flow rate, as well as coolant temperature and pressure at the assembly box outlet for the first five seconds after the scram. It takes around 1 second until the fuel rod power decreased to decay heat, whereas it takes two seconds until the flow reverses, driven by the injection of accumulator TZ2.

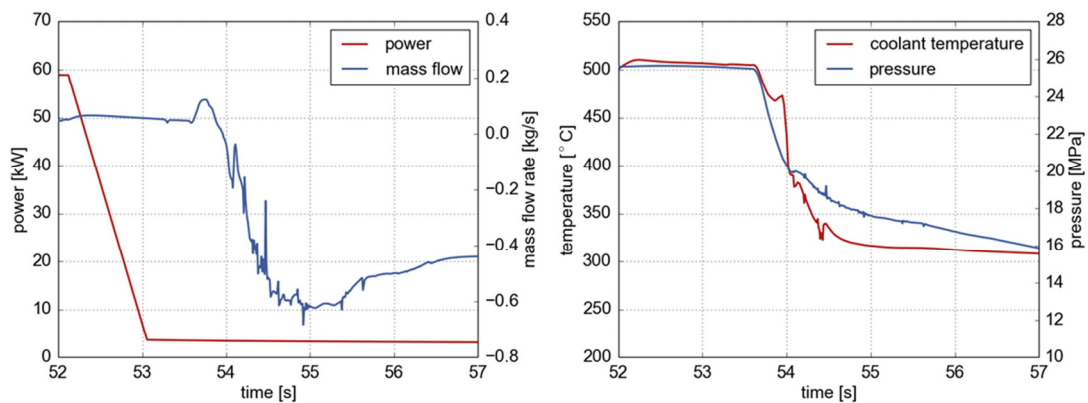


Fig. 7-20 Power of the fuel rods, coolant mass flow rate, temperature at the outlet of the test section, and pressure for a coolant shortcut between channel 1 and channel 4.

The progression of cladding temperatures after the scram is depicted in Fig. 7-21. Under supercritical pressure conditions, the cladding temperature does not exceed 600 °C. Once the pressure drops to subcritical conditions, the rods are immediately wetted and a boiling crisis is not to be expected.

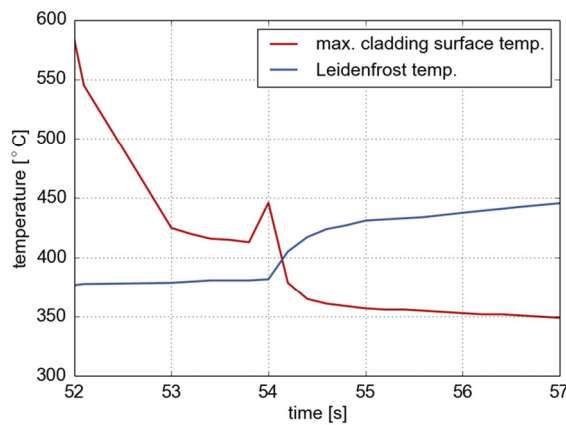


Fig. 7-21 Maximum cladding surface temperature and Leidenfrost temperature in case of a coolant shortcut between channel 1 and channel 4.

A further increase of the shortcut diameter does not change the progression of the accident sequence qualitatively, but the period of coolant heat up is shorter before the scram is activated.

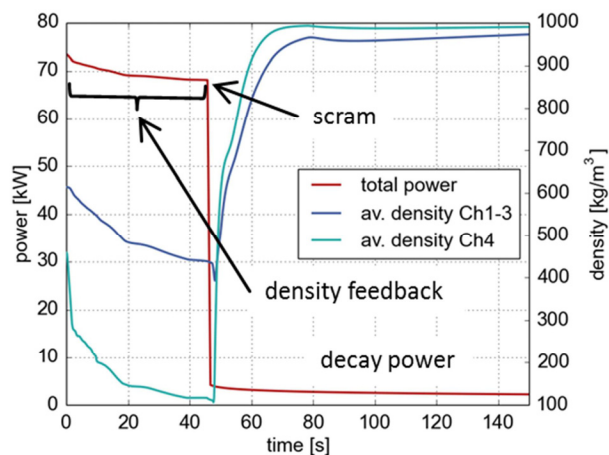


Fig. 7-22 Density feedback on power: total power and average coolant densities in channels 1 to 3 and channel 4 over time.

Fig. 7-22 shows the progression of power during the accident sequence. In the phase of coolant heat up, the total power decreases from 73.4 kW to 68 kW, due to a declining coolant density in the test section, as described in Chapter 4.1.1. At $t = 52$ s, scram is released and the power decreases linearly for 1 second of control rod insertion. From then on, the decay heat equation (7.1) is applied to determine the released residual heat.

7.6 Loss-of-coolant Accidents

To model a double-ended break of a pipe, a control valve in the respective line is immediately closed (driving time 0.1 s) to prevent flows in this direction. At the same time, connections between the two adjacent points and the environment – a point, which is taken out of simulation ($p = 0.1$ MPa) – are

opened. A loss coefficient of 1 is applied to simulate free discharge [68]. Check valves prevent in-flows into the system. The described large break LOCA model is depicted in Fig. 7-23.

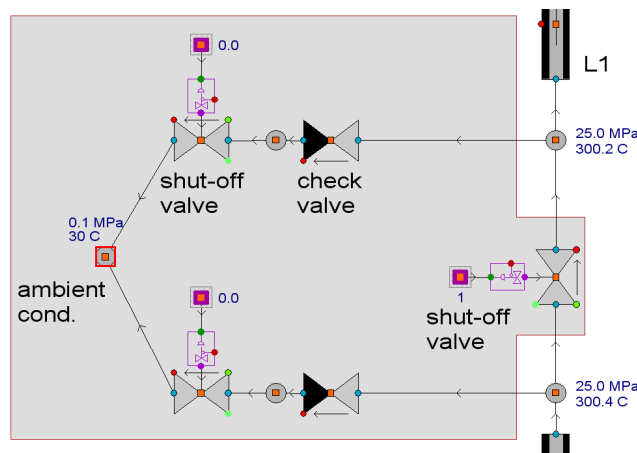


Fig. 7-23 Modeling of a large break LOCA with APROS.

7.6.1 Large Break of the Emergency Cooling Line L3

The phenomena occurring in the test section in case of a loss-of-coolant accident can easiest be explained by a postulated large break of the emergency cooling line L3, shown in Fig. 2-6. Starting from steady state operation as described in Chapter 0, a sudden, guillotine break of the entire emergency cooling line L3 is assumed to occur 1.4 m behind pump HC2 at time 2 s. The history of the fuel bundle power, as well as the mass flow, pressure and temperature of the coolant at the inlet of the test section are zoomed out for the first two seconds after the break initiation in Fig. 7-24.

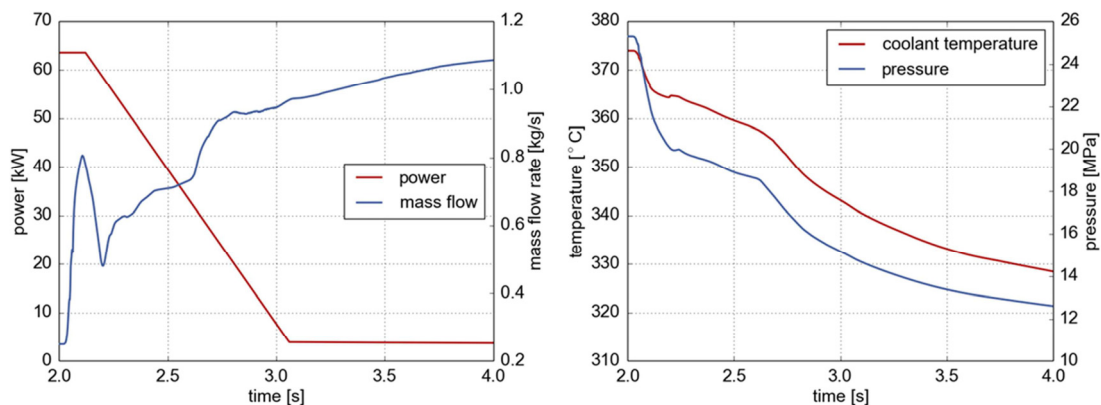


Fig. 7-24 Power of the rod bundle, history of the coolant mass flow, coolant temperature and pressure after opening a large break in line L3 at time 2 seconds.

Right after the break opened, the coolant starts to be ejected through the open emergency cooling line, increasing the mass flow through the test section to about 0.8 kg/s within ~0.1 seconds. Simultaneously, the pressure drops to sub-critical conditions, and the coolant temperature is reduced to the saturation temperature at this pressure. Scram is released at a pressure of 22.5 MPa with a delay time of 0.06 s only. Reflection of the pressure wave causes first a minimum mass flow at ~2.2 s, but the

mass flow is increasing shortly afterwards again. The claddings of the fuel rods are even better cooled under these conditions than at the supercritical, steady state condition before. The cladding surface temperature and the Leidenfrost temperature, predicted analytically with Eq. (3.35), are shown in Fig. 7-25. When sub-critical pressure is reached, the claddings are already colder than the Leidenfrost temperature and are wetted immediately.

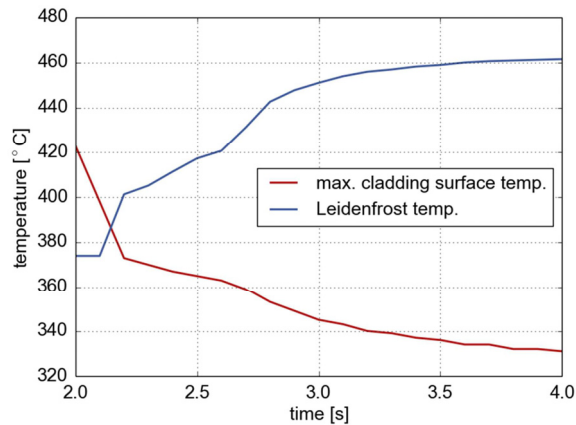


Fig. 7-25 Maximum cladding surface temperature and Leidenfrost temperature after a large break of line L3.

During the next 5 s, the water inventory of accumulator TZ2 is just fed into the break, but accumulator TZ1 can replace the missing coolant up to 30 s, as shown in Fig. 7-27.

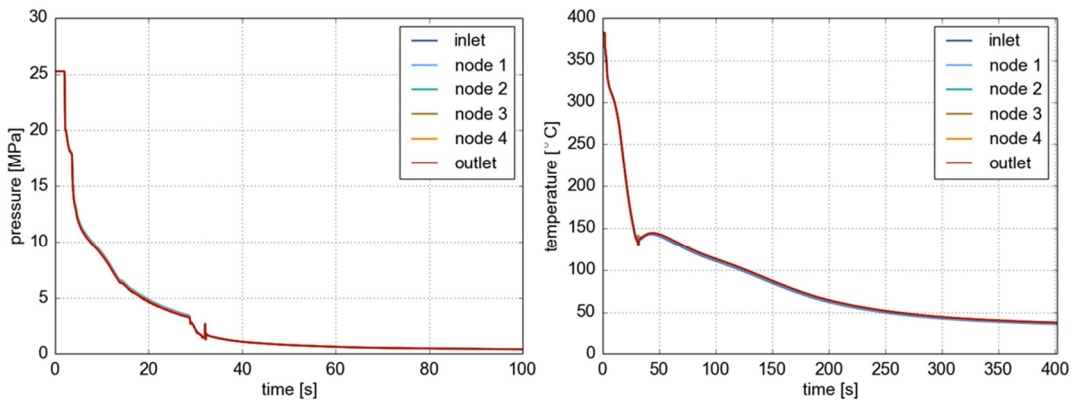


Fig. 7-26 Histories of pressure and coolant temperature after a large break of the emergency cooling line L3.

The opening of the automatic depressurization system ADS2 does not cause any significant effect on coolant mass flow. At a pressure of 12 MPa, about 19 s after scram, the FLCI pump HC1 starts injecting water from the emergency coolant reservoir HN1 and the mass flow from accumulator TZ1 is slightly reduced accordingly. Once TZ1 is empty, a coolant mass flow rate of 0.2 kg/s is supplied by the emergency pump, causing a short peak of the coolant temperature at 45 s, but temperature and pressure are decreasing steadily afterwards again, depicted in Fig. 7-26. During the entire emergency cooling phase, the secondary cooling circuit is kept running.

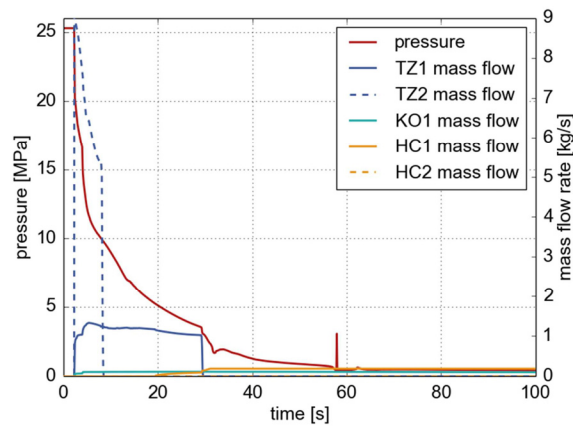


Fig. 7-27 Assembly box pressure and emergency coolant mass flow rate provided by the accumulators and pump HC1.

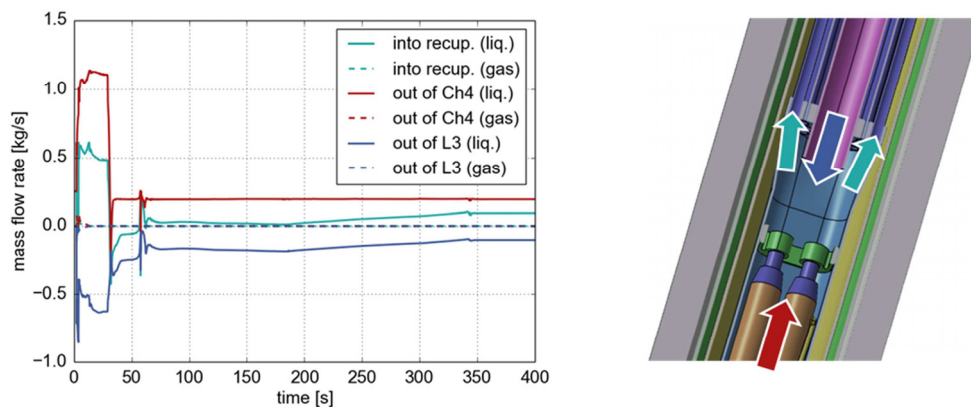


Fig. 7-28 Coolant mass flow rate distribution inside the test fuel element with schematic illustration of flow paths in the transition piece between assembly box and recuperator section¹⁵. Red – coolant flowing upwards through the assembly box, blue - coolant ejected from emergency line L3, cyan – coolant entering the recuperator. The orientations of the arrows indicate positive flow directions.

Fig. 7-29 shows the progression of water inventory of the depressurization tank BN and the emergency coolant reservoir HN1. The refilling pump HC3, installed in the connecting line between both tanks, can be used to regain water for continued residual heat removal in case of an intact primary circuit. In case of a rupture of line L3, however, about 50 % of the coolant mass flow is lost through the break in L3 line (blue in Fig. 7-28); the rest is collected in the depressurization tank (cyan in Fig. 7-28). Thus, after 2370 seconds, the water level in tank BN exceeds the limit of 1.1 m, which automatically activates pump HC3 until the level falls to 0.8 m again. At 6350 seconds, tank HN1 is getting almost empty: its water level reaches the minimum limit of 0.2 m. Again, water is retransferred from tank BN to tank HN1. After 16200 s (4.5 h), both tanks would be empty if they had not been refilled from outside.

¹⁵ Design by CVR, with permission from CVR from 2014.

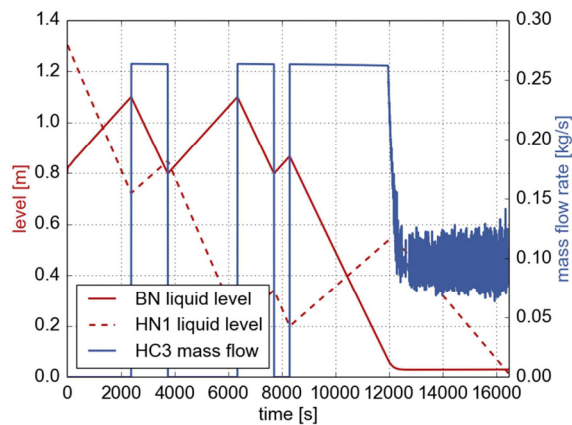


Fig. 7-29 Water level inside depressurization tank BN and emergency cooling reservoir HN1 and mass flow rate delivered by the interconnected refilling pump HC3.

In total, the water inventory of both tanks of 1.65 m³ suffices for active residual heat removal of 4.5 hours. Within this period, the lost water must be replaced. For this purpose the experimental hall will be equipped with a sump in order to collect the spilled water. This will be done by collecting the spilled-out water from the system to the sump placed underneath the primary block. Furthermore, the level of sump should be above the depressurization tank in order to allow a flow back to this tank (otherwise, a small additional pump needs to be added).

During the total simulation period of 4.5 hours, the temperature of the circulating water in the primary loop stays below 50 °C.

Other break locations have been tested as well, but the exact break location turned out to be of minor importance for the accident scenario of a rupture of the emergency cooling line.

Discussion

In case of any break of the primary system, both accumulators supply their water inventory of 30 liter each within 10 to 30 s, to provide a grace period for the emergency cooling pumps to start. In case of a break of line L3, the accumulator TZ2 of the ELCI system will just feed into the break. It will not provide any coolant to the test section, but the other accumulator TZ1 will help to cool down the fuel rods effectively, avoiding a boiling crisis during depressurization. Only pump HC1 of the FLCI system can remove the residual heat afterwards in this case. Therefore, it will be important to ensure that the ELCI system is not activated instead. A comparatively small coolant mass flow rate of 720 l/h is sufficient to keep the fuel rods wetted. A higher mass flow is undesired to maximize the time until the coolant reservoirs, tanks HN1 and BN, will be empty. Opening of the automatic depressurization system ADS2 can help to extend this time period, as some of the injected water is kept in the system, but it cannot avoid that the coolant will sooner or later be lost and must be replaced.

7.6.2 Large Break of the Return Line L2

The situation is similar if a large break of the return line L2 is regarded. The break location is assumed to be 0.9 m upstream of pump HCC. Again, the mass flow through the test section is even

increased during the accident, as shown in Fig. 7-30 for the first 2 s after the break. The pressure wave coming from the break is causing again a short peak of the mass flow within ~ 0.1 s and the pressure drops to sub-critical conditions, releasing a scram of the reactor at ~ 2.1 s. Opening of the automatic depressurization system ADS2 at 1.6 s does not have any effect on the conditions inside the test section since line L2 is open anyway.

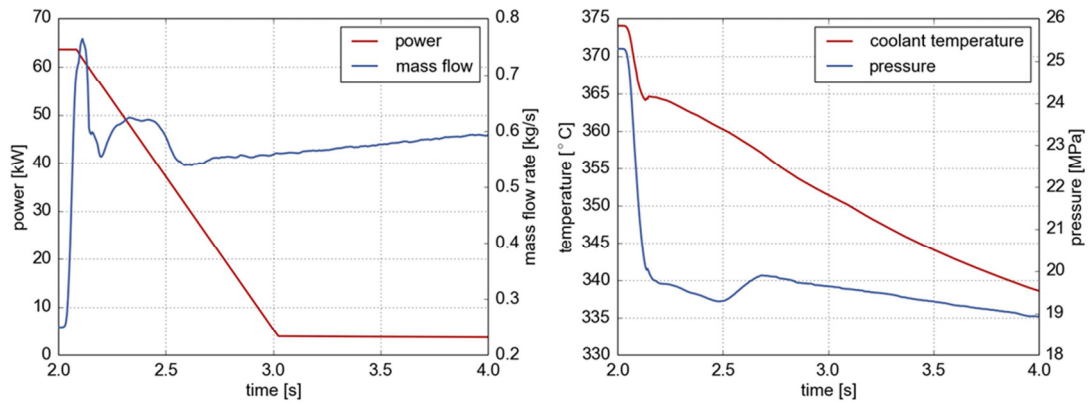


Fig. 7-30 Power of the rod bundle, history of the coolant mass flow, coolant temperature and pressure after opening a large break in line L2 close to pump HCC at time 2.

The following pressure reduction is slower now than in the last case, as the small recuperator tubes are causing some pressure loss between the test section and the break. As a consequence, the Leidenfrost temperature does not increase so rapidly and the cladding surface temperature stays hotter than the Leidenfrost temperature during the first second. Therefore, we observe post-dryout conditions for a period of ~ 1 s, as shown in Fig. 7-31. However, the peak temperature is still less than 492 °C and the Leidenfrost temperature is reached again short afterwards at ~ 3.1 s. There, a quench front runs from the inlet to the outlet of the test section, which is rewetting the claddings again.

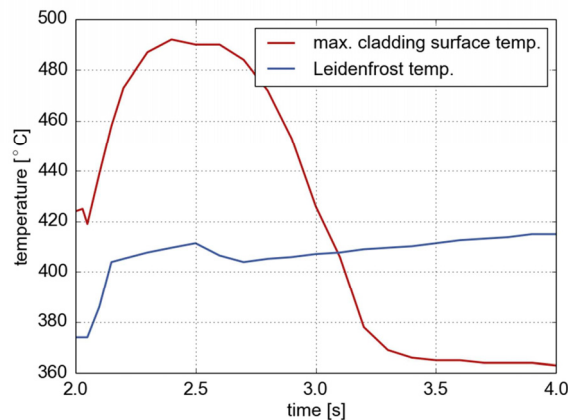


Fig. 7-31 Maximum cladding surface temperature and Leidenfrost temperature after a large break in line L3, predicted with Eq. (3.35).

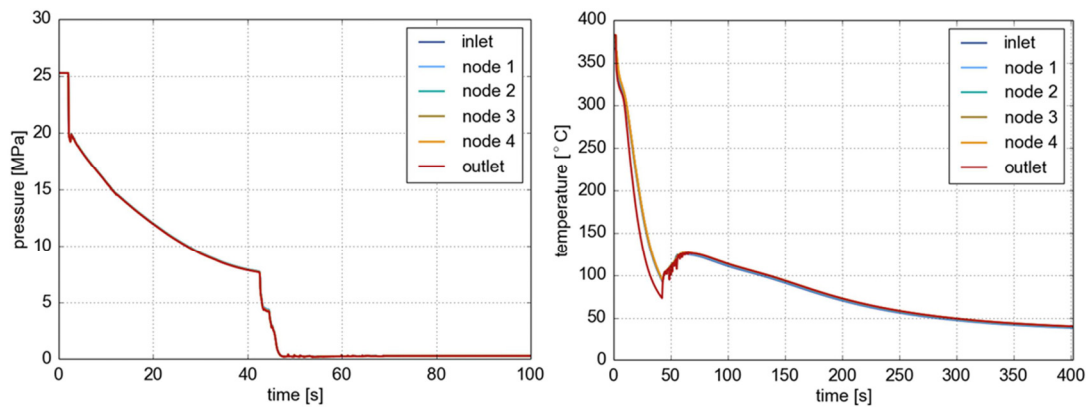


Fig. 7-32 Histories of coolant temperature, pressure and mass flows after a large break of the coolant return line L2.

Temperature and pressure histories are shown in Fig. 7-32. The missing coolant is supplied again from accumulator TZ1, which needs 45 s now to become empty as the total mass flow through the fuel element is limited to approximately 1.5 kg/s, which is injected in relatively equal parts by both accumulators, depicted in Fig. 7-33 (right). The reduced temperature appearing in the outlet node is caused by the coolant jet injected via the emergency line, which is penetrating into the assembly box during the first 43 seconds. When a pressure of 12 MPa has been reached, the coolant pump HC1 starts injecting into line L1, providing the only mass flow after 45 s, once accumulator TZ1 is empty, as illustrated on the left hand side of Fig. 7-33.

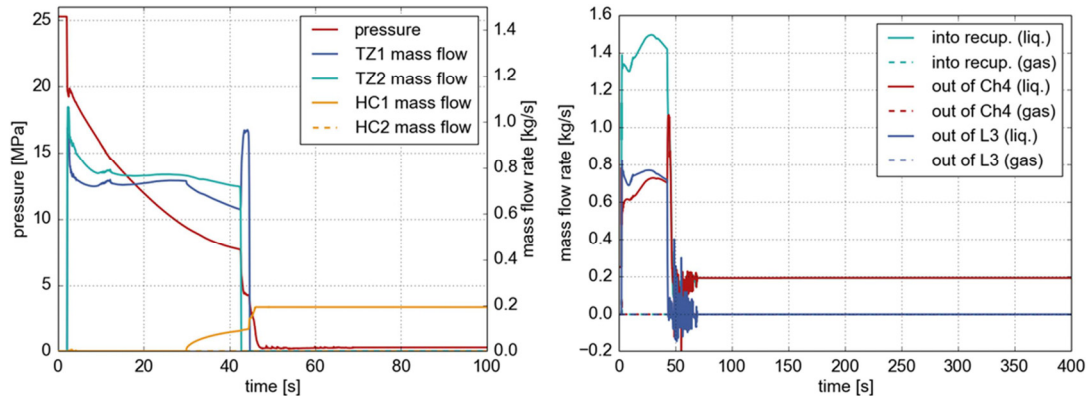


Fig. 7-33 System pressure and emergency coolant mass flow rate provided by the accumulators and pump HC1 (left) with the resulting mass flow distribution inside the test fuel element (right).

In case of a break of the return line L2, all coolant injected by the feed line cooling injection system FLCI gets lost through the break. Fig. 7-34 shows that the liquid level inside the emergency coolant reservoir HN1 reaches the lower limit of 0.2 meters approximately 1 hour and 15 minutes after scram. The reservoir is first refilled by water from the pressure suppression tank BN, but the lost water must be replaced \sim 1 hour later at latest.

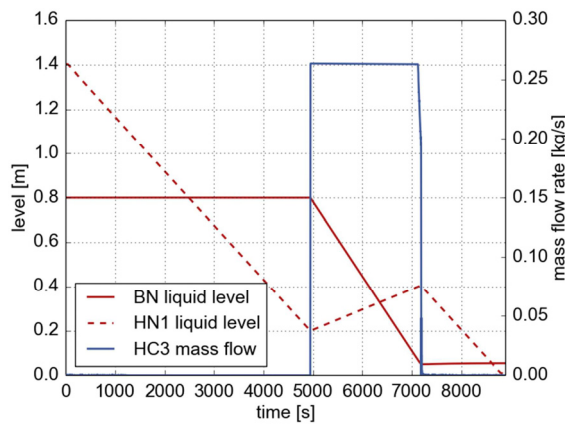


Fig. 7-34 Water level inside depressurization tank BN and emergency cooling reservoir HN1 and mass flow rate delivered by the interconnected refilling pump HC3.

Discussion

In case of a break of line L2, both accumulators provide coolant to the test section simultaneously, and both pumps HC1 and HC2 could remove the residual heat afterwards, in principle. The automatic pressurization system ADS2 is opened automatically, but it does not have any effect, being close to the break. Again, the safety system ensures that the second barrier will not be damaged if the third barrier failed. Cladding surface temperatures exceeding the material limit of 816 °C during such short term transients are not to be expected.

7.6.3 Large Break of the Feed Line L1

The situation is getting more complex if we assume a large break of the feed line L1. This simulation assumes a break 1.4 m in front of the fuel element inlet. Fig. 7-35 shows the pressure and coolant temperature progression inside the assembly box. Again, the break is assumed to happen at time $t = 2$ s and is followed by a sharp pressure and temperature drop to saturation condition.

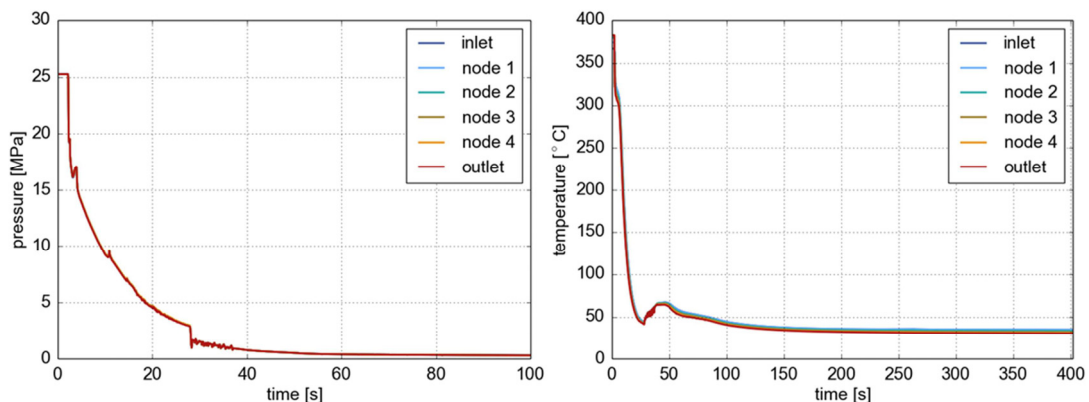


Fig. 7-35 Pressure and coolant temperature progression inside the assembly box for a rupture of the feed line close to the inlet of the fuel element.

Now the leakage through the break causes the coolant to run backwards and the outlet in Fig. 7-35 becomes the inlet. Again, the pressure drop causes a scram of the reactor after ~ 0.1 s, and both passive accumulators inject their coolant inventories. Accumulator TZ1 is just feeding into the break, but accumulator TZ2 can inject coolant now onto the test section through the emergency cooling line L3.

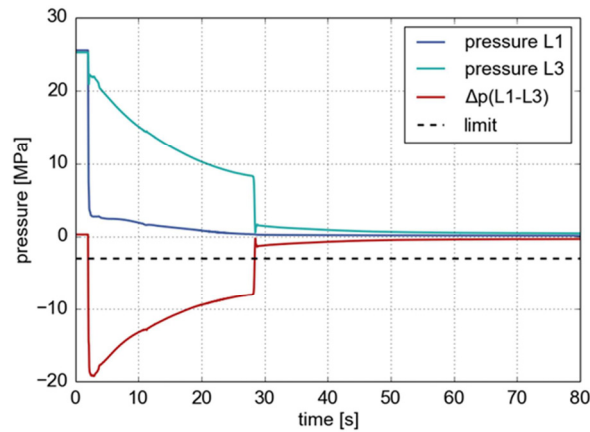


Fig. 7-36 Pressure progression in lines 1 and 3 close to the fuel element connection. The scram is released by the Δp signal as soon as the differential pressure (L1 - L3) falls below the threshold at -3 MPa.

The reverse flow causes a negative pressure difference L1 - L3 of up to 18 MPa, shown in Fig. 7-36, which activates the emergency cooling pump HC2, which starts to inject 18 seconds after scram through the emergency cooling line system ELCI, as illustrated on the left hand side of Fig. 7-37. The right hand side of Fig. 7-37 shows that it takes around 250 seconds after accumulator TZ2 has been depleted until the coolant mass flow injected via the emergency line L3 is equally distributed in two fractions.

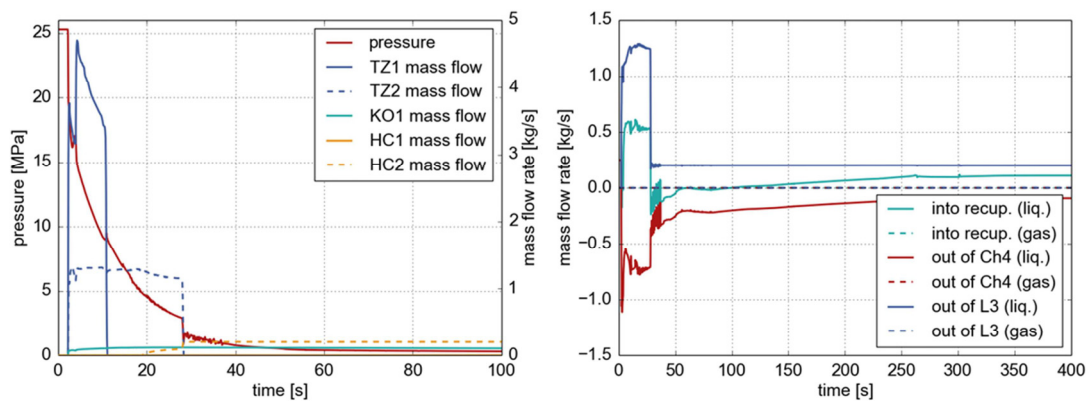


Fig. 7-37 Emergency coolant injection by the accumulators and pump HC2 with resulting mass flow distribution inside the test fuel element.

One fraction is passing and cooling the fuel rods in channel Ch4 (shown in red), whereas the other fraction leaves the fuel element in opposite direction through the recuperator tubes, through line L2 and finally through pump HCC to the break and to the depressurization tank via ADS1 (shown in

cyan). The pressure loss in the pump (loss coefficient estimated as ~ 32 by Hermetic Pumpen) is not hindering this reverse flow significantly.

Fig. 7-38 illustrates the power, mass flow, as well as pressure and temperature histories at the outlet of the test section during the first two seconds after the break occurred. At 2.06 seconds, the reactor is scrammed as a low system pressure is detected. During fuel rod insertion, which needs one second, the power decreases linearly to residual heat, which is below 4 kW. At the same time, the coolant flow direction inside the assembly box gets inverted due to the emergency injection over line L3.

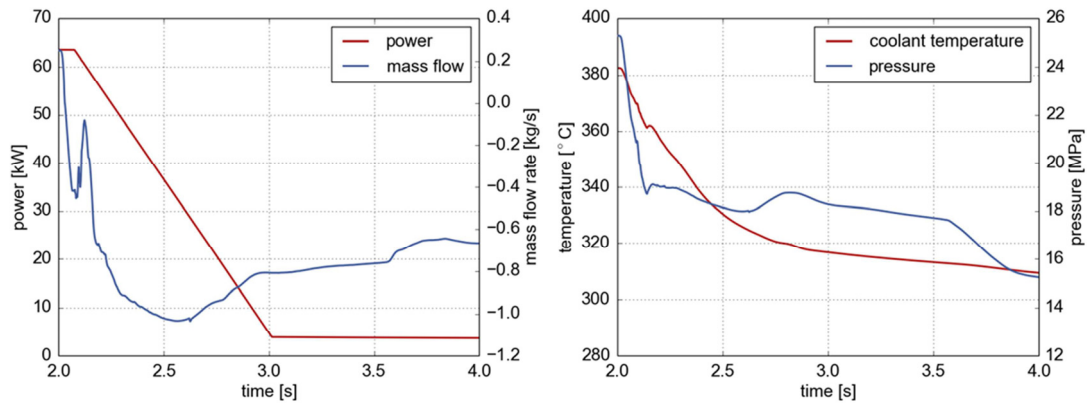


Fig. 7-38 Power of the rod bundle, history of the coolant mass flow, coolant temperature and pressure after opening a large break in line L1 close to the fuel element connection at time 2.

The temperature plot in Fig. 7-39, predicted analytically with Eq. (3.35), shows that the maximum cladding temperature slightly increases immediately after the break occurred. But, as soon as the pressure falls to subcritical and the control rods are released, it clearly drops below Leidenfrost temperature and the fuel rods are well cooled.

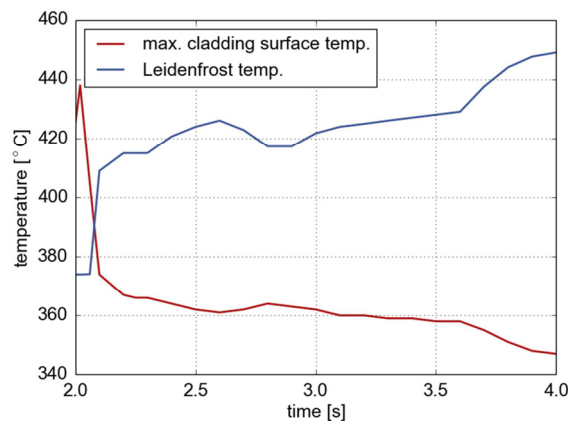


Fig. 7-39 Maximum cladding surface temperature and Leidenfrost temperature after a large break in line L1 close to the fuel element, predicted with Eq. (3.35).

Compared with the loss-of-coolant accidents discussed in the subsections before, the exact break location in the feed line has a larger impact on the accident sequence. Fig. 7-40 shows again pressure

and coolant temperature distribution in the test section. In this example, the break location is assumed to be 0.3 m downstream of the pressure side of recirculation pump HCC. The pressure progression in this case is almost identical to a break close to the fuel element head; the coolant temperatures in the test section, however, differ significantly within the first 300 seconds. As illustrated on the right hand side of Fig. 7-40, another heat up of the coolant along the fuel rods is found after the quenching period of accumulator TZ2, which is due to the small mass flow during this period, illustrated with a red line in Fig. 7-41 (right). The bottom part of the test section, still denoted as inlet in Fig. 7-40, is even reaching the saturation temperature.

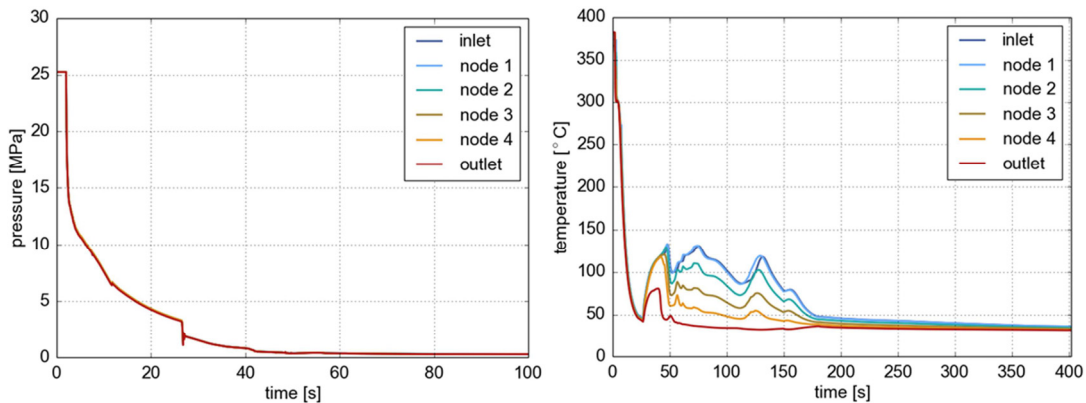


Fig. 7-40 Pressure and coolant temperature progression inside the assembly box for a break of the feed line close to the recirculation pump HCC.

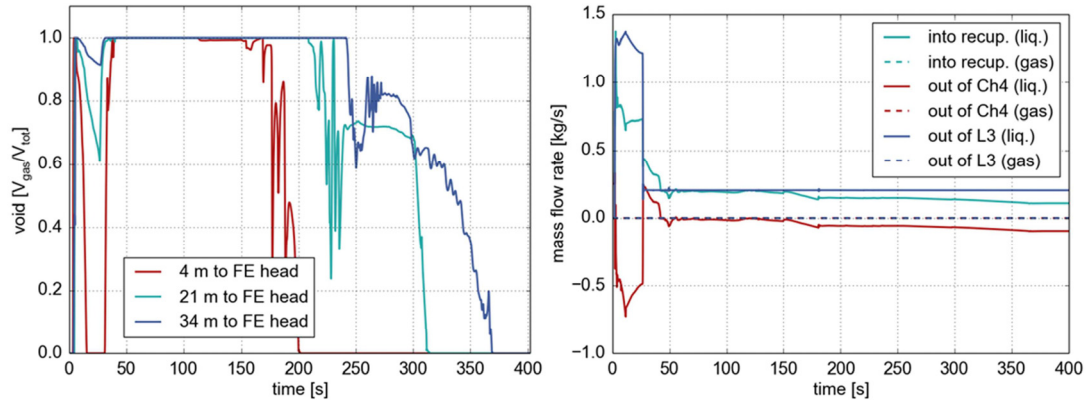


Fig. 7-41 Void fraction in line L1 (left) during emergency coolant injection through line L3 and split of coolant mass flow through recuperator and test section Ch4 (right).

This effect is caused by coolant heat up at the fuel rods, and evaporation at the surface of the hot pressure tube and along line L1, which is still hot. The presence of vapor is increasing the pressure drop along this flow path significantly, causing the coolant to run rather backwards through recuperator and cooler, where evaporation is avoided. We see in Fig. 7-41 on the left hand side that line L1 is mostly voided during this period. It takes until ~ 350 s before line L1 is filled with liquid and 50 % of the injected coolant is available for the test section again.

Fig. 7-42 depicts the progression of fuel rod power and coolant mass flow rate, as well as coolant temperature and pressure for the first seven seconds after a full break of the feed line close to recirculation pump HCC.

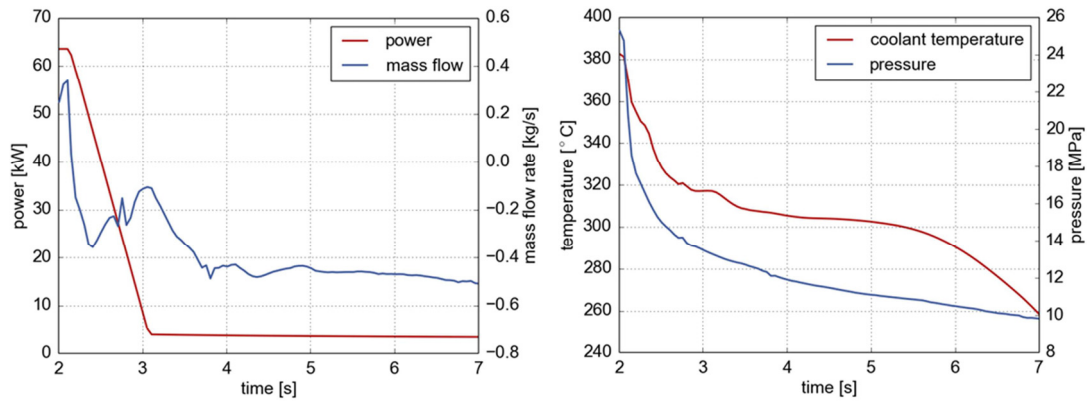


Fig. 7-42 Power of the rod bundle, history of the coolant mass flow, coolant temperature and pressure after opening a large break in line L1 close to pump HCC at time 2.

Similar to the break close to the fuel element discussed before, the reactor gets scrammed right away due to the dropped system pressure. Again, the rigorous coolant injection of accumulator TZ2 drives the flow inside the assembly box in downward direction. Thus, as visible from Fig. 7-43, the fuel rods get immediately quenched. However, due to the sudden pressure decrease, the coolant evaporates in the lower part of the test section during the first two seconds with a maximum void fraction of 85 % as shown in Fig. 7-44.

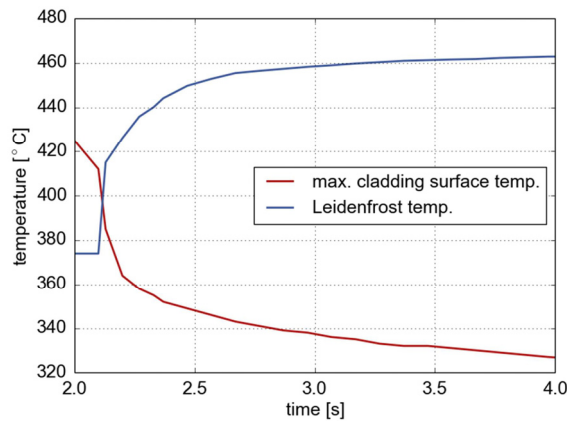


Fig. 7-43 Maximum cladding surface temperature and Leidenfrost temperature after a large break in line L1 close to recirculation pump HCC, predicted with Eq. (3.35).

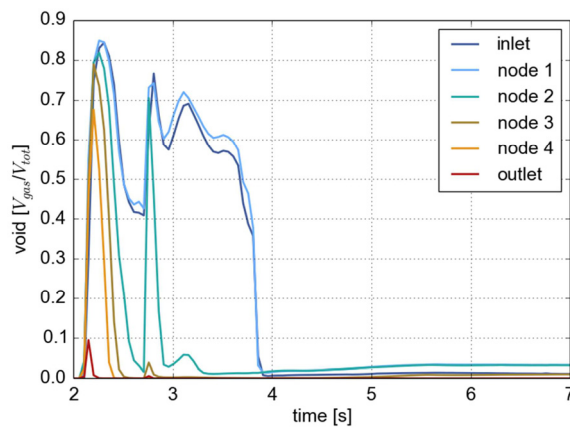


Fig. 7-44 Void fraction inside the test section directly after opening the break.

The performance of the safety systems is also checked by simulating smaller breaks of the feed line close to the fuel element connection. In case that a hole of 1 mm is assumed, the Δp -signal does not get activated. However, after eight seconds, the system pressure falls below 22.5 MPa and the feed line injection system FLCI is activated. As the mass flow through the break is only 0.015 kg, sufficient coolant was left inside the system for an effective residual heat removal. Larger break sizes are handled by emergency system ELCI again, activated by a reversed flow, in the same manner as in the sequences shown above.

Discussion

In case of a large break of the feed line L1, the ELCI system is the only emergency cooling system which can supply coolant to the test section, as the FLCI will feed into the break. From the top of the test section, the coolant from line L3 can flow to the assumed outlet via two different routes: one fraction is cooling the test section and flows backwards through line L1 as intended, and the other fraction runs in opposite direction via the recuperator, the cooler, line L2, and through pump HCC to the same outlet. This flow split reduces the coolant mass flow along the fuel rods. For break locations close to the recirculation pump, the flow through the test section and through the broken feed line L1 is heated up, reaching even saturation temperature within the first six minutes, whereas the reverse flow is cooled, staying liquid. This effect increases the flow resistance through the test section and through line L1 significantly, decreasing the mass flow in the intended direction even further. Nevertheless, the accident analyses confirm that the peak cladding surface temperature will not exceed the design limits.

8 Beyond-design-basis Accident with In-containment Source Term Analysis

As discussed in Chapter 7, the applied safety systems are able to mitigate design basis accidents covering a number of anticipated, single-component failures. These systems reliably detect accidental conditions, scram the reactor and initiate the emergency cooling via the intended injection line, including the depressurization of the loop. Due to a sophisticated logic of signals and actions (Tab. 2-2) the integrity of the test facility is never endangered. It is proven that either the primary loop (third barrier) or the claddings (second barrier) stay intact and thus no radiological release is to be suspected. Different from these analyses, this chapter focuses on a beyond-design-basis accident and its radiological consequences. (Further beyond-design-basis accidents, such as mechanical failures of the pressure tube and potential secondary damages are discussed by Zeiger et al. [89], [90]). The aim of this investigation is to determine an in-containment source term, which allows the evaluation of radiological hazards for the facility operators in case of an eventual severe multi-component failure. In a first step, a hypothetical accident scenario of the highly unlikely case of a combined failure of barriers 1 to 3 is simulated with APROS in order to obtain the worst case fuel centerline temperature. This temperature sequence is then used in a second step to evaluate the radiological source term of the overheated fuel, which is assumed to propagate without any further filtering into the experimental hall. For this purpose, the CORSOR-O fractional release rate model of Lorenz and Osborne [91], developed at the Oak Ridge National Laboratory, has been applied.

8.1 Accident Scenario

The investigated beyond-design-basis accidental scenario, which may possess a very low probability of occurrence, is a double-ended guillotine rupture of the feed line. This means an immediate loss of the third barrier. As the rupture is located inside the shielded duct between reactor and experimental hall, leaking fluids are free to enter the experimental hall. This laboratory is operated at 20 Pa sub-atmospheric pressure. The hermetically sealed room has a volume of 1762 m³. It is equipped with a filtering system, which is capable to handle 17620 m³/h of air and which keeps the pressure sub-atmospheric even in case of a major LOCA accident. Fig. 8-1 shows the site plan with reactor hall and adjacent experimental hall. The test fuel element is linked to the handling and safety systems via two coolant supply lines and the emergency line. In the connection between reactor and experimental hall, the piping is enclosed by a shielded bridge. Together, the reactor, the duct and the experimental hall form a gastight containment.

A further aggravation of the initiating event is caused by a black-out in combination with the failure of all onsite emergency power supply systems. This prevents the emergency pumps from starting-up and stops the secondary circuit flow. However, for the first 25 seconds after the accident initiation, the cooling of the rods is still ensured by the injection of the passive pressure accumulator TZ1. After this period, heat removal happens solely via conduction over the flooded insulation gap. The assumed thermal-hydraulic boundary conditions at the break location are saturated steam with $T = 100\text{ }^{\circ}\text{C}$ at $p = 0.1\text{ MPa}$. The scenario assumptions are listed in Tab. 8-1.

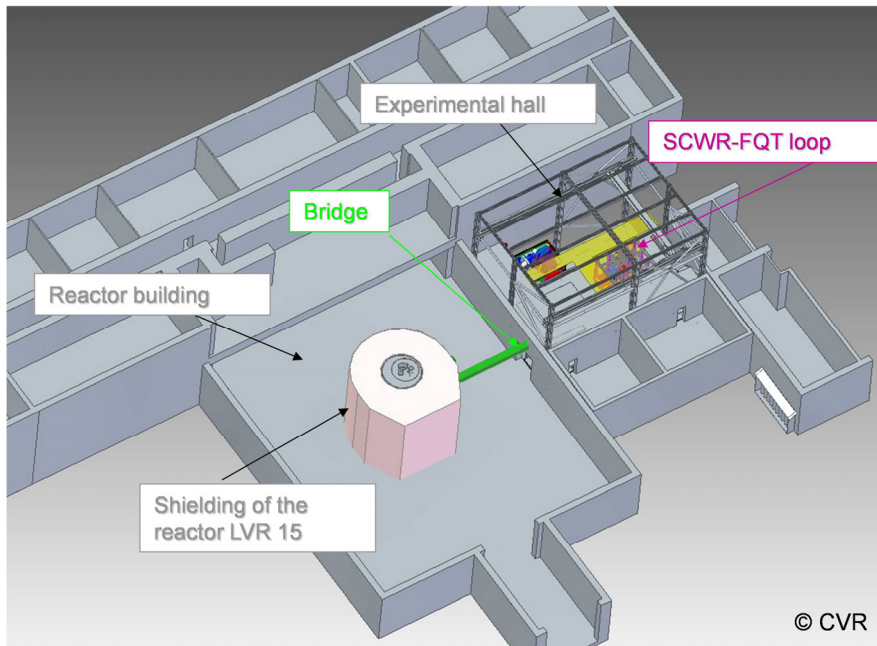


Fig. 8-1 Site plan of the reactor building and adjacent experimental hall¹⁶.

Tab. 8-1 Postulated accident scenario for a loss of coolant in combination with a total loss of power.

- Guillotine break of feed line L1
- Reactor is scrammed
- Failure of all emergency cooling pumps (loss of off-site power and failure of emergency power (diesel & batteries))
- Failure of the cooling circuit pump
- Both accumulators TZ1 and TZ2 inject for the first 25 seconds
- Heat transfer to reactor pool via flooded gap
- Failure of cladding, but fuel rod geometry unchanged
- Water temperature in the insulation gap $T = 50\text{ °C}$ (const.)
- Ambient conditions at break point: $T = 100\text{ °C}$, $p = 0.1\text{ MPa}$ (steam)

¹⁶ Design by CVR, with permission from CVR from 2014.

For the first 25 seconds of the accident sequence, APROS predicts a similar coolant temperature progression as for a break of the feed line L1, presented in Chapter 6. As long as accumulator TZ1 injects coolant into the system, the temperatures in the test section decrease rapidly. Contrary to the before simulations, no subsequent active cooling is available under the assumptions taken here. Thus, the stagnant water inside the assembly box heats up due to the residual power of the fuel until it reaches saturation temperature at $t = 80$ s. Since the coolant inventory of the test section is small, the entire water inside the assembly box is evaporated already after a period of approximately 400 seconds, being followed by a drastic temperature increase, as depicted on the left hand side of Fig. 8-2. As given by the safety criteria described in Chapter 2.3.2, the second barrier will certainly fail, as the obtained cladding temperatures exceed the limit of 816 °C by far. The predicted peak temperature is close to the melting point of the claddings. From that moment on, the shielding and retention capacity of the cooling system is lost and airborne radioactive material is free to enter the loop. As the pressure tube would mostly be voided then, the radioactive material would enter the experimental hall without filtering. Even though the integrity of the claddings will certainly be lost, it is assumed in this analysis that the fuel rod geometry maintains unchanged. The obtained cladding temperature progression at different heights of the fuel rods is illustrated on the right hand side of Fig. 8-2 for the entire simulation time of approximately 200 minutes. After reaching a maximum temperature of 1400 °C the temperature decreases slowly due to decreasing decay power. The progression of residual power is plotted on the left hand side of Fig. 8-3. According to the peak fuel centerline temperatures, damage of the fuel bundle must be expected. However, melting of the UO_2 pellets ($T_{\text{melt}} = 2865$ °C) and failure of the pressure tube are unlikely.

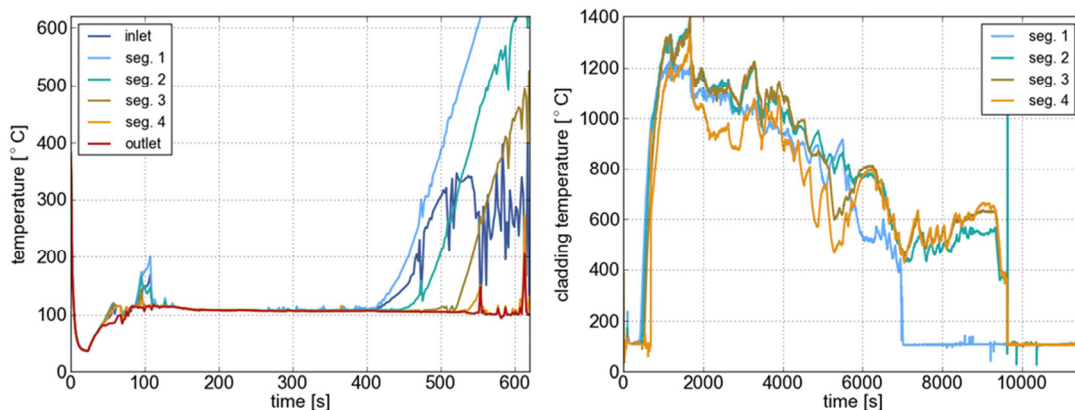


Fig. 8-2 Coolant temperatures along the fuel rods for the first 600 seconds (left) and the total simulation time of 200 minutes (right). Inlet and outlet denote the lower and upper end of the assembly box. Segments 1 to 4 are in between.

The progression of the fuel pin centerline temperature of segment 3, depicted on the right hand side of Fig. 8-3, is used for the following determination of the resulting radiological source term.

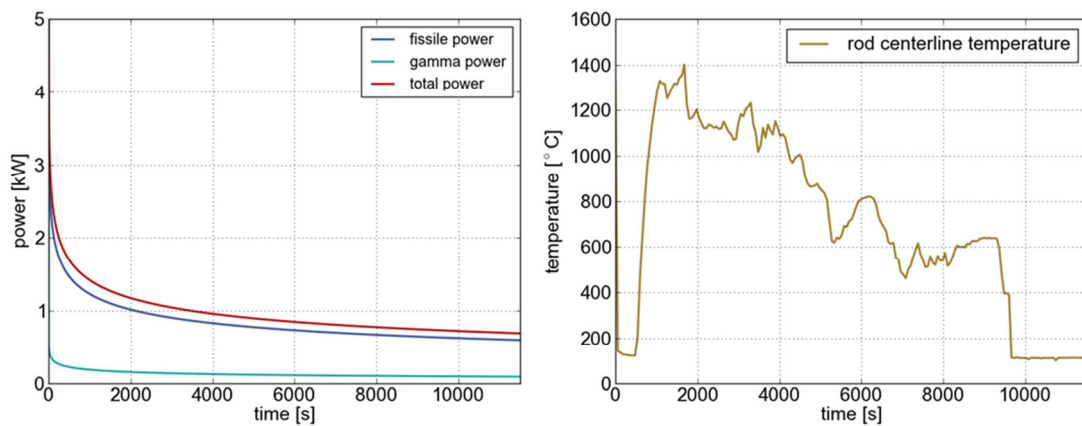


Fig. 8-3 Progression of heating power (left) and rod centerline temperature used as basis for the source term evaluation (right).

8.2 Release Rate Model CORSOR-O

During normal operation, only a few percent of the fission products leave the binding fuel matrix, which thus forms the first safety barrier against release of radioactivity into the environment. However, as soon as the fuel heats up during accidental conditions, additional large-scale fission product release is caused due to thermal processes up to vaporization of fuel and structural materials. A detailed description of five principal mechanisms, which control the rate of release of fission products from LWR fuel under such conditions has been provided by Wichner et al. [92]. As outlined by Silberberg et al. [93], this fuel heat up results in a significant release of noble gases (Xe, Kr), volatile species such as I, Te and Cs and alkaline earth radionuclides (Sr and Ba). In this way, radioactivity can exit the primary system as gas or aerosols through the break. Possible transport mechanisms are affected by the physical form of the fission products. At high temperatures, they are released as atoms, which might combine with vaporized material or other fission products, e.g. as CsI. In the vapor form, they are very mobil but they will in turn condens on aerosols or on structural surfaces. Another important influence on the transport mechanisms is given by the present atmosphere. It was found in the experiments of Lorenz and Osborne [91] that less than 1 % of the released iodine is in volatile form (I_2 , HI, or CH_3I), which is important since these forms are able to remain for long duration in the gas phase. In contrast, in a steam atmosphere, as it might be present in the assumed scenario, almost 70 % of the released Cesium is found to be associated with aerosols. The rest is present in vapor form.

The methodology applied here in order to determine the transient radiological release follows the recommendations proposed by Lorenz and Osborne [91]. The used fractional release rate model is called CORSOR-O. This easy to use stand-alone model is geometry independent. Its basis lies on the fission product release tests performed at the Oak Ridge National Laboratory between 1975 and 1993. In particular the tests carried out from 1981 on, the horizontal (HI) and the vertical induction heated (VI) test series, sponsored by the U.S. Nuclear Regulatory Commission (NRC) and performed under different atmospheres. These experiments provide information on relative release rates, chemical form and transport behavior for various fission products from high-burnup PWR and BWR fuel.

As described by Lorenz and Osborne [91], the fractional release rate model developed by Wichner and Lorenz [92] apply release rate coefficients, k (min^{-1}), which can be obtained from the test series mentioned above in order to represent the release rates of radioactive elements.

The fraction A of original inventory released in time t is defined as:

$$A = 1 - \exp(-ft). \quad (8.1)$$

The fractional release rate coefficient f can be calculated for each fission product with the following Arrhenius type expression:

$$f = f_0 \exp(-Q/RT), \quad (8.2)$$

with the species-dependent CORSOR-O release rate constant f_0 , the constant single-temperature activation energy $Q = 230$ kJ/mol, and the universal gas constant $R = 8.314$ J/mol K. The release rate constant for the highly volatile species Cesium and the noble gases Krypton and Xenon, possessing high vapor pressures, is determined as 12000 min^{-1} , assuming that the release is controlled by migration through the UO_2 . The release mechanism of fission products with low vapor pressure is, in contrast, slower and assumed to be controlled by vaporization. Depending on the system conditions, these species are also likely to recondense and thus might remain within the system. For all other species, a release rate multiplier R_f is applied. Its values, listed in Tab. 8-2, are chosen to fit the temperature dependent experimental data.

$$f_0 = R_f 12000 \text{ min}^{-1} \quad (8.3)$$

Tab. 8-2 Relative release rates [91].

Element	Multiplier R_f	Element	Multiplier R_f
Ag	0.4	Mo	0.25
Ba	0.2	Pu	0.00002
Ce	0.002	Ru	0.00004
Cs	1	Sb	0.5
Eu	0.1	Sr	0.1
I	0.8	Te	0.8
Kr	1	Xe	1
La	0.0002	Zr	0.0002

Using the inventory reduction method [91], equation (8.1) is applied for each period Δt , which yields the fraction of current inventory. The radioactive inventory A_0 must then be reduced by the amount released during the time step, according to:

$$A = A_0 (1 - \exp(-f\Delta t)). \quad (8.4)$$

8.3 Source Term

For the prediction of the in-containment source term, the inventory of fission products in the test section has been determined at KFKI Atomic Energy Research Institute, Budapest with the best-estimate in-house code TIBSO [83] for calculation of production and spreading of radioactive isotopes. Results are listed in Annex B. The underlying assumptions are a four-rod bundle with a total power of 64.5 kW and an irradiation time of 10^7 s (~115 days), which is 20 % longer than the envisaged test period. For the evaluation of the source term, the elements Kr, Sr, Zr, Mo, Ru, Ag, Sb, Te, I, Xe, Cs, Ba, La, Ce, Eu, and Pu are taken into respect, with 158 isotopes in total. For a number of important radioactive nuclides Tab. 8-3 lists their inventory for the SCWR-FQT test as it would arise 500 seconds after the reactor scram [80].

According to Eq. (8.4), the relative release rates from Tab. 8-2 are used in conjunction with the predicted fission product inventory of the four fuel rods to yield the in-containment accident source term in Bq as a function of time. For the calculations, the time interval Δt is chosen to be 20 s. Moreover, no consideration is given to a special treatment of early gap release from the fuel rods. In practice, this first release phase begins with the initiation of cladding failure and covers the release of the small fraction of fission products, which are resident in the fission gas plena and the gap between pellets and cladding during normal reactor operation. For example Kuhlman et al. [94] propose an immediate release of the volatile species Cs (5 % of initial inventory), I (1.7 %), and Kr and Xe (3 %) at 900 °C (corresponding to first cladding fractures), according to the gap release fraction estimates reported by Ritzman et al. [95]. However, it has to be kept in mind that the amount of gap inventory depends strongly on the fuel history, e.g. irradiation time and the type of accident. This phase lasts until the heat up of the fuel bulk leads to a considerably increased release of fission products in the so-called early in-vessel release phase, which is solely considered here. During this phase, significant quantities of volatile nuclides and also small amounts of less volatile species are no longer retained in the fuel matrix and released into the containment, as described by Soffer et al. [96]. Thus, the onset of fission product release into the experimental hall is assumed to be equal to the earliest failure of claddings, given by the material limit. Note that, due to the simple empirical model for fission product release used with CORSOR-O, its prediction capabilities are limited as discussed by Silberberg et al. [93] and Rest and Cronenberg [97]. This inaccuracy mainly results from the disregard of grain size and structural effects, such as fracturing of the UO₂ pellets.

Tab. 8-3 Half-life, radioactive inventory [80] at $t = 500$ s after the reactor scram and effective dose coefficients for inhalation [98] for selected important radioactive nuclides.

	Half life	Radioactive inventory [Bq]	Effective dose [Sv]
Iodine isotopes			
I 131	8.04 days	5.750E+13	2.0E-08
I 132	2.3 hours	8.145E+13	3.1E-10
I 133	20.8 hours	1.297E+14	4.0E-09
I 134	52.6 min.	1.352E+14	1.5E-10
I 135	6.61 hours	1.207E+14	9.2E-10
Noble gases			
Kr 85m	4.48 hours	3.272E+13	-
Kr 87	1.272 hours	4.510E+13	-
Kr 88	2.84 hours	6.532E+13	-
Xe 133	5.245 days	1.301E+14	-
Xe 135	9.09 hours	7.144E+13	-
Xe 137	3.818 min.	2.685E+13	-
Xe 138	14.17 min.	8.113E+13	-
Cesium isotopes			
Cs 137	30.02 years	9.234E+11	6.7E-09
Cs 138	32.2 min	1.093E+14	4.6E-11
Other fission products			
Sr 89	50.5 days	7.396E+13	5.6E-08
Mo 99	2.75 days	1.192E+14	1.1E-09
Te 132	3.258 days	8.446E+13	3.0E-09
Ba 140	12.74 days	1.212E+14	1.6E-09
Actinide isotopes			
Pu 239	24130 years	1.212E+09	3.2E-05
Pu 241	14.41 years	4.842E+09	8.4E-08

The next step is to transform the obtained activities to an effective dose, which is measured in Sv and allows assessing the radio-toxicity of the released material, using the BfS dose coefficients [98]. The radio-toxicity of a certain nuclide is determined by its effective dose coefficient (dose per unit intake), which accounts for radiation and tissue weighting factors. One assumption used to calculate the effective dose for inhalation in the experimental hall is that the complete released fission products infiltrate the room and that they distribute instantaneously and homogeneously throughout the free air volume. In fact, the in-containment source term is mitigated by removing fission products from the atmosphere. On one hand, this happens by natural processes such as deposition and sorption of vapors on surfaces. On the other hand, engineered safety features can be designated for this purpose. Feasible devices are suppression pools, containment sprays and filtration systems with particulate filters and adsorption beds made from charcoal. In terms of simplification, a reduction of

airborne material due to deposition on surfaces is not considered here. Moreover, removal of fission products by the installed filtration system or other features is not considered, which resembles to the accumulation of the total released radioactivity in the containment atmosphere.

The resulting effective dose D_E in Sv for a known activity intake I can be determined according to the guidelines for determination of body doses for internal radiation exposure subject to §§ 63 and 63A of the radiation protection ordinance documented chapter 3.42.1 of the Handbuch Reaktorsicherheit und Strahlenschutz [99]:

$$D_E = f_E I . \quad (8.5)$$

The isotope dependent dose coefficient f_E has been taken from BfS [98]. For a conservative evaluation of the theoretical radiation exposure of facility operators, the effective dose factors for internal occupational radiation exposure are applied. As incorporation type inhalation is assumed. No values are provided by BfS [98] for radioactive noble gases. After an accident, these gases are hard to contain as they are chemically inactive and in gases form at room temperature and thus will pass the filters. Hence, after breathing they will also not be retained or react with the human body. Thus, the health concern relates only to external radiation exposure. For this reason, the gases which remain inside the building after an accident with radioactive release have to be vented in advance of any kind of recovery actions.

Fig. 8-4 shows the in-containment source term for the isotope iodine-131, which results from the postulated beyond-design-basis accident. The release per time step ($\Delta t = 20$ s) is displayed graphically with blue bars. Due to peak fuel temperatures, most of the radioactive release is observed within the first 1000 seconds after the claddings have failed. As illustrated on the left hand side of Fig. 8-3, the residual power already decreased about 98 % to 1.4 kW within 1000 seconds after the scram. The cyan curve illustrates the integral released activity over time in Bq, as well as the converted effective dose in Sv. The total amount of released I-131 is $2.74 \cdot 10^{11}$ Bq, corresponding to 0.5 % of the initial inventory. After conversion, this comes up to an effective dose of 5480 Sv.

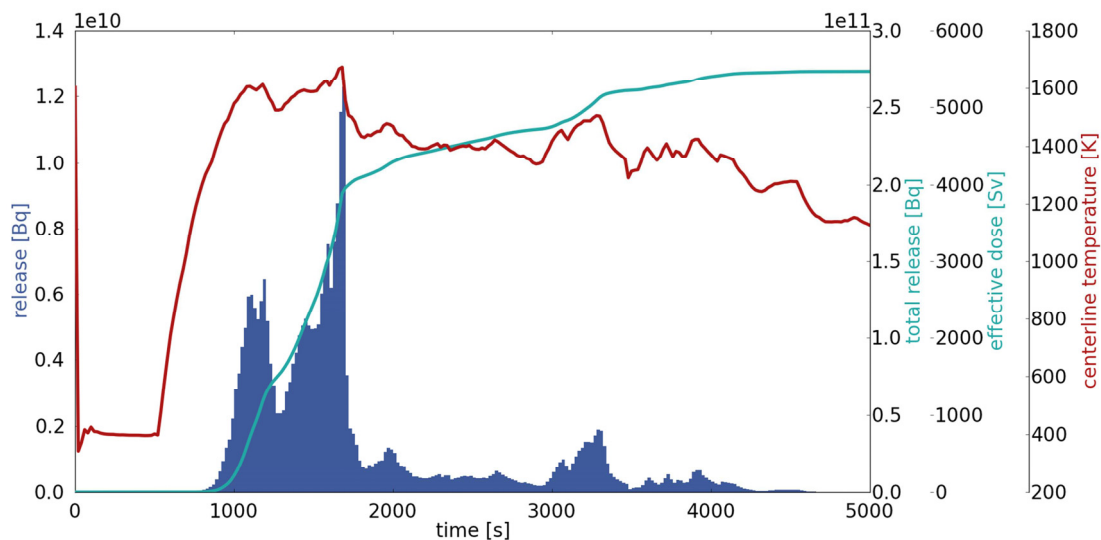


Fig. 8-4 Source term of iodine-131: fuel rod centerline temperature (red) and I-131 release per time step (blue), integral release with converted effective dose (both green).

Fig. 8-5 shows the release of isotopes, which together cover more than 99 % of the total released activity. The integral radiological release of all isotopes considered adds up to $9.02 \cdot 10^{12}$ Bq.

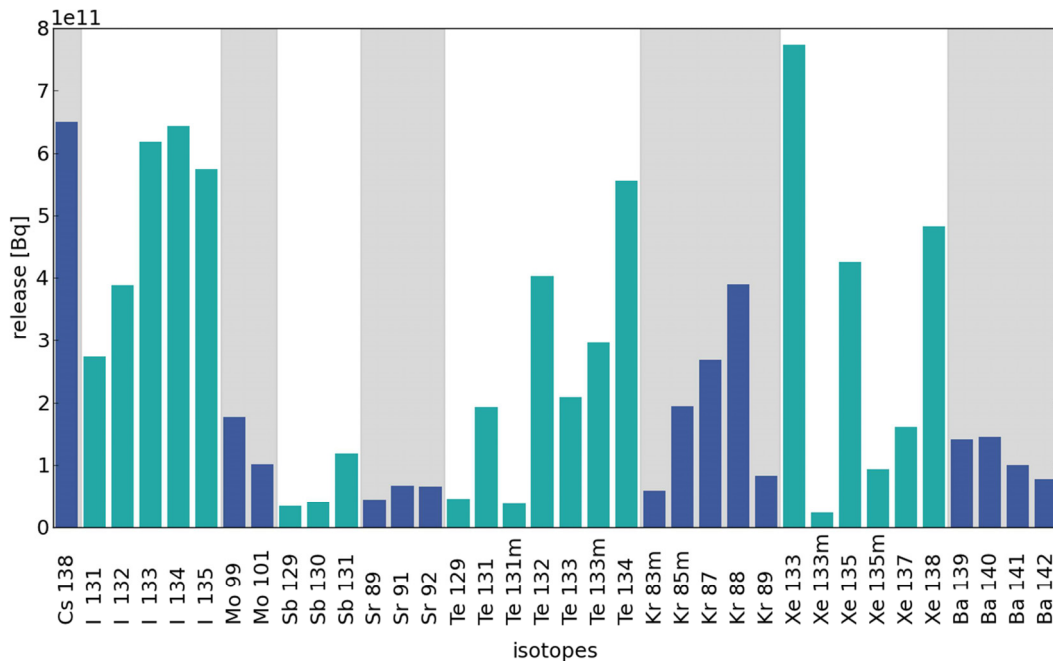


Fig. 8-5 Radioactive release of all isotopes contributing with more than $2 \cdot 10^{10}$ Bq. This covers 99 % of the total released activity.

Regarding health consequences from severe accidents, the radionuclides I, Cs, and Te are primary risk-dominant. The radioactive isotopes of iodine are both, gamma and beta emitters and key contributors to the dose received by an individual, not only from the radioactive cloud but also from deposition on surfaces. Especially iodine-131, which after ingestion concentrates in the thyroid gland, is due to its longest half life of eight days a major cause of nodules. After a severe accident, the ionizing radiation of cesium isotopes is a potential hazard for cancer. As resulting from the analysis, only cesium-138 with an amount of $6.51 \cdot 10^{11}$ Bq contributes greatly to the overall released activity, illustrated in Fig. 8-5. However, its effective dose of 30 Sv is of minor importance due to a relatively low conversion multiplier of only $4.6 \cdot 10^{-11}$ Sv/Bq (Fig. 8-6). Other important isotopes are tellurium-132 and barium-140, which could both be contributors to early doses and effects. The incorporation of strontium into bones may cause bone cancer and leukemia. After the conversion of the radioactive release illustrated in Fig. 8-5, the effective doses are obtained, as shown in Fig. 8-6:

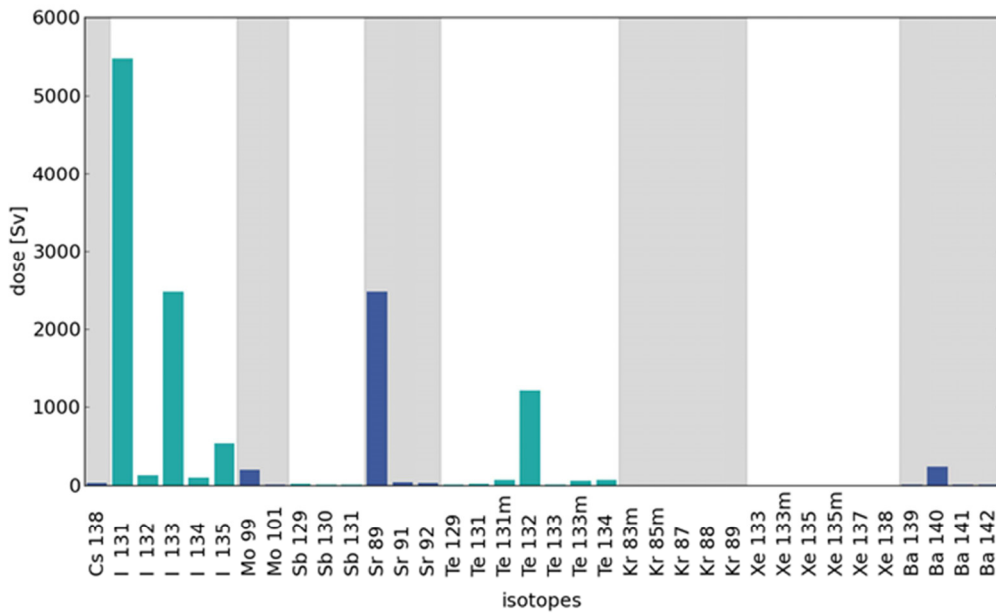


Fig. 8-6 Dose by isotope after conversion of released activity (Fig. 8-5) with effective dose coefficients.

The effective dose of all isotopes is 13324 Sv. For a better overview, Fig. 8-7 gives the contribution of twelve isotopes responsible for more than 97 % of the overall effective dose.

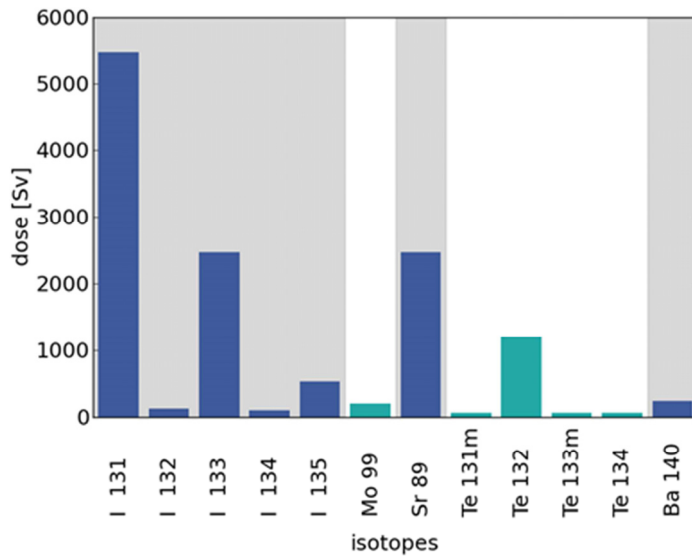


Fig. 8-7 Effective dose of all isotopes contributing with more than 50 Sv. This covers 97 % of the overall effective dose.

According to the NRC, the lethal dose (LD) is defined as the dose of radiation expected to cause death to 50 percent of an exposed population within 30 days (LD 50/30). Typically, this value is in the range of 4 to 5 Sv received over a very short period. Assuming a homogeneous distribution of the released radioactive material inside the 1762 m³ experimental hall, results in a dose of 7.56 Sv/m³.

Discussion

Fission product release rate estimates are performed for a postulated beyond-design-basis accident sequence: a large pipe break event in combination with a loss of power. Due to the relatively small water inventory of the test fuel element, the test section falls dry already seven minutes after the break. The subsequent heat up of the fuel causes the failure of the claddings. In principle, there are no more barriers left against radioactive release into the experimental hall. For the prediction of the generated in-containment source term, a homogenous distribution of radioactive material in the atmosphere of the experimental hall is assumed. Furthermore, an additional gap release of fission products, which escaped from the fuel matrix during operation, is not taken into respect. The integral released activity of all considered isotopes adds up to $9.02 \cdot 10^{12}$ Bq. After converting the released activity to the effective dose, the isotopes I-131, I-133, Sr-89, and Te-132 are found to be the main contributors to the source term in terms of potential health consequences to the operating personnel. In total, the effective dose sums up to 13324 Sv. This means a severe radiological contamination of the experimental hall, which in consequences may not be entered for a certain period of time until the radiation of short-lived isotopes has decayed. Therefore, a second, redundant set of emergency cooling systems with an independent power supply is recommended to exclude such situations.

9 Summary and Conclusions

The scope of the SCWR-FQT project is the development of the first nuclear test facility operated with supercritical water. This test will be of great benefit for the development of SCWR systems in many respects. It does not only represent a unique opportunity to gain operating experience with SCWR systems, but the envisioned test results will also be the high value for the validation of thermal-hydraulic and system codes. Furthermore, the performance of selected nuclear grade materials and reactor physics can be studied under realistic SCWR conditions. Finally, as the planned loop is a nuclear facility, its approval will serve as the test case for a general licensing approach of SCWRs.

As such an in-pile test always bears a certain hazardous potential, the system design process has been guided by a strategy of Defense in Depth with the basic tenet to protect the health and safety of the public and operational staff. This concept is implemented, inter alia, by the application of multiple physical barriers against radioactive release. Moreover, comprehensive safety systems are an important prerequisite in order to assure a safe execution of the intended experiments. These are two sets of combined active and passive emergency coolant injection systems for residual heat removal. Each of them consists of a bladder accumulator and a pump which is connected to an emergency reservoir. These systems are not redundant but cover different kinds of accidents. Being complemented by a depressurization system, this configuration allows bringing the system into a safe state in case of an accident. Uninterrupted power supply of the emergency systems in case of a black-out is secured by auxiliary batteries and a diesel generator.

In the present thesis, the commercial thermal-hydraulic code APROS has been applied to evaluate the performance and transient response of the intended safety systems under accidental conditions. A numerical model has been elaborated, which represents the test loop and all its safety-relevant equipment. As certain parts of the loop could not be modeled applying APROS standard components, alternative implementations with grouped basic modules have been developed.

The code has been validated against experiments regarding its ability to simulate distinguished flow phenomena with appropriate accuracy. The considered cases included a water hammer experiment conducted by Fujii and Akagawa [58] and a natural circulation loop investigated by Becker et al. [59] and Mathisen [60]. For both cases the numerical simulation results show good agreement with the experimental data. However, comparing results for another experiment has led to the identification of inadequacies: post-dryout conditions which may occur when crossing the critical point after depressurization from supercritical pressure conditions at full power, as described by Köhler and Hein [62], are not predicted correctly by the simulation. For this purpose, an independent analytical model has been developed using a quasi-steady-state approach [63], to predict maximum cladding temperatures and thus to compensate the deficit in the APROS code. Moreover, a code-to-code comparison with ATHLET confirmed a proper implementation of basic system specifications. Afterwards, the generated numerical model of the SCWR-FQT facility has been applied to support various design optimizations to withstand dynamic loads. For instance, it was found that a fast depressurization of the test section entails the risk of buckling collapse of the sensitive internals, caused by considerably high pressure differences across the thin-walled guide tubes. Thus, the speed of pressure drop has been attenuated by a reduction of the inlet and outlet cross sections in the fuel element head piece. An optimum value was found by a parametric study.

Finally, safety analyses for a list of anticipated design basis accidents have been conducted. These include a trip of the recirculation pump, a loss of heat sink, pipe ruptures and blockages at various locations, as well as coolant shortcuts inside the test fuel element.

The obtained simulation results, which are described in detail in Chapter 7, show that all assumed failures will be detected correctly by the optimized safety concept and the designated accident management measures will be taken. The general mitigating procedure starts with reactor scram being followed by depressurization of the primary loop. In case of intact pipe work, depressurization is accomplished by the automatic depressurization system, which leaves a grace time for the control rods to penetrate into the core and thus avoids a boiling crisis. Depressurization causes the test section to be quenched by two passive bladder accumulators for different kinds of accidents. Subsequently, two displacement pumps, fed from an emergency reservoir, are able to inject coolant via different flow lines and thus provide adequate residual heat removal. The simulations show that at least one of the barriers against radioactive release, i.e. the claddings or the primary circuit, remains intact. Thus, the safety systems are expected to perform as intended, mastering these postulated design basis accidents.

Additionally, a strategy for long-term residual heat removal has been worked out. In order to realize a closed emergency cooling circulation, coolant from the depressurization tank can be conducted to the emergency coolant reservoir by the use of a refilling pump. In a similar way, coolant which is collected in a sump has to be retransferred to the reservoir in case of a LOCA. A second independent heat sink can be established by flooding an air gap normally insulating the test fuel element from the reactor pool. In case the primary heat sink is lost, this passive feature alone is able to stabilize the coolant temperature inside the primary circuit. Cooling of the test section by purely passive heat conduction suffices twelve days after the reactor shutdown.

A beyond-design-basis accident analysis focused on the unlikely case of a simultaneous multi-component failure and its radiological consequences. The postulated scenario assumes a failure of the first three barriers. Only the final barrier against radioactive release, the hermetically sealed experimental hall equipped with a venting and filtration system, is assumed to stay intact. APROS simulations were performed to yield the worst case fuel center line temperatures for this scenario. For the duration of ~500 seconds, peak fuel temperatures of more than 1300 °C were reached. The predicted temperature distribution has then been used as input to an analysis of the source term for in-containment radioactivity release inside the experimental hall. For this purpose, the fractional release rate model CORSOR-O developed by Lorenz and Osborne [91] has been applied in an analysis considering 158 isotopes present after an assumed irradiation time of ~115 days, which is 20% longer than the envisaged test period. Finally, on the basis of the assumptions made, the integral radiological release adds up to $9 \cdot 10^{12}$ Bq. After conversion with the effective dose coefficients for inhalation, the total effective dose is 13000 Sv, with iodine-131 as the main contributor.

Although, the radioactive inventory of the test section is relatively small, the considerable release results from the fact that the water inventory of the test fuel element is very limited. In case of a pipe rupture and a simultaneous failure of the required emergency pump, this water would be evaporated already after 400 seconds. In that case, the fuel claddings would fail within a short period and no barrier preventing release into the experimental hall would be left. These findings clarify that even if the postulated scenario of a severe multi-component failure may possess a very low probability of occurrence, redundant and diverse pumps are highly recommended for both emergency systems to strictly avoid common-mode failures.

As a next step, the loop is planned to be constructed and tested out-of-pile with all safety systems, prior to its installation into the research reactor. In this framework, the thermal-hydraulic predictions made here will be validated against experimental data.

Nomenclature

Latin symbols

a_s	$m\ s^{-1}$	Sonic speed
A	m^2	Cross section
c_p	$J\ kg^{-1}\ ^\circ C^{-1}$	Specific heat capacity
C	-	Coefficient
d	m	Diameter
D_E	Sv	Effective dose
E	Pa	Young's modulus
f	-	Coefficient
f_E	$Sv\ Bq^{-1}$	Dose coefficient
F	-	Friction loss
g	$m\ s^{-2}$	Acceleration due to gravity
Gr	-	Grashof number
h	$J\ kg^{-1}$	Enthalpy
H	m	Height
I	Bq	Intake
k	$W\ m^{-2}\ ^\circ C^{-1}$	Heat transfer coefficient
k_{eff}	-	Effective multiplication factor
L	m	Length
L_{pe}	$kJ\ kg^{-1}$	latent heat of vaporization
m	kg	Mass
n	-	Number of lobes
Nu	-	Nusselt number
p	Pa	Pressure
P	W	Power
Pr	-	Prandtl number

Nomenclature

q	$W m^{-2}$	Heat flux
Q	W	Heat flow
Q	$kJ mol^{-1}$	Single-temperature activation energy
R	$J mol^{-1} K^{-1}$	Universal gas constant
R^2	-	Coefficient of determination
R_f	-	Release rate multiplier
$R_{p0.2}$	Pa	Yield strength
Re	-	Reynolds number
s	m	Thickness
S_b	-	Safety factor against buckling
t	s	Time
T	$^{\circ}C$	Temperature
u	$m s^{-1}$	Velocity
Y	-	Design value
z, Z	m	coordinate

Greek symbols

α	-	Void fraction
Γ	$kg m^{-3} s^{-1}$	Mass change rate
ε	m	Roughness
ν	-	Poisson's ratio
ρ	$kg m^{-3}$	Density

Subscripts

0	Initial
all	Allowable
b	Bulk
cr	Critical
dry	Dry
fl	Form loss

g	Gas
H	Hydraulic
i	Inner
i	Interface
k	Phase (liquid, gaseous)
l	Liquid
L	Leidenfrost
melt	Melting
n	Nominal
nb	Nucleate boiling
nc	Non-condensable gas
out	Outer
pc	Pseudo-critical
pu	Pump head
R	Reflection
sat	Saturation
sub	Sub-cooling
sp	Single-phase
va	Valve
w	Wall
wet	Wetted

References

- [1] The Generation IV International Forum. (2014, March) [Online]. <https://www.gen-4.org/>
- [2] U.S. DOE Nuclear Energy Research Advisory Committee and the Generation IV International Forum, "A Technology Roadmap for Generation IV Nuclear Energy Systems," 2002.
- [3] T. Schulenberg and J. Starflinger, *High Performance Light Water Reactor: Design and Analyses*. Karlsruhe: KIT Scientific Publishing, ISBN 978-3-86644-817-9, 2012.
- [4] J. Starflinger et al., "European Research Activities within the Project: 'High Performance Light Water Reactor Phase 2' (HPLWR Phase 2).," in *Proc. ICAPP '07*, Nice, France, May 13- 18, 2007.
- [5] D. Bittermann, D. Squarer, T. Schulenberg, and Y. Oka, "Economic Prospects of the HPLWR," in *GENES4/ANP2003*, Kyoto, Japan, 2003.
- [6] D. Bittermann, T. Schulenberg, and M. Andreani, "The safety concept of the HPLWR," in *Proc. ISSCWR4*, Heidelberg, Germany, March 8-11, 2009.
- [7] B. de Marsac, D. Bittermann, J. Starflinger, and T. Schulenberg, "Containment design proposal with active and passive safety systems for a high performance light water reactor," in *ISSCWR4*, Heidelberg, Germany, March 8-11, 2009.
- [8] T. Schulenberg, J. Starflinger, and J. Heinecke, "Three pass core design proposal for a high performance light water reactor," *Progress in Nuclear Energy*, vol. 50, pp. 526-531, 2008.
- [9] Y. Oka, S. Koshizuka, Y. Ishiwatari, and A. Yamaji, *Super Light Water Reactors and Super Fast Reactors - Supercritical-Pressure Light Water Cooled Reactors*, Springer, Ed., 2010.
- [10] X.J. Liu, T. Yang, and X. Cheng, "Core and sub-channel analysis of SCWR with mixed spectrum core," *Annals of Nuclear Energy*, vol. 37, no. 12, pp. 1674-1682, Dec. 2010.
- [11] L. Behnke, S. Himmel, C. Waata, E. Laurien, and T. Schulenberg, "Prediction of heat transfer for a supercritical water test with a four rod fuel bundle," in *Proc. ICAPP '06*, Reno, USA, June 4-8, 2006.
- [12] Generation IV International Forum, "Technology Roadmap Update for Generation IV Nuclear Energy Systems," 2014.
- [13] T. Schulenberg, "Material requirements of the high performance light water reactor," *The Journal of Supercritical Fluids*, vol. 77, pp. 127-133, 2013.
- [14] M. Ruzickova; T. Schulenberg; D.C. Visser; R. Novotny; A. Kiss; C. Maraczy; A. Toivonen, "Overview and progress in the European project 'Supercritical Water Reactor – Fuel Qualification Test'," *to be published in Progress in Nuclear Energy*, 2014.
- [15] Reactor Services Division, "Light Water Reactor LVR-15," Prague, Czech Republic, 1996.
- [16] M. Raqué, A. Vojacek, P. Hajek, and T. Schulenberg, "Design and 1D Analysis of the Safety Systems for the SCWR Fuel Qualification Test," in *Proc. NUTHOS-9*, Kaohsiung, Taiwan, September 9-13, 2012.
- [17] S. Himmel, A.G. Class, E. Laurien, and T. Schulenberg, "Determination of Mixing Coefficients in a Wire-Wrapped HPLWR Fuel Assembly using CFD," in *Proc. ICAPP '08*, Anaheim, USA, June 8-12, 2008.

- [18] T. Vágó, A. Kiss, and A. Aszódi, "Numerical Investigation on the Inlet and Outlet Effect of Heated Test Section of SCWR Fuel Qualification Test Design," in *Proc. NURETH-15*, Pisa, Italy, May 12-15, 2013.
- [19] J. Hofmeister, C. Waata, J. Starflinger, and T. Schulenberg, "Fuel assembly design study for a reactor with supercritical water," *Nuclear Engineering and Design*, vol. 237, pp. 1513-1521, 2007.
- [20] State Office for Nuclear Safety (SÚJB), "Requirements of the State Office for Nuclear Safety on Nuclear Research Facilities with Respect to Nuclear Safety, Radiation Protection, Physical Protection and Emergency Preparedness," Prague, Czech Republic, 2004.
- [21] State Office for Nuclear Safety (SÚJB), "Requirements on Nuclear Installations for Assurance of Nuclear Safety, Radiation Protection and Emergency Preparedness," Regulation No. 195/1999 Sb. 1999.
- [22] Risk and Safety Working Group, "An Integrated Safety Assessment Methodology (ISAM) for Generation IV Nuclear Systems," Version 1.1, 2011.
- [23] S. Penttilä and A. Toivonen, "Oxidation and SCC behaviour of austenitic and ODS steels in supercritical water," in *Proc. ISSCWR6*, Shenzhen, China, March 03-07, 2013.
- [24] S. Penttilä, A. Toivonen, J. Li, W. Zheng, and R. Novotny, "Effect of surface modification on the corrosion resistance of austenitic stainless steel 316L in supercritical water conditions," *The Journal of Supercritical Fluids*, no. 81, pp. 157-163, 2013.
- [25] M. Hänninen and J. Kurki, "Simulation of flows at supercritical pressures with a two-fluid code," in *Proc. NUTHOS-7*, Seoul, Korea, October 5-9, 2008.
- [26] M. Hänninen and J. Kurki, "Thermal-Hydraulic Simulation of Supercritical-Water-Cooled Reactors," in *Nuclear Power - System Simulations and Operation*, InTech, Ed.: Dr. Pavel Tsvetkov.
- [27] X.J. Liu, T. Yang, and X. Cheng, "Thermal-hydraulic analysis of flow blockage in a supercritical water-cooled fuel bundle with sub-channel code," *Annals of Nuclear Energy*, vol. 59, pp. 194-203, 2013.
- [28] T. Zeiger, M. Raqué, M. Kuznetsov, R. Redlinger, and T. Schulenberg, "Risk Analysis for a Radiolysis Gas Detonation in an Active Test Loop using Supercritical Water," in *Proc. NUTHOS-9*, Kaohsiung, Taiwan, September 9-13, 2012.
- [29] T. Schulenberg; X. Cheng; X.J. Liu; C. Zhou; M. Raqué; T. Zeiger, "Deliverable E3.3, Analyses of Design Basis Accidents, Project SCWR-FQT," Contract Number: 269908, 2014.
- [30] R. Novotny; P. Hähner; J. Siegl; P. Haušild; S. Ripplinger; S. Penttilä; A. Toivonen, "Stress corrosion cracking susceptibility of austenitic stainless steels in supercritical water conditions," *Journal of Nuclear Materials*, no. 409, pp. 117-123, 2011.
- [31] The American Society of Mechanical Engineers, *ASME Boiler and Pressure Vessel Code, Section III, Division I*. New York, 2004.
- [32] A. Vojáček and G. Mazzini, "Analyses of the start-up and shut-down of SCWR fuel qualification test loop with ATHLET code," *Bezpečnost' jaderné energie*, vol. 21, no. 59, pp. 289-294, 2013.
- [33] T. Schulenberg, A. Vojacek, T. Zeiger, and M. Raqué, "Risks and safety analyses of an SCWR fuel qualification test loop," in *Proc. ISSCWR6*, Shenzhen, China, March 03-07, 2013.

- [34] T. Schulenberg, M. Raqué, and K. Arheidt, "Prediction of heat transfer during depressurization from supercritical pressure," in *Proc. NURETH-15*, Pisa, Italy, May 12-17, 2013.
- [35] VTT Finland and Fortum. (2014, Feb.) APROS - Process Simulation Software. [Online]. <http://APROS.vtt.fi/>
- [36] K. Porkholm, H. Kontio, H. Plit, M. Mustonen, and K. Söderholm, "APROS Simulation Model for Olkiluoto-3 EPR Applications," in *Proc. TOPSAFE*, Dubrovnik, Croatia, Sept. 30 - Oct. 03, 2008.
- [37] W. Wagner; J.R Cooper; A. Dittmann; J. Kijima; H.-J. Kretzschmar; A. Kruse; R. Mareš; K. Oguchi; H. Sato; I. Stöcker; O. Šifner; Y. Takaishi; I. Tanishita; J. Trübenbach; Th. Willkommen, "The IAPWS Industrial Formulation 1997 for the Thermodynamic Properties of Water and Steam," *Journal of Engineering for Gas Turbines and Power*, vol. 122, pp. 150-182, 2000.
- [38] J. Kurki, "Simulation of thermal hydraulics at supercritical pressures with APROS," Helsinki University of Technology, Department of Engineering Physics and Mathematics, Thesis for the degree of Master of Science in Technology, 2008.
- [39] M. Schlagenhauser, "Simulation des Dampf-Wasserkreislaufs und der Sicherheitssysteme eines High Performance Light Water Reactors," Karlsruhe Institute of Technology, Dissertation 2010.
- [40] M. Hänninen and J. Ylijoki, "The constitutive equations of the APROS six-equation model," VTT Finland and Fortum, APROS Version 5.09, 2007.
- [41] M. Hänninen, "Phenomenological extensions to APROS six-equation model: non-condensable gas, supercritical pressure, improved CCFL and reduced numerical diffusion for scalar transport calculation," VTT Technical Research Centre of Finland, VTT Publications 720, 2009.
- [42] T. Siikonen, "Numerical Method for One-Dimensional Two-Phase Flow," *Numerical Heat Transfer*, vol. 12, pp. 1-18, 1987.
- [43] D. Bestion, "The physical closure laws in the CATHARE code," *Nuclear Engineering and Design*, vol. 124, no. 3, pp. 229-245, 1990.
- [44] J. Luukka, "Improving the calculation of rate of stratification in APROS," Lappeenranta University of Technology, Faculty of Technology, Master Thesis, 2010.
- [45] N.I. Kolev, *Multiphase Flow Dynamics 2: Thermal and Mechanical Interactions*. Berlin: Springer-Verlag, 2002.
- [46] VDI-Gesellschaft Verfahrenstechnik und Chemieingenieurwesen, Ed., *VDI Wärmeatlas*, 10th ed. Berlin Heidelberg New York: Springer Verlag, 2006.
- [47] R.W. Lockhart and R.C. Martinelli, "Proposed Correlation of Data for Isothermal Two-phase, Two-component Flow in Pipes," *Chemical Engineering Progress*, vol. 45, no. 1, pp. 39-48, 1949.
- [48] I. Pioro, R. Duffy, and T. Dumouchel, "Hydraulic resistance of fluid flowing in channels at supercritical pressures (survey)," *Nuclear Engineering and Design*, vol. 231, pp. 187-197, 2004.
- [49] J. Knudsen and D. Katz, *Fluid Dynamics and Heat Transfer*, McGraw-Hill Book Company, Ed. New York, 1958.
- [50] D.C. Groeneveld and C.W. Snoek, "A comprehensive examination of heat transfer correlations suitable for reactor safety analysis," *Multiphase Science and Technology*, vol. 2, pp. 181-274, 1986.
- [51] P.J. Berenson, "Film-Boiling Heat Transfer From a Horizontal Surface," *Journal of Heat Transfer*, vol. 83, pp. 351-358, August 1961.

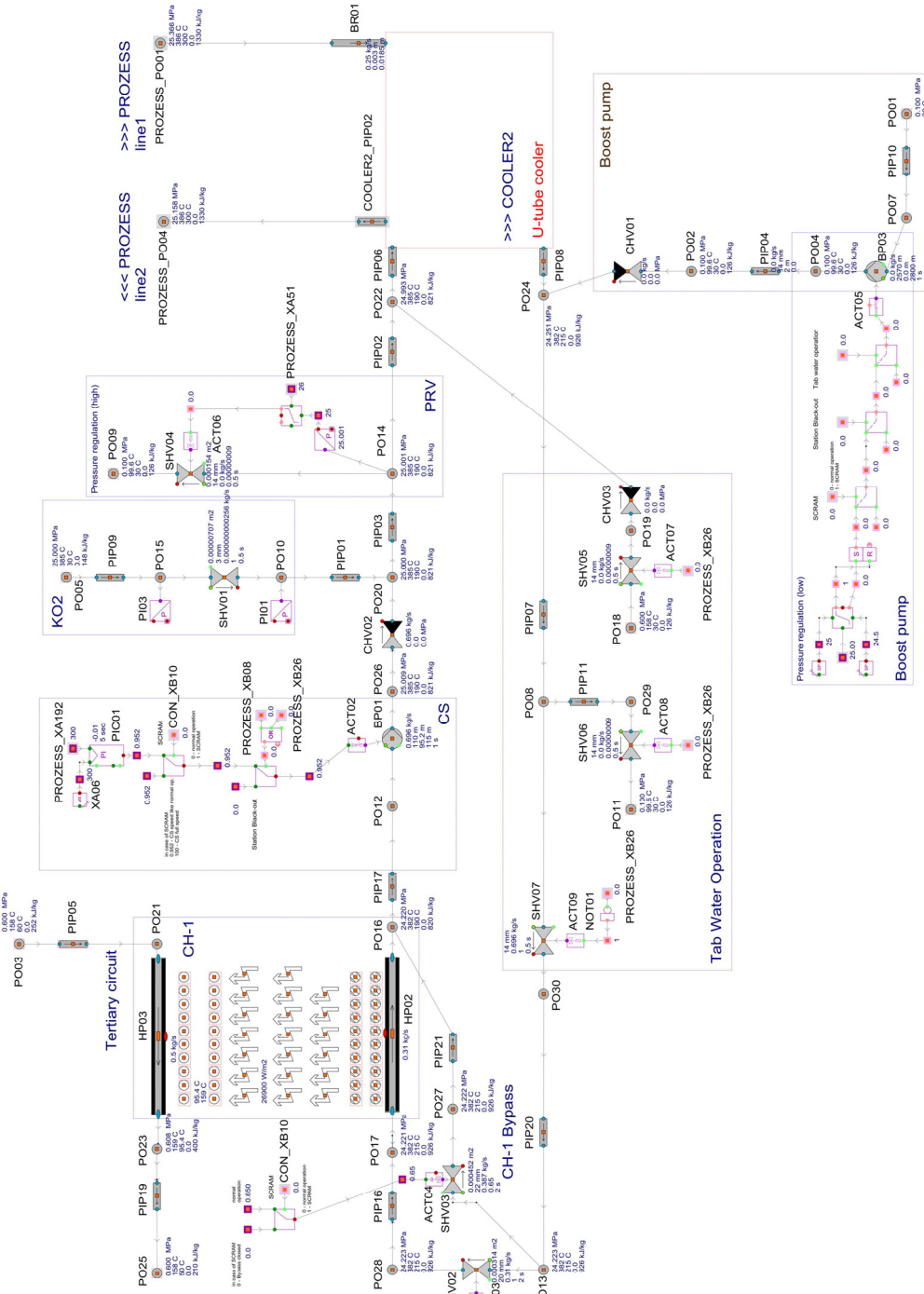
- [52] M. Hänninen, E. Puska, J. Miettinen, and J. Ylijoki, "Homogeneous Two Phase Flow Model of APROS," Finland, Version 2.2, 1991.
- [53] J. Kurki, "Simulation of thermal hydraulic at supercritical pressures with APROS," in *Proc. IYNC 2008*, Interlaken, Switzerland, September 20-26, 2008.
- [54] J.D. Jackson and W.B. Hall, "Forced convection heat transfer to fluids at supercritical pressure," in *Turbulent Forced Convection in Channels and Bundles, Vol. 2*. Hemisphere, New York, 1979, pp. 563-611.
- [55] I. Kokkonen, "Air/water countercurrent flow limitation experiments with full-scale fuel bundle structures," *Experimental Thermal and Fluid Science*, vol. 3, pp. 581-587, 1990.
- [56] F. Moody, "Maximum flow rate of a single component, two-phase mixture," *Transactions of ASME, Journal of Heat Transfer*, vol. 86, pp. 134-142, 1965.
- [57] M. Hänninen and E. Ahtinen, "Simulation of non-condensable gas flow in two-fluid model of APROS – Description of the model, validation and application," *Annals of Nuclear Energy*, vol. 36, pp. 1588-1596, 2009.
- [58] T. Fujii and K. Akagawa, "Water Hammer Phenomena in a One-Component Two-Phase Bubbly Flow," *Nuclear Engineering and Design*, vol. 141, pp. 101-110, 1993.
- [59] K.M. Becker, R.P. Mathisen, O. Eklind, and B. Norman, "Measurements of Hydrodynamic Instabilities, Flow Oscillations and Burnout in a Natural Circulation Loop," Aktiebolaget Atomenergi, AE-131, Stockholm, Sweden, 1964.
- [60] R.P. Mathisen, "Out of pile channel instability in the loop Skälvan," in *Proc. Symp. on Two Phase Flow Dynamics*, Eindhoven, 1967, pp. 19-64.
- [61] M. Raqué, H. Herbell, and T. Schulenberg, "Validation of the System Code APROS for Fast Transients," in *Proc. ICONE21*, Chengdu, China, July 29 - August 02, 2013.
- [62] W. Köhler and D. Hein, "Influence of the Wetting State of a Heated Surface on Heat Transfer and Pressure Loss in an Evaporator Tube," Kraftwerk Union AG, Erlangen, NUREG/IA-0003, 1986.
- [63] T. Schulenberg and M. Raqué, "Transient heat transfer during depressurization from supercritical pressure," *to be published in Int. Jnl. of Heat and Mass Transfer*, 2014.
- [64] J.P. Tullis, *Hydraulics of Pipelines – Pumps, Valves, Cavitation, Transients*, John Wiley and Sons, Ed. New York, 1989.
- [65] N. Joukowsky, *Über den hydraulischen Stoß in Wasserleitungsrohren*, Voß, Ed. Petersburg und Leipzig, 1900.
- [66] H. Herbell, "Thermohydraulische Auslegung des Zwischenüberhitzers eines High Performance Light Water Reactors," Karlsruhe Institut of Technology, Dissertation, 2011.
- [67] M. Raqué, O. Frybort, A. Vojacek, and T. Schulenberg, "Passive Residual Heat Removal System for the SCWR Fuel Qualification Test Facility," in *Proc. NURETH-15*, Pisa, Italy, May 12-17, 2013.
- [68] I.E. Idelchik, *Handbook of Hydraulic Resistance, Revised and Augmented*, 2nd ed. Berlin: Springer-Verlag, 1986.
- [69] B. Szygalski, "Modellierung des transienten Wärmeübergangs bei Sieden nahe dem kritischen Punkt," Karlsruhe Institut of Technology, Institute for Nuclear and Energy Technologies, Diploma Thesis, 2012.
- [70] X. Cheng, Y.H. Yang, and S.F. Huang, "A simplified method for heat transfer prediction of supercritical fluids in circular tubes," *Ann. Nucl. Energy*, vol. 36, pp. 1120–1128, 2009.

- [71] W. Rohsenow, *Modern Developments in Heat Transfer*. New York: Academic Press, 1963.
- [72] D.C. Groeneveld and C.G.J. Delorme, "Prediction of thermal non-equilibrium in the post-dryout regime," *Nucl. Eng. Design*, vol. 36, pp. 17-26, 1976.
- [73] G. Lerchel and H. Austregesilo, ATHLET Mod 2.1 Cycle A, User's Manual, GRS-p-1/Vol.1, Rev.4., 2006.
- [74] C. Zhou, Y. Yang, and X. Cheng, "Feasibility analysis of the modified ATHLET code for supercritical water cooled systems," *Nuclear Engineering and Design*, vol. 250, pp. 600-612, 2012.
- [75] A.A. Bishop, R.O. Sandberg, and T.S. Tong, "Forced convection heat transfer to water nearcritical temperatures and super-critical pressures," *A.I.Ch.E.-I.Chem.E. Symposium Series*, vol. 2, pp. 77-85, 1965.
- [76] C. Zhou, Y. Yang, and X. Cheng, "Loss of Coolant Flow Accident Analysis of the Supercritical Water-cooled Reactor Fuel Qualification Test Loop," in *Proc. ISSCWR6*, Shenzhen, China, March 03-07, 2013.
- [77] T. Schulenberg; M. Raqué; C. Zhou; T. Zeiger, "Deliverable E3.1, WP3 Interim report after year 1, Project SCWR-FQT," Contract Number: 269908, 2012.
- [78] G. Zhang, H. Zhang, H. Gu, Y. Yang, and X. Cheng, "Experimental and numerical investigation of turbulent convective heat transfer deterioration of supercritical water in vertical tube," *Nuclear Engineering and Design*, vol. 248, pp. 226-237, 2012.
- [79] R. Schneider, M. Schlagenhauser, and T. Schulenberg, "Conceptual Design of the Safety System for a SCWR Fuel Qualification Test," in *Proc. NUTHOS-8*, Shanghai, China, October 10-14, 2010.
- [80] Á. Brolly; G. Hegyi; G. Hordósy; C. Maráczy; P. Vértes; O. Frybort; P. Dostal; A. Vojacek; J. Soltes, "Deliverable E2.5, WP2 Analyses of normal operation - Final report on neutronic analyses, Project SCWR-FQT," Contract Number: 269908, 2014.
- [81] F. Brown, MCNP - a general Monte Carlo n-particle transport code, Version 5, Los Alamos National Laboratory, LA-UR-03-1987, 2003.
- [82] M. Raqué, I. Vasari, and T. Schulenberg, "Safety Analyses for a SCWR In-pile Fuel Assembly Test," in *Proc. NURETH-14*, Toronto, Canada, Sept. 25-30, 2011.
- [83] KFKI Atomic Energy Research Institute. [Online]. <http://www.kfki.hu/~vertes/tibso/tbabst.html>
- [84] G. Rudstam, "Uncertainty of decay heat calculations originating from errors in the nuclear data and the yields of individual fission products," *Journal of Radioanalytical Chemistry*, vol. 55, no. 1, pp. 79-99, 1980.
- [85] M. Raqué and T. Schulenberg, "Optimization of the SCWR Fuel Qualification Test for fast Depressurization Transients," in *Proc. ISSCWR6*, Shenzhen, China, March 03-07, 2013.
- [86] P. Kremers, "Strukturmechanische Analyse eines Versuchsbrennelements für einen Reaktor mit überkritischem Wasser," Karlsruhe Institut of Technology, Institute for Nuclear and Energy Technologies, Diploma Thesis, 2009.
- [87] Kerntechnischer Ausschuss (KTA), "Safety Standards of the Nuclear Safety Standards Commission KTA, 3201.2 Components of the Reactor Coolant Pressure Boundary of Light Water Reactors Part 2: Design and Analysis," 6/96.
- [88] K. Almenas, A. Kaliatka, and E. Uspuras, *Ignalina RBMK-1500 – A Source Book*, Ignalina Safety Analysis Group, Ed. Lithuania: Lithuanian Energy Institute, 1998.

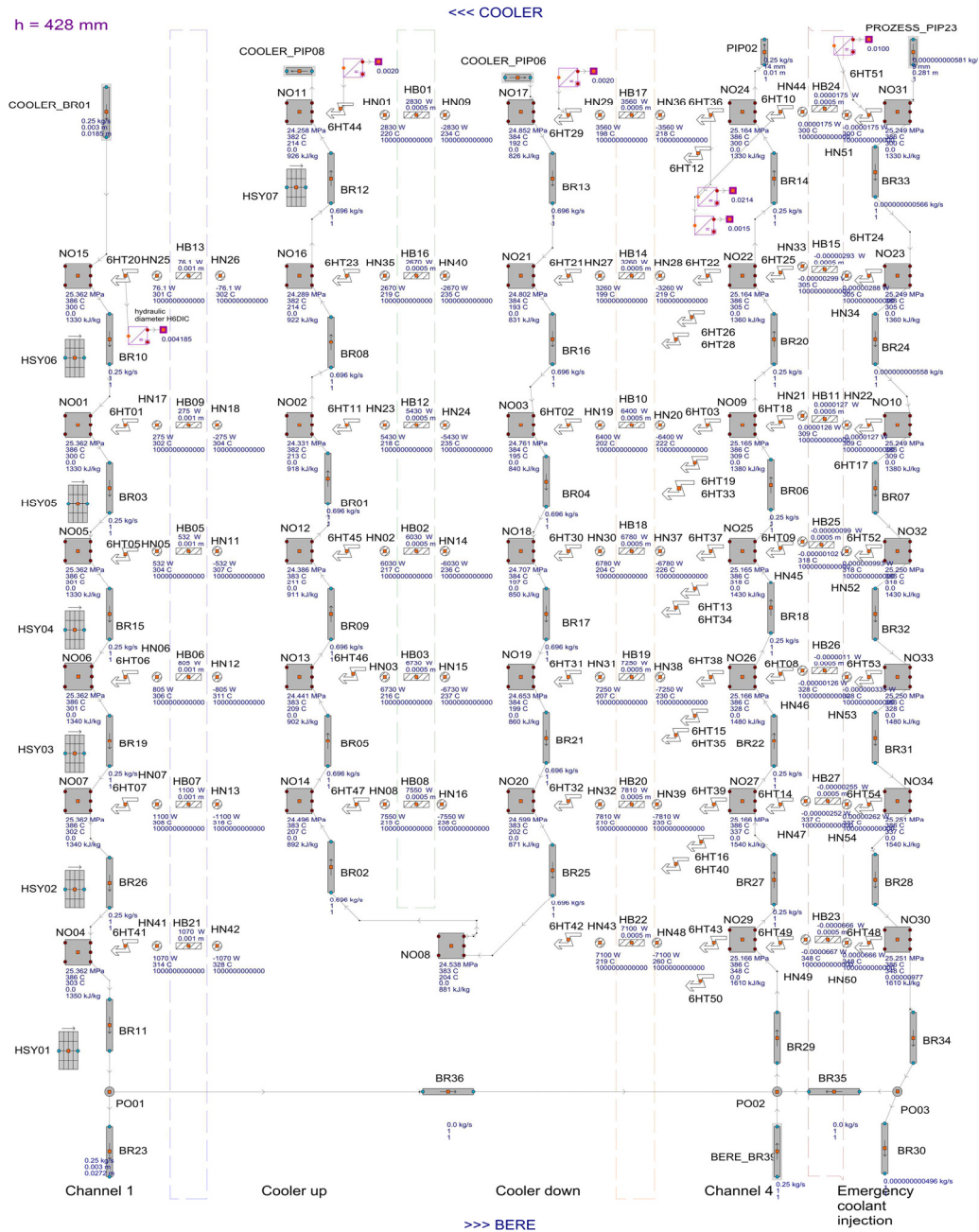
References

- [89] T. Zeiger, M. Raqué, and T. Schulenberg, "Study of consequences of a pressure tube failure for an SCWR in-pile fuel assembly test," in *Proc. NURETH-15*, Pisa, Italy, May 12-17, 2013.
- [90] T. Zeiger, T. Schulenberg, M. Flad, and M. Raqué, "Indirect consequences of pressure tube rupture during SCWR fuel qualification test," in *Proc. PBNC 2014*, Vancouver, Canada, August 24-28, 2014.
- [91] R.A. Lorenz and M.F. Osborne, "A summary of ORNL fission product release tests with recommended release rates and diffusion coefficients," Oak Ridge National Laboratory, NUREG/CR-6261, 1995.
- [92] R.P. Wichner and R.A. Lorenz, "Technical bases for estimating fission product behavior during LWR accidents," U.S. Nuclear Regulatory Commission, Washington, D.C., NUREG-0772, 1981.
- [93] M. Silberberg, J.A. Mitchell, R.O. Meyer, and C.P. Ryder, "Reassessment of the Technical Bases for Estimating Source Terms," U.S. Nuclear Regulatory Commission, Washington, D.C., NUREG-0956, 1986.
- [94] M.R. Kuhlman, D.J. Lehmicke, and R.O. Meyer, "CORSOR User's Manual," Battelle's Columbus Laboratories, NUREG/CR-4173 (BMI-2122), 1985.
- [95] R.L. Ritzman; E.F. Aber; C. Alexander; M.H. Fontana; D.K. Landstrom; D.L. Lessor; H.L. McMurry; D.L. Morrison; P.C. Owzarski; G.W. Parker; L.F. Parsly; M. Pobereskin; A.K. Postma; H.S. Rosenberg; W.A. Yuill, "Release of Radioactivity in Reactor Accidents, Appendix VII to Reactor Safety Study," U.S. Nuclear Regulatory Commission, Washington, D.C., WASH-1400 (NUREG-75/014), 1975.
- [96] L. Soffer, S.B. Burson, C.M. Ferrell, R.Y. Lee, and J.N. Ridgely, "Accident Source Terms for Light-Water Nuclear Power Plants," U.S. Nuclear Regulatory Commission, Washington, D.C., NUREG-1465, 1995.
- [97] J. Rest and A.W. Cronenberg, "Modeling the behavior of Xe, I, Cs, Te, Ba, and Sr in solid and liquified fuel during severe accidents," *Journal of Nuclear Materials*, no. 150, pp. 203-225, 1987.
- [98] Federal Office for Radiation Protection of Germany (BfS), "Dose coefficients to calculate radiation exposure," *Bundesanzeiger*, no. 160a and 160b, August 2001.
- [99] Der Bundesminister des Innern, *Handbuch Reaktorsicherheit und Strahlenschutz*. Köln, Germany: Gesellschaft für Reaktorsicherheit (GRS) mbH, 1997.

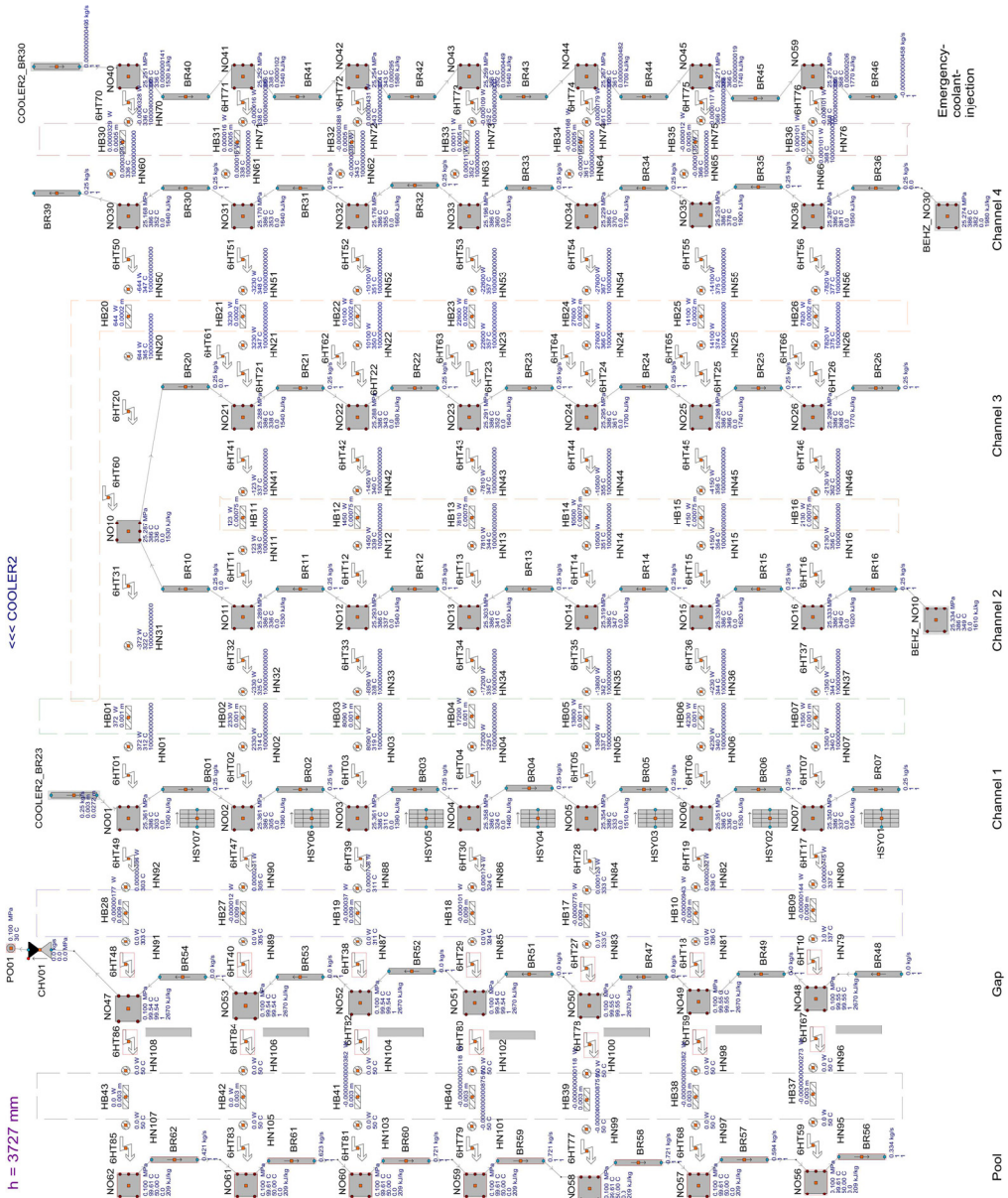
Secondary Loop - net ID: COOLER



Cooler FE - net ID: COOLER2

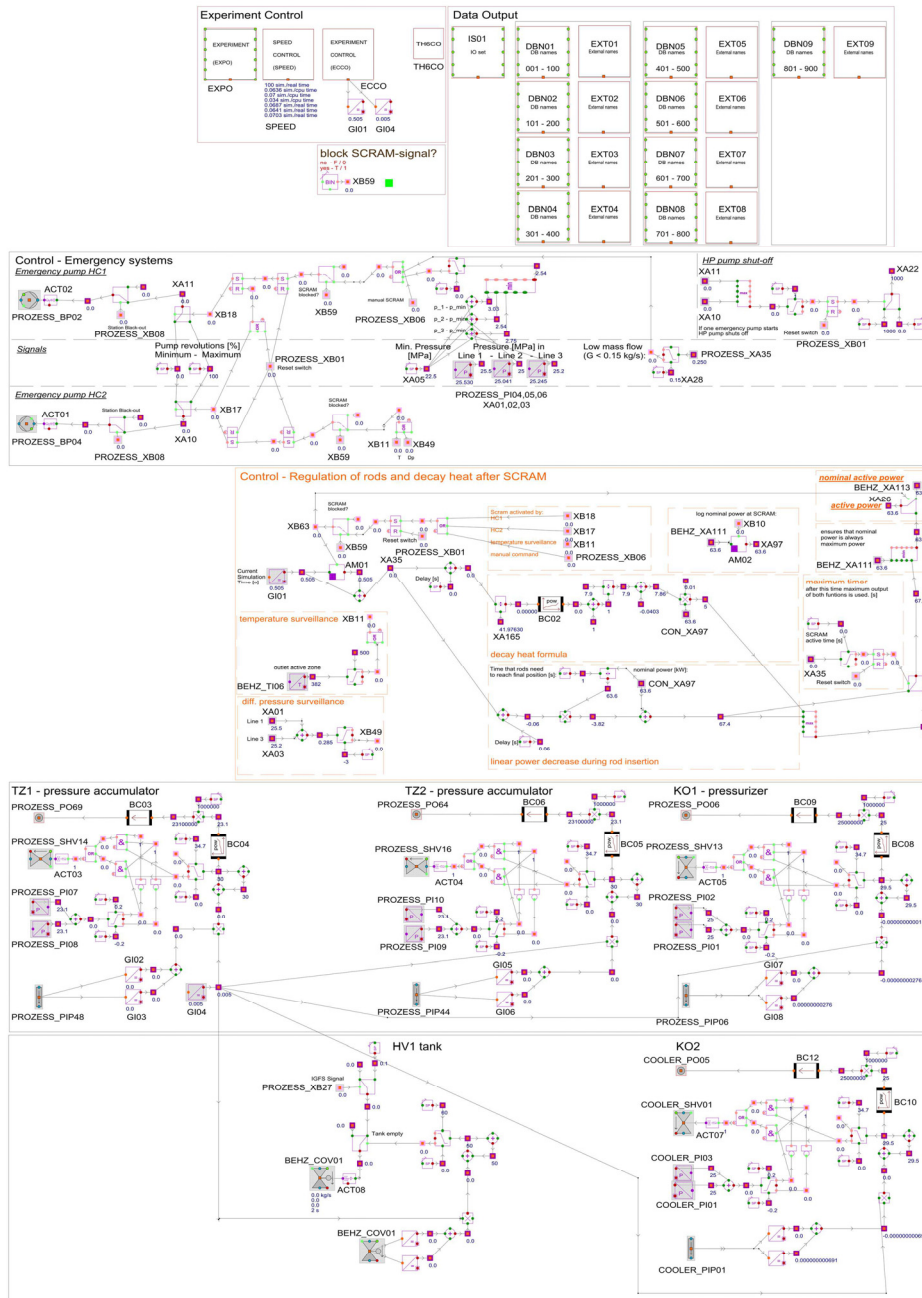


Recuperator FE - net ID: BERE



Annex A

Control Window - net ID: CON



Annex B

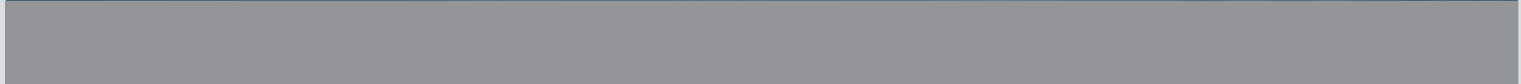
Nuclide inventory of the fuel after 10^7 s (~115 days) exposure at full load operation plus 500 seconds of decay [80].

isotope	type	half-life		activity [Bq]
94-Pu-236	0	2.90E+00	year	2.41E-05
94-Pu-237	0	4.53E+01	day	7.68E+00
94-Pu-238	0	8.78E+01	year	3.78E+07
94-Pu-239	0	2.41E+04	year	1.21E+09
94-Pu-240	0	6.57E+03	year	1.52E+08
94-Pu-241	0	1.44E+01	year	4.84E+09
94-Pu-242	0	3.74E+05	year	2.10E+03
94-Pu-243	0	4.96E+00	hour	1.08E+08
94-Pu-244	0	8.01E+07	year	2.24E-06
94-Pu-245	0	1.05E+01	hour	9.20E-01
94-Pu-246	0	1.09E+01	day	4.86E-05
36-Kr-079	0	1.46E+00	day	6.01E+00
36-Kr-081	0	2.10E+05	year	5.82E-02
36-Kr-081	1	1.30E+01	sec	3.25E-08
38-Sr-083	0	1.35E+00	day	5.96E-01
36-Kr-083	1	1.83E+00	hour	9.88E+12
36-Kr-085	0	1.07E+01	year	1.58E+11
38-Sr-085	0	6.48E+01	day	9.16E+05
36-Kr-085	1	4.48E+00	hour	3.27E+13
38-Sr-085	1	1.13E+00	hour	2.38E+03
36-Kr-087	0	1.27E+00	hour	4.51E+13
38-Sr-087	1	2.81E+00	hour	5.33E+06
36-Kr-088	0	2.84E+00	hour	6.53E+13
40-Zr-088	0	8.34E+01	day	2.65E+00
36-Kr-089	0	3.17E+00	min	1.40E+13
38-Sr-089	0	5.05E+01	day	7.40E+13
40-Zr-089	0	3.27E+00	day	3.87E+02
36-Kr-090	0	3.23E+01	sec	2.11E+09
38-Sr-090	0	2.91E+01	year	8.75E+11
36-Kr-091	0	8.57E+00	sec	1.77E-04
38-Sr-091	0	9.52E+00	hour	1.12E+14
36-Kr-092	0	1.85E+00	sec	0.00E+00
38-Sr-092	0	2.71E+00	hour	1.10E+14
36-Kr-093	0	1.29E+00	sec	0.00E+00
40-Zr-093	0	1.53E+06	year	1.77E+07
42-Mo-093	0	3.50E+03	year	7.63E-04
42-Mo-093	1	6.85E+00	hour	6.64E+00

36-Kr-095	0	7.80E-01	sec	0.00E+00
40-Zr-095	0	6.40E+01	day	9.26E+13
40-Zr-097	0	1.69E+01	hour	1.16E+14
44-Ru-097	0	2.90E+00	day	2.50E-01
42-Mo-099	0	2.75E+00	day	1.19E+14
42-Mo-101	0	1.46E+01	min	6.80E+13
44-Ru-103	0	3.94E+01	day	5.31E+13
47-Ag-103	0	1.09E+00	hour	1.97E-04
44-Ru-105	0	4.44E+00	hour	2.36E+13
47-Ag-105	0	4.13E+01	day	5.34E-01
44-Ru-106	0	1.01E+00	year	1.70E+12
47-Ag-106	0	2.40E+01	min	4.79E+00
47-Ag-106	1	8.46E+00	day	2.38E+01
47-Ag-108	1	4.18E+02	year	1.63E+00
47-Ag-110	1	2.50E+02	day	3.00E+08
47-Ag-111	0	7.45E+00	day	4.65E+11
47-Ag-112	0	3.14E+00	hour	3.36E+11
47-Ag-115	0	2.00E+01	min	1.65E+11
51-Sb-115	0	3.21E+01	min	1.09E-03
51-Sb-117	0	2.80E+00	hour	1.16E+00
51-Sb-118	0	3.60E+00	min	1.76E+00
51-Sb-119	0	1.59E+00	day	9.62E+02
51-Sb-120	0	1.59E+01	min	5.79E+03
51-Sb-120	1	5.76E+00	day	1.67E+04
52-Te-121	0	1.68E+01	day	8.36E+01
53-I-121	0	2.12E+00	hour	8.93E-03
52-Te-121	1	1.54E+02	day	2.16E+01
51-Sb-122	0	2.70E+00	day	3.36E+09
52-Te-123	0	1.00E+13	year	5.67E-08
53-I-123	0	1.32E+01	hour	3.40E+01
52-Te-123	1	1.20E+02	day	5.93E+05
51-Sb-124	0	6.02E+01	day	1.26E+09
51-Sb-124	2	2.02E+01	min	2.45E+08
51-Sb-125	0	2.73E+00	year	5.72E+10
53-I-125	0	6.01E+01	day	3.43E+03
54-Xe-125	0	1.70E+01	hour	1.45E+00
52-Te-125	1	5.80E+01	day	5.91E+09
54-Xe-125	1	5.70E+01	sec	1.68E-03
51-Sb-126	0	1.24E+01	day	1.56E+10
53-I-126	0	1.30E+01	day	1.01E+05
51-Sb-126	1	1.90E+01	min	1.14E+10
51-Sb-127	0	3.85E+00	day	3.47E+12
52-Te-127	0	9.35E+00	hour	3.13E+12
54-Xe-127	0	3.64E+01	day	5.46E+02

55-Cs-127	0	6.25E+00	hour	3.53E-02
52-Te-127	1	1.09E+02	day	3.06E+11
54-Xe-127	1	1.17E+00	min	2.27E+00
51-Sb-128	0	9.01E+00	hour	4.53E+11
53-I-128	0	2.50E+01	min	1.34E+10
51-Sb-128	1	1.04E+01	min	4.01E+12
51-Sb-129	0	4.40E+00	hour	1.11E+13
52-Te-129	0	1.16E+00	hour	9.69E+12
53-I-129	0	1.57E+07	year	1.50E+05
55-Cs-129	0	1.34E+00	day	2.39E+01
52-Te-129	1	3.36E+01	day	1.88E+12
54-Xe-129	1	8.89E+00	day	5.21E+04
51-Sb-130	0	4.00E+01	min	1.33E+13
53-I-130	0	1.24E+01	hour	3.33E+10
51-Sb-131	0	2.30E+01	min	3.95E+13
52-Te-131	0	2.50E+01	min	4.05E+13
53-I-131	0	8.04E+00	day	5.75E+13
55-Cs-131	0	9.69E+00	day	2.22E+04
56-Ba-131	0	1.18E+01	day	3.10E+00
52-Te-131	1	1.25E+00	day	8.05E+12
54-Xe-131	1	1.19E+01	day	6.27E+11
52-Te-132	0	3.26E+00	day	8.45E+13
53-I-132	0	2.30E+00	hour	8.15E+13
55-Cs-132	0	6.48E+00	day	2.08E+06
53-I-132	1	1.39E+00	hour	1.81E+11
52-Te-133	0	1.25E+01	min	4.39E+13
53-I-133	0	2.08E+01	hour	1.30E+14
54-Xe-133	0	5.25E+00	day	1.30E+14
56-Ba-133	0	1.05E+01	year	2.16E+02
52-Te-133	1	5.54E+01	min	6.20E+13
54-Xe-133	1	2.19E+00	day	3.80E+12
52-Te-134	0	4.18E+01	min	1.17E+14
53-I-134	0	5.26E+01	min	1.35E+14
55-Cs-134	0	2.06E+00	year	6.61E+10
55-Cs-134	1	2.90E+00	hour	1.94E+08
53-I-135	0	6.61E+00	hour	1.21E+14
54-Xe-135	0	9.09E+00	hour	7.14E+13
55-Cs-135	0	2.30E+06	year	7.02E+06
57-La-135	0	1.95E+01	hour	2.76E+03
54-Xe-135	1	1.57E+01	min	1.56E+13
55-Cs-135	1	5.30E+01	min	5.31E+09
56-Ba-135	1	1.20E+00	day	4.20E+06
55-Cs-136	0	1.32E+01	day	2.71E+11
54-Xe-137	0	3.82E+00	min	2.69E+13

55-Cs-137	0	3.00E+01	year	9.23E+11
57-La-137	0	6.00E+04	year	5.50E+00
58-Ce-137	0	9.00E+00	hour	4.35E+02
54-Xe-138	0	1.42E+01	min	8.11E+13
55-Cs-138	0	3.22E+01	min	1.09E+14
57-La-138	0	1.05E+11	year	1.23E-03
54-Xe-139	0	3.97E+01	sec	1.57E+10
56-Ba-139	0	1.38E+00	hour	1.17E+14
58-Ce-139	0	1.38E+02	day	1.13E+05
54-Xe-140	0	1.36E+01	sec	5.91E+02
56-Ba-140	0	1.27E+01	day	1.21E+14
57-La-140	0	1.68E+00	day	1.21E+14
54-Xe-141	0	1.72E+00	sec	0.00E+00
56-Ba-141	0	1.83E+01	min	8.30E+13
57-La-141	0	3.93E+00	hour	1.12E+14
58-Ce-141	0	3.25E+01	day	1.06E+14
54-Xe-142	0	1.22E+00	sec	0.00E+00
56-Ba-142	0	1.06E+01	min	6.43E+13
57-La-142	0	1.52E+00	hour	1.06E+14
57-La-143	0	1.41E+01	min	7.60E+13
58-Ce-143	0	1.38E+00	day	1.15E+14
54-Xe-144	0	1.15E+00	sec	0.00E+00
58-Ce-144	0	2.85E+02	day	2.68E+13
54-Xe-145	0	9.00E-01	sec	0.00E+00
63-Eu-147	0	2.40E+01	day	6.57E-03
63-Eu-149	0	9.31E+01	day	8.32E+00
63-Eu-152	0	1.33E+01	year	2.35E+07
63-Eu-152	1	9.32E+00	hour	8.96E+04
63-Eu-154	0	8.61E+00	year	1.94E+09
63-Eu-155	0	4.96E+00	year	1.90E+10
63-Eu-156	0	1.52E+01	day	6.59E+11
63-Eu-157	0	1.52E+01	hour	1.72E+11
63-Eu-158	0	4.59E+01	min	7.13E+10



ISSN 1869-9669
ISBN 978-3-7315-0277-7

